Pontificia Universidad Católica del Perú
Escuela de Posgrado

Universidad Carlos III de Madrid
Escuela de Doctorado

Doctoral Thesis

STUDY OF STRUCTURAL JOINTS WITH COMPOSITE MATERIALS TO ENHANCE THE MECHANICAL RESPONSE OF BUS SUPERSTRUCTURES

ESTUDIO DE UNIONES ESTRUCTURALES CON MATERIALES COMPUESTOS PARA MEJORAR EL COMPORTAMIENTO MECÁNICO DE SUPER-ESTRUCTURAS DE AUTOBUSES

A dissertation submitted by as a cotutelle in partial fulfillment of the requirements for the degree of:

Doctor en Ingeniería Mecánica y Organización Industrial (UC3M)
Doctor en Ingeniería (PUCP)

presented by:

Daniel Lavayen Farfán

Thesis Advisors:

UC3M: Dra. María Jesús López Boada

PUCP: Dr. Jorge Antonio Rodríguez Hernández

Madrid, 2022

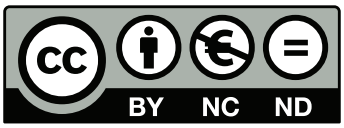

Abstract

Steel structures have an ubiquitous presence in several industries due to their availability and low price. Bus super-structures are typically built using structural steel hollow shapes and serve a major role during crashes and rollovers, as they protect the passengers by absorbing the kinetic energy of impacts and dissipating it as plastic deformations. In recent years, composite materials have gained protagonism in numerous applications due to their high specific strength and stiffness. However, costs and manufacturing complexity have made all-composite automotive structures economically unfeasible. Thus, the current tendency is the use of multimaterial structures: using composites only in the zones where they are needed, while keeping an inexpensive material, like steel, elsewhere. Hollow structural shapes, used in bus structures, are susceptible to bending collapse failure during rollover and crashes, which must be precisely predicted and calculated. Existing theoretical models for this failure mechanism have certain limitations to account for larger thickness, plastic hardening, and composite reinforcements. The present work aims to address these limitations through the development of new theoretical models for the so-called medium-thin-walled hollow shapes, as well as for reinforced CFRP-Steel hollow shapes. Both materials are joined using structural adhesives due to their ease-of-use and relatively low price. Experimental test results have shown the validity and accuracy of the proposed models. These proposed models are then implemented in a concept model of a bus structure to address its crashworthiness and the effectiveness of the reinforced shapes.

Acknowledgments

This thesis project could not have been completed without the support of incredible people that guided me and walked by me throughout this journey.

First, I would like to acknowledge the great support provided by my advisors. The experience, insights and motivation by Maria Jesus were key drivers during the thesis and I hold her the highest regard as I learned much from her. I would also like to thank Coqui for the continuous advice, lessons, and for always pushing me forwards ever since the undergraduate years.

A special mention to José Antonio and Miguel Angel at the Material Science Department at UC3M, who aided the experiments and provided noteworthy insights and suggestions for this work. And also to Edward Herrera for his experience and advice regarding bus design and manufacturing processes.

I would also like to thank my sister Litzy and mother Maria Elena for unconditionally supporting me in every step of the way, through prosperity and adversity.

Last but by any means least, this research project has been supported by the "Proyecto de Mejoramiento y Ampliación de los Servicios del Sistema Nacional de Ciencia Tecnología e Innovación Tecnológica (8682-PE)" through a scholarship provided for the PhD Studies, financed by the World Bank, CONCYTEC and PROCIENCIA (010-20180-FONDECYT-BM-PDAEG). Funding for the experiments has also been received from the Comunidad de Madrid. This work couldn't have been done without their most valued support.

Published and submitted content

In peer reviewed scientific journals:

- Lavayen-Farfan, Daniel, Jose A. Butenegro-Garcia, Maria Jesus L. Boada, Miguel Angel Martinez-Casanova and Jorge A. Rodriguez-Hernandez (2022) "Theoretical and experimental study of the bending collapse of partially reinforced CFRP-Steel square tubes". *Thin-Walled Structures* 177, p. 109457. doi: 10.1016/j.tws.2022.109457

- Lavayen-Farfan, Daniel, Maria Jesus L. Boada, and Jorge A. Rodriguez-Hernandez (2021) "Bending collapse analysis for thin and medium-thin-walled square and rectangular hollow shapes". *Thin-Walled Structures* 165, p. 107934. doi:10.1016/j.tws.2021.107934.

In scientific congresses:

- Lavayen-Farfan, Daniel, Jose A. Butenegro-Garcia, Maria Jesus L. Boada, Miguel Angel Martinez-Casanova and Jorge A. Rodriguez-Hernandez (2021) "Bending collapse of partially reinforced hybrid CFRP-Steel square hollow shapes for implementation in lightweight structures". In: *1st Virtual ESIS TC4 Conference on the fracture of composites and adhesives*. 28-29 September 2021. Online

- Lavayen-Farfan, Daniel, Jose A. Butenegro-Garcia, Maria Jesus L. Boada, Miguel Angel Martinez-Casanova and Jorge A. Rodriguez-Hernandez (2021) "Uniones adhesivas para incorporación de refuerzos en estructuras ligeras susceptibles a colapso por flexión" (in Spanish). In proceedings: *XXI Congreso Internacional de Adhesión y Adhesivos*. 16-17 November 2021. Online.

Accepted presentations in future scientific congresses:

- Lavayen Farfan, Daniel, Jose A. Butenegro-Garcia, Maria Jesus L. Boada, Miguel Angel Martinez-Casanova and Jorge A. Rodriguez-Hernandez (2022) "Sobre el uso de materiales compuestos para el refuerzo y mejora de la resistencia al vuelco de autobuses" (in Spanish). XV Congreso Iberoamericano de Ingeniería Mecánica. Madrid, Spain. 22-24 November, 2022.

- Lavayen Farfan, Daniel, Maria Jesus L. Boada, Jorge A. Rodriguez-Hernandez (2022) "Optimization of the rollover crashworthiness of bus structures with localized composite reinforcements based on concept modelling and theoretical models for bending collapse". The fifth International Conference on Numerical Modelling in Engineering (NME 2022). 24-24 August 2022. Online.

Contents

List of Figures

List of Tables

Chapter 1

Introduction

1.1 Problem statement

Research and development on composites is constantly advancing. Applications can be found all throughout engineering and are expanding everyday gaining further protagonism. In the automotive industry, where lighter and stronger designs are continuously required, composites are widely used due to their excellent strength-to-weight ratio. However, composites behave differently from classical engineering materials, such as steel and aluminum, since they are anisotropic, have different failure mechanisms, and require different manufacturing processes. Nevertheless, research is continuously overcoming the associated difficulties and composites are being incorporated more and more in vehicle manufacturing (K. Friedrich & Almajid, 2013). This increase has mainly to do with multimaterial structures instead of switching materials altogether.

Buses are vehicles that generally have a high center of gravity, which makes them especially vulnerable to rollover accidents (Gillespie, 1992). For this reason, bus structures (also known as super-structures) must be able to withstand a rollover scenario with little damage dealt to the passengers. The importance of rollover crashworthiness evaluation comes from the fatality rate of these kind of accidents (Liang & Le, 2010a; Policia Nacional del Peru, 2017; Rajamani, 2012). For this reason, specific regulations have been adopted all over the world, with the majority of them based on the UN/ECE 66 (2007).

A current tendency in modern manufacturing and lightweight design is the use of multiple and different materials simultaneously, for lighter and better suited designs. The most common problem when working with different materials is the joining or fastening method, especially in structural components. The joints have the critical job to maintain the stiffness of the structure, and absorb part of the deformation energy during an impact. These problems can also be seen as a challenge to overcome in the expanding fields of study of composites, mechanical engineering, and manufacturing (Henning et al., 2019).

1.2 Motivation

Using multimaterial joints, as a replacement of traditional joints in the structure of a bus, can have a significant influence on not only the stiffness and stability, but also the crashworthiness and plastic behavior. It is thus vital to explore the influence these joints have on the response of the structure, especially during a rollover accident, as they must assure the safety of the occupants of the vehicle. UN/ECE 66 (2007) specifies the analysis and requirements that a structure must comply with in order to be "rollover crashworthy". For analysis, quasi-static and dynamic models are used to address the response of the bus, however, they require experimental information from tests, often of bending collapse of the zones with highest internal loads.

The development of multimaterial joints for bus structures is presented as an alternative to modernize the automobile industry, increase crashworthiness, vehicle safety, and to reduce weight and fuel consumption. The current thesis aims to aid these developments and transfer them to the industry, by proposing theoretical models for the bending collapse of steel and CFRP-steel hollow shapes, which can be employed in all stages of structural design.

1.3 Objectives

The main goal of this thesis is the development of theoretical models to predict the behavior of composite - steel shapes and joints for its inclusion in the super-structure of a bus. The structural joint must guarantee at least the same stiffness and strength of a traditional joint and comply with the requirements of the UN/ECE 66 (2007). In order to achieve the main goal, the following specific objectives are used:

- Development of a mechanical / mathematical model of a multimaterial joint made of composite - steel representative of the structure of a bus, as well as the structure itself.
- Experimental characterization of a representative model of the joint with and without reinforcement, in order to calibrate the mechanical and mathematical model.
- Exploration of different geometries for the structure and their effect on the rollover crashworthiness evaluation according to UN/ECE 66 (2007).
- Development of a concept model of a bus section frame for rollover analyses. The developed concept model can be used to explore different geometries and the influence of the reinforcements on the overall crashworthiness. An adequate geometry must provide enough safety while keeping the weight and costs at an acceptable level.

1.4 Methodology

The doctoral research is to be performed as a "cotutelle" thesis, between the Pontifical Catholic University of Peru and the University Carlos III of Madrid in Spain. The thesis posses a two large portions deeply entwined. The first portion corresponds to an experimental study of the collapse of thin-walled shapes, frequently used by bus manufacturers. These steel shapes are then reinforced with composites and their performance is measured and compared. These results are used to build theoretical models of the collapse of thin-walled shapes, and also to calibrate numerical models. The numerical FEM models can then be used to evaluate different geometries and sizes not tested by experiments. The main proposed test to address the crashworthiness capabilities is the three-point bending test. Through this test, the characteristic $M - \theta$ curves can be determined for different geometries. The theoretical model is to be programmed in Matlab and the numerical FEM models are to be developed in Ansys.

The second part of the research corresponds to the study of the structure, using the theoretical models developed beforehand. The goal is to obtain the most adequate dimensions and reinforcements in compliance with the UN/ECE 66 (2007). Multiple simulations are run using different tube sizes with and without the developed reinforcements. The structure itself is modeled as a simplified concept model in order to save calculation time. This evaluation run is performed inside a Matlab environment with communication with Ansys (which also needs to be developed).

1.5 Expected results

The main outputs of this work are the following:

- A model for the evaluation of the critical zones of a structure. This model can then be implemented as a custom finite element to address the behavior and response of new structures in many fields, not just automotive.
- A methodology to improve the design of bus structures, making sure they comply with the corresponding regulations.
- Provide tools and techniques to the automotive industry for better and lighter designs.

1.6 Overview

The present document is organized in seven chapters, which are described below. This organizations loosely follows the objectives set beforehand.

Chapter 2: This chapter serves as a general state of the art for most of the topics required for the thesis development. The goal of this chapter is to provide a general overview of the current and most important research in different fields, ranging from bending collapse of thin-walled shapes, adhesives, composites, calculation methods and meta models.

Chapter 3: In this chapter, the study cases are described and benchmarked with a linear analysis. It serves to identify the most critical zones. Also, some candidates of reinforcements and hybrid nodes are proposed.

Chapter 4: In this chapter, the bending collapse of unreinforced, square and rectangular hollow shapes is described. A collapse theory, based on the existing Kecman theory, is proposed and it is found that it can make better predictions than the original when working with "medium-thin-walled" commercial shapes. This chapter is a reproduction of Lavayen-Farfan et al. (2021).

Chapter 5: Further work is performed on the bending collapse of hollow shapes. A new theoretical approach is developed to predict the bending collapse response curves for CFRP-steel shapes. In this case, the steel shapes are partially reinforced with CFRP plates on the flanges and the webs and the increase in strength and specific energy absorbed is measured. This chapter is a reproduction of Lavayen-Farfan et al. (2022)

Chapter 6: Once the collapse mechanism for unreinforced and reinforced shapes is described and analyzed, the next stage is their incorporation into a bus model for rollover analysis. A concept model of a bay of the bus is constructed and analyzed using both the unreinforced and reinforced shapes.

Chapter 7: Conclusions and outlook of the whole work is presented as a wrap-up of the project.

The workflow of the thesis can be seen in Fig. 1.1.

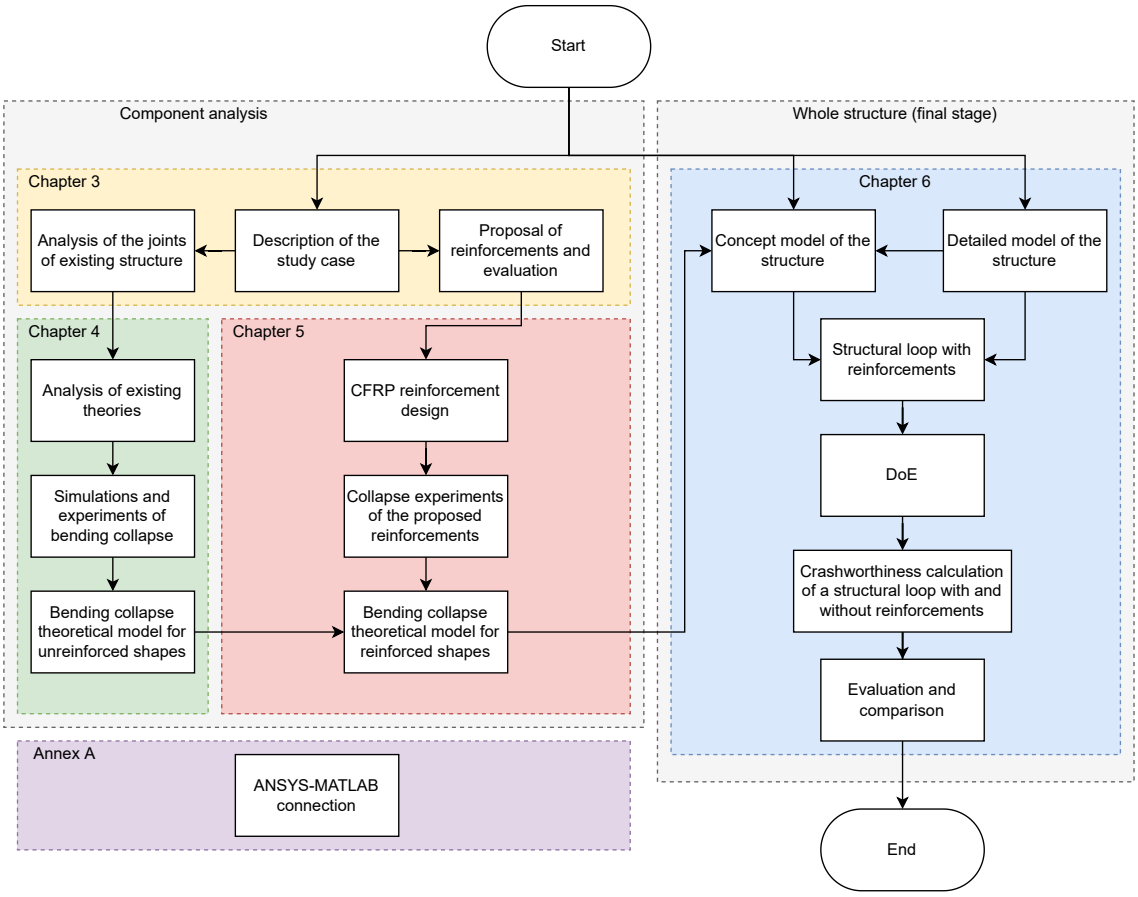

Figure 1.1: Thesis flowchart.

Chapter 2

State of the art - Literature review

In general terms, automotive safety can be studied from two perspectives. The first one consists of accident prevention, otherwise known as active safety measures, which seeks to improve accident avoidance and reduce the probabilities of an accident by attacking its possible causes, either human, technical, environmental, etc. The second perspective consists of accident mitigation or passive safety, which encompasses measures taken to lessen the damage caused to the passengers (Seiffert & Gonter, 2013). In this chapter, the main aspects related to rollover crashworthiness in buses are explored. A comprehensive literature review is performed on several topics including: use of composite materials, techniques for analysis of structures, calculation tools, joint methods, etc. By reviewing the recent literature, a better insight is gained to the areas required for the development of this thesis, as well as those areas where new advances are needed.

2.1 Vehicle rollover

As mentioned beforehand, vehicle rollover accidents are responsible of a great number of fatalities when compared to other accidents. According to Rajamani (2012), up to a third of rollover accidents report loss of human lives, thus continuous research and developments are performed in accident mitigation and avoidance. For instance, one of the most common methods to avoid these kind of accidents is highway design, where the curves are banked with an angle α_g.

Rollover analysis can be performed by considering the vehicle as a solid rigid traveling a banked curve at a certain constant velocity v. By traveling said curve, the vehicle is under an acceleration that points towards the center of curvature, as seen in Fig. 2.1. This acceleration translates into a centrifugal force that, in fact, produces the rollover. Under this effect, the normal force between the road and inner tires decreases, while the force between the road and outer tires increases. The limit condition occurs when the former reaches zero. According to the equations of dynamic equilibrium (d'Alembert's principle), the minimum acceleration required for this condition can be defined:

$$a_y := \frac{t/2 + \alpha_g h}{h} g \tag{2.1}$$

where t is the track width of the vehicle, h the height of the center of gravity, and g the acceleration due to gravity. Moreover, the value $t/2h$ can be defined as the rollover threshold according to Gillespie (1992) or SSF[1], according to Rajamani (2012), and is defined when the vehicle travels along a plain curve ($\alpha_g = 0$). If the SSF is low, so is the acceleration required to produce rollover, making it more probable. Due to its pure dependence on geometric factors, SSF is a widely used parameter to measure the

[1] Static stability factor.

propensity to rollover. It can also be seen that vehicles with large h, such as buses and heavy trucks, are naturally more prone to rollover.

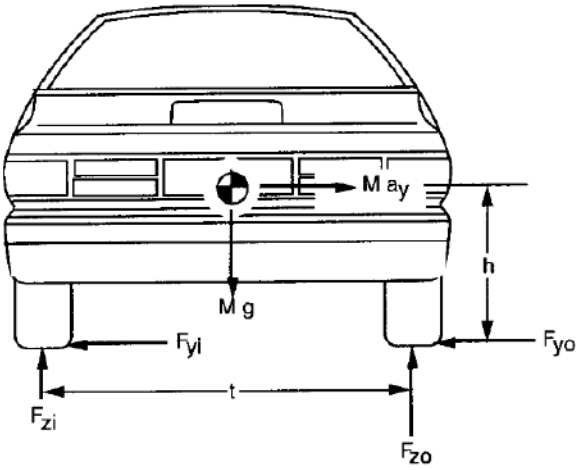

Figure 2.1: One DoF model for modeling the rollover of a vehicle. Source: Gillespie (1992).

Since rollover is a dynamic phenomenon, a time transient analysis is also required, in which not only the geometric characteristics of the vehicle are considered, but also the influence of other factors such as suspension, the road itself, etc. For instance, when a vehicle suddenly enters a curve, its roll angle also suddenly changes and slightly oscillates as shown in Fig. 2.2. Depending on the suspension, this oscillation may be quickly dissipated.

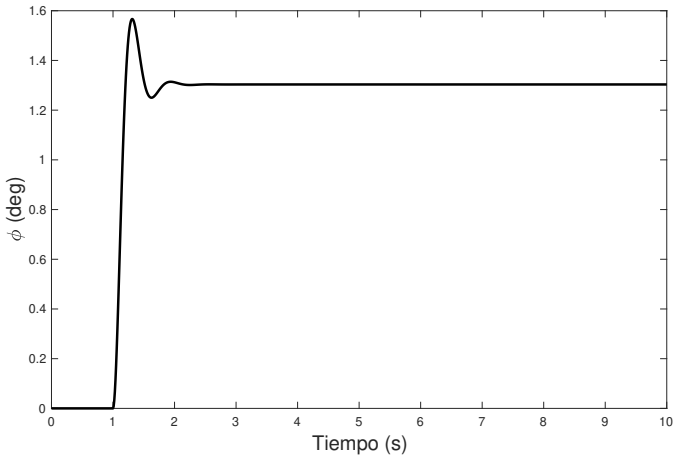

Figure 2.2: Roll angle change due to a sudden lateral acceleration. Adapted from Gillespie (1992).

If a rollover accident were to occur, passengers are susceptible to being crushed to death by the structure, being thrown outside the vehicle, or suffer injuries and trauma. To prevent these accidents from happening, the following measures can be taken:

- Highway curves must be banked, so that the bank angle α_g increases the SSF. The ultimate goal of the banked surface is to provide an inclined plane that supports part of the normal acceleration produced when traveling along the curve.
- Differentiated speed limits for different vehicle types and weights. However, this measure is highly dependent of the driving habits and does not take into conside-

ration factors such as suspension, stiffness of the vehicle, environmental conditions, etc.

- Autonomous driving systems and warning systems focused on prevention of slipping and rollover (Chu et al., 2018).

Although there are measures in rollover avoidance, vehicle structures, especially bus structures, must be able to minimize the damage dealt to the passengers.

2.1.1 Regulations related to rollover

The super-structures of buses must guarantee certain safety parameters during a rollover event. Thus, there are special regulations related to safety and rollover crashworthiness that a bus must comply in order to circulate. Some of these regulations are the UN/ECE 66 (2007) in EU, the FMVSS 220 (US DoT, 1976) in the USA (used for a wide range of heavy vehicles), the AIS 031 in India, the SANS 1563 in South Africa, the ADR 59/00 in Australia (the three last ones based on the UN/ECE R66). The specific requirements can be summarized as follows:

- UN/ECE 66 (2007) and AIS 031 require that the structure is tested in a rollover test (or alternatives). These standards define the so-called "residual space" which is a space that shall not be invaded during the rollover test of the structure; thus it provides a survival space for the occupants (as seen in Fig. 2.3). UN/ECE 66 (2007) has been initially thought for single-decker buses, whereas AIS 031 incorporates the definition of residual spaces for double-decker buses.

- On the other hand, FMVSS 220 establishes a test where a quasi-static load, equivalent to 1.5 times the weight of the vehicle, is applied to the roof of the vehicle and the deformation is measured. However, this test differs from the actual rollover accident, and is more related to the bus falling upside down. In fact, UN/ECE 66 (2007) reflects the real rollover phenomenon better, as evidenced by Liang and Le (2010b). Moreover, Gepner et al. (2014) showed that the requirements of FMVSS 220 end up in unbalanced designs, unreal conditions, and recommends the use of UN/ECE 66 (2007). It is no wonder that a new regulation is being developed for the US, with stricter requirements than the R66 (Zhou et al., 2019).

The dimensions of the residual space according to UN/ECE 66 (2007) are shown in Fig 2.3 and are extended along the whole cabin. It ends 200 mm behind the last seat and 600 mm ahead of the front seat. The manufacturer can also define a larger residual space.

The rollover test consists of installing the bus structure (or the whole bus), with the suspension mechanism blocked and the equivalent weight of the passengers, on top of a pivoted surface. This surface is then inclined slowly until the structure reaches the point of unstable equilibrium. Then, the structure must fall down a ditch 800 mm deep. A schematic of the test is shown in Fig. 2.4.

This test requires a finished prototype of the structure and its destruction, as well as access to a pivoted surface capable of lifting the whole bus. This requirements have a high cost for manufacturers just to try new prototypes (Nigade et al., 2013). For this reason, the following alternatives are proposed by the R66:

- Rollover test with a representative section of the bus instead of the whole structure. The cost is significantly reduced, since only a section of the bus must be tested and destroyed.

- Quasi-static test on a representative section of the bus, in which the load is applied to the roof of the structure. The absorbed energy of the structure must be at least the same as the kinetic energy during the rollover test.

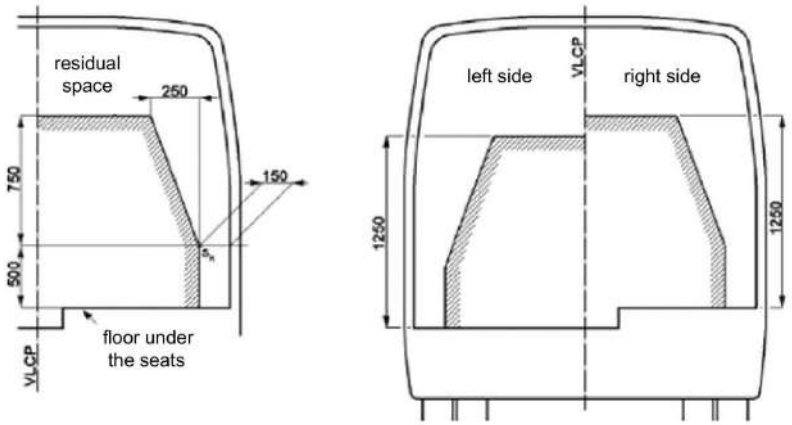

Figure 2.3: Residual space definition. Source: UN/ECE 66 (2007).

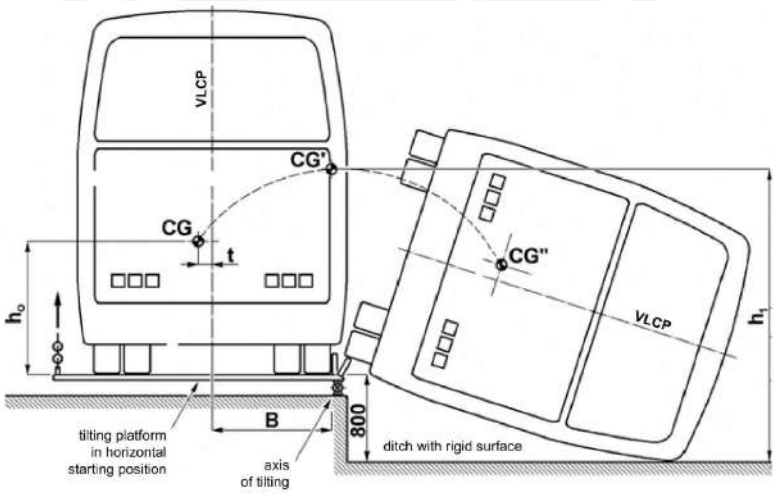

Figure 2.4: Rollover test scheme. Source: UN/ECE 66 (2007).

- Quasi-static calculation based on testing of the structural components. The model for calculation must identify zones where plastic deformations are prone to occur, as well as those where plastic hinges are prone to appear due to bending collapse (see Fig. 2.5 left). Each of the plastic zones can be idealized through its constitutive law (see Fig. 2.5 right). The amount of energy absorbed by the structure must be larger than the kinetic energy from the rollover test. It is worth noting that the plastic hinges show two characteristic curves: quasi-static and dynamic. Dynamic curves may be defined through an impact test or by multiplying the quasi-static curve by a factor K_d, which is 1.2 for steel. The resulting curve can be seen in Fig. 2.6.
- Finite element simulation of the rollover test. UN/ECE R66 allows this method as long as it is validated through experimental tests.

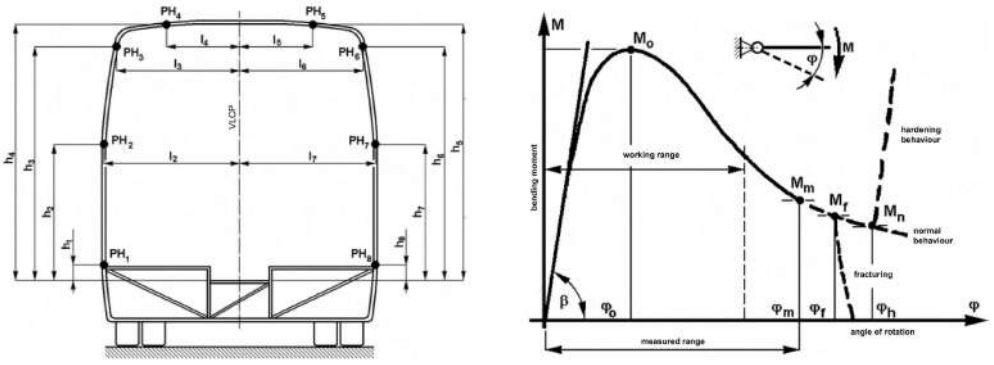

Figure 2.5: Left: Location of the plastic hinges. Right: their corresponding constitutive law $M - \theta$ typically obtained through testing. Source: UN/ECE 66 (2007).

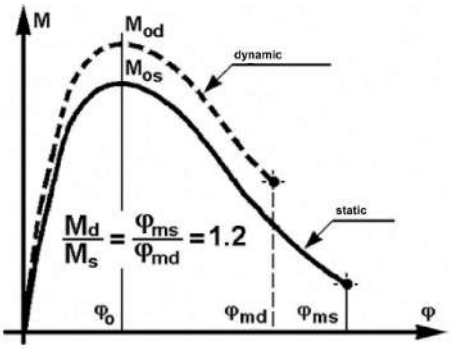

Figure 2.6: Relationship between the dynamic and static $M-\theta$ for a plastic hinge. Source: UN/ECE 66 (2007).

2.1.2 Rollover crashworthiness research

There has been plentiful research about rollover tests on bus structures, and most of them take into consideration the requirements established by the existing regulations. Research has been able to identify substantial differences between regulations and the effectiveness of design practices. For instance, Liang and Le (2010b) compared two different bus models (one of them following the recommendations of (Roca et al., 1997)), and found that the lateral panels are the zones that absorb the most kinetic energy (See Fig. 2.7). The aforementioned authors also found that the European R66 describes better the rollover scenario than the American counterpart. Since numerical simulations were used, the authors had to run tests on the joints in order to validate the simulations.

Similar research has been performed by Gepner et al. (2014), who tested paratransit buses, [2] and elaborated numerical simulations. By using ANOVA and Sobol analyses, the joints of the walls with the roof and floor are the most influential zones for crashworthiness.

Roca et al. (1997) established certain recommendations to improve the crashworthiness of the structure. It was observed, from long before the establishment of R66, that bending collapse is the most important energy absorption mechanism. Thus, the following criteria were defined:

- Joints between the columns and floor and roof must remain as elastic as possible. Collapse should occur as far from them as possible.
- The plastic hinges should occur on the structural shapes of the columns and roof, not on the joints.

[2] Buses typically used in North America for transport of people with disabilities.

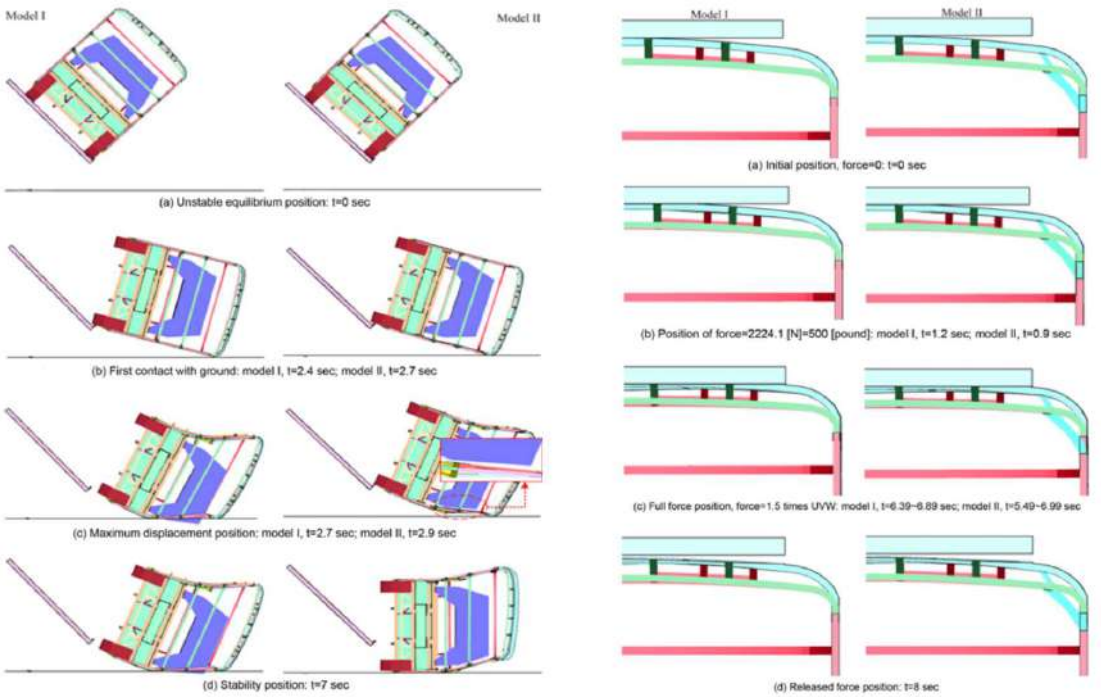

Figure 2.7: Comparison between the rollover tests in LS-DYNA following UN/ECE R66 and FMVSS 220. Source: Liang and Le (2010b).

- Columns, roof and floor must form a closed loop or ring. If elements are not connected, the structure will not likely pass the rollover test. It is especially important that no longitudinal members interfere with the roof and columns.

Due to the deficiencies of FMVSS 220, the NHTSA[3] recently proposed new regulations for bus rollover crashworthiness, largely based on UN/ECE R66 with stricter requirements. Research by Zhou et al. (2019) summarizes the new requirements as follows:

1. The proposed regulation requires the addition of a 68 kg mass on each seat to represent the weight of the seated people. In the European regulation, this addition must only be done when seat belts are installed.

2. Approval using alternative methods, such a quasi-static calculation and equivalent sections, is no longer valid.

3. Rollover simulation is no longer valid, since it requires experimental data after all.

The largest influence lies on the addition of the weight of the passengers. It was once again confirmed that the joints of the columns, roof and floor along the structural rings are the zones that absorb the most energy (Fig. 2.8). In order to validate the simulation, experimental tests of the joints are performed as seen in Fig. 2.9.

On the other hand, the CIC[4] performs static and dynamic analyses to verify the fulfillment of the requirements of R66, and its method is the only one accepted in the UK as valid (Hashemi et al., 2009). This method consists of:

[3]National Highway Transit Safety Administration.
[4]Cranfield Impact Centre - UK

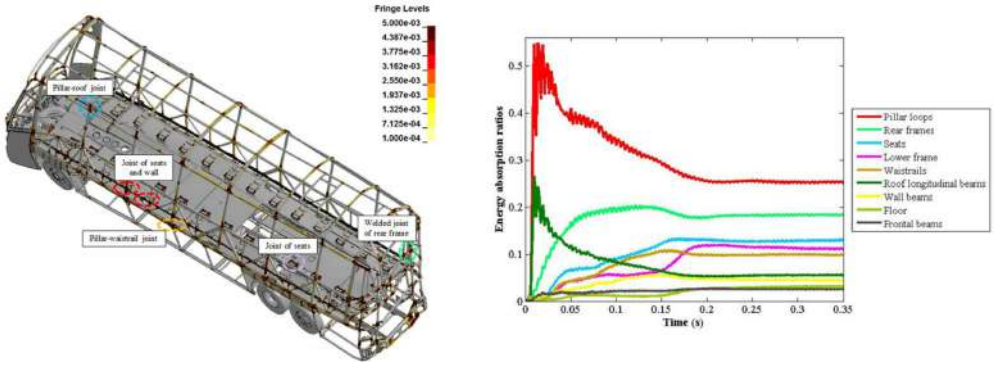

Figure 2.8: Left: location of the plastic hinges in the structural rings. Right: energy absorbed by each component of the structure. Source: Zhou et al. (2019).

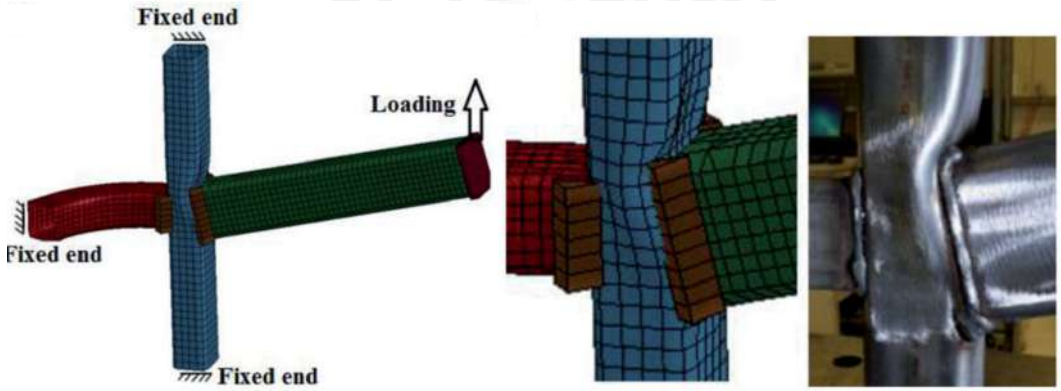

Figure 2.9: Model used for the validation of the structural joints. Source: Zhou et al. (2019).

- Creation of a quasi-static model using BEAM elements for the super-structure.
- Prediction of the rollover test based on the theoretical material properties.
- Quasi-static and dynamic tests of the regions next to the roof, railings, roof.
- Introduction of the experimental tests into the FEM model for approval.

2.1.3 Bending collapse

Kecman's model

As explained before, calculation and verification according to R66 requires the data about the $M-\theta$ curves of the plastic hinges that form in the structure. These hinges appear due to bending collapse of the structural shapes. Thus, a calculation method for the $M-\theta$ is required for the most commonly used structural shapes in buses, namely square and rectangular hollow shapes. Kecman (1979) was one of the first authors that described the bending collapse phenomenon on rectangular, thin-walled, hollow shapes, based on previous works by Rhodes and Harvey (1971), who determined the collapse load for these shapes.

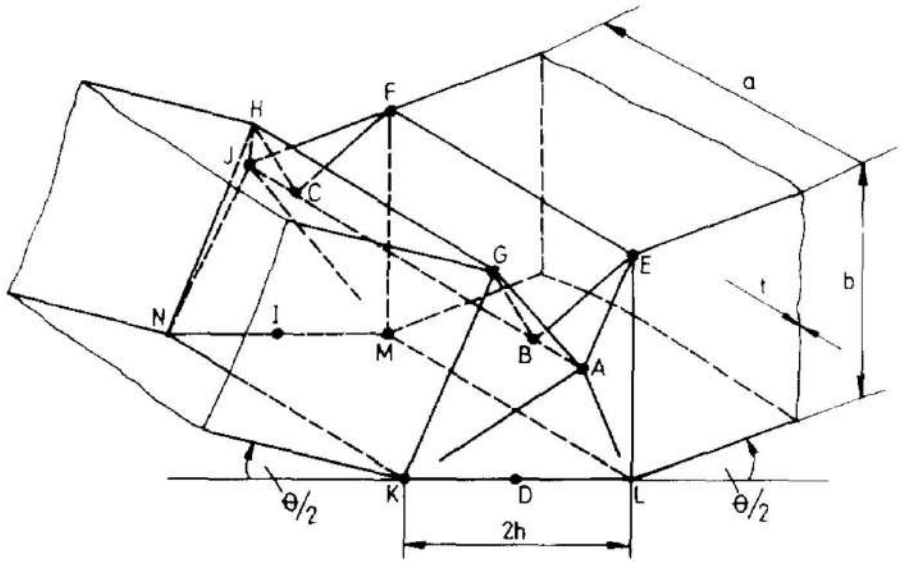

Figure 2.10: Collapse model with plastic hinge lines by Kecman (1979).

The model by Kecman (1983) is based on the calculation of the energy absorbed by each hinge line that forms in the collapsed zone, as seen in Fig 2.10. The energy on each line can be calculated as:

$$W_i = \int_0^{\psi} m_P L d\psi = m_P L \psi \tag{2.2}$$

where the term m_p is the plastic moment per unit length on the plastic hinge, L is the length of the plastic hinge line, and ψ is the bending angle of the plastic hinge line. For a elastic-perfectly plastic material, m_p can be defined in terms of the nominal flow stress σ_0 and thickness t of the shape, as follows:

$$m_p = \frac{1}{4}\sigma_0 t^2 \tag{2.3}$$

Hinge lines can be grouped into 9 groups[5]. Each term refers to a hinge line shown in Fig. 2.10. The energy absorbed by each group can then be quantified as follows:

$$W_1 = W_{EF} + W_{GH} = 2m_p a \left[\pi/2 - \rho - \arcsin\left(1 - \frac{b}{h}\sin\rho\right)\right] \tag{2.4}$$

$$W_2 = W_{BC} = m_p a \left[\pi - 2\arcsin\left(1 - \frac{b}{h}\sin\rho\right)\right] \tag{2.5}$$

$$W_3 = W_{AB} + W_{CJ} = 2m_p \left(b\sin^2\rho - h\sin\rho + \sqrt{b\sin\rho\,(2h - b\sin\rho)}\cos\rho\right) \times \left(\pi - \rho - \arcsin\left(1 - \frac{b}{h}\sin\rho\right)\right) \tag{2.6}$$

$$W_4 = W_{BG} + W_{BE} + W_{CH} + W_{CF} = 4m_p h\pi/2 \tag{2.7}$$

[5]Some authors, including Kecman, recognize 8 groups. However, the last term is usually separated to include the influence of reinforcements.

$$W_5 = W_{GK} + W_{EL} + W_{HN} + W_{FM} = 4m_p b \arctan\left[\frac{z_A}{\sqrt{(h - x_A")^2 + (y_A" - y_B)^2}}\right] \tag{2.8}$$

$$W_6 = W_{GA} + W_{AE} + W_{CH} + W_{CF} = 4m_p \frac{h}{r_{roll}} z_A \tag{2.9}$$

$$W_7 = W_{KA} + W_{LA} + W_{NJ} + W_{MJ} = \frac{8}{3} m_p \frac{z_A}{r} \sqrt{h^2 + y_b^2 + z_A^2} \tag{2.10}$$

$$W_8 = W_{KN} + W_{LM} = 2m_p\,(a\rho) \tag{2.11}$$

$$W_9 = W_{KL} + W_{MN} = 2m_p \left(2h \arctan\left(\frac{z_A}{y_A}\right)\right) \tag{2.12}$$

The term W_6 depends on the rolling radius r_{roll} which requires an empirical expression. Authors such as Huang and Zhang (2018), Kecman (1983), and Lavayen-Farfan et al. (2022) arrived at different variations for this term. Once the total deformation energy is calculated, the total moment on the plastic hinge can be determined using numerical derivation:

$$M(\theta) = \frac{d}{d\theta} \sum_{i=1}^{9} W_i \approx \frac{W(\theta + \Delta\theta) - W(\theta)}{\Delta\theta} \tag{2.13}$$

However, the calculation of the collapse stage based on the absorbed energy does not include the calculation of the maximum moment. The determination of the peak moment was first described by Rhodes and Harvey (1971). Nonetheless, this calculation is based on the bending collapse of lipped channels, instead of rectangular hollow shapes. Later, Kecman (1979) found that the method described by Rhodes and Harvey (1971) can be used for thin-walled rectangular shapes as long as the flange is considered as the compression part, as shown in Fig. 2.11.

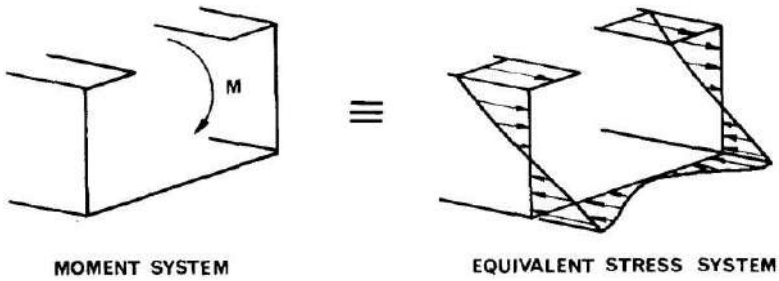

Figure 2.11: Collapse model by Rhodes and Harvey (1971) used to determine the maximum moment.

It was found that depending on the dimensions of the shape, the collapse might be totally elastic, elasto-plastic, or completely plastic. The behavior depends on the critical stress σ_{crit}, the yield stress σ_Y, and the tensile stress σ_U. The critical stress can be defined as:

$$\sigma_{cr} := \frac{\pi^2 E}{12(1 - \nu^2)} \left(5.23 + 0.16\frac{a}{b}\right) \left(\frac{t}{a}\right)^2 \tag{2.14}$$

An effective width a_e can also be defined as follows:

$$a_e := \begin{cases} a\left(0.7\frac{\sigma_{cr}}{\sigma_Y} + 0.3\right) & \text{, si } \sigma_{cr} > \sigma_Y \\ a & \text{, si } \sigma_{cr} \leq \sigma_Y \end{cases} \tag{2.15}$$

The maximum moment is then defined as follows:

- $\sigma_{cr} < \sigma_Y$:

$$M_m = M_{m'} = \sigma_Y t b^2 \left[\frac{2a + b + a_e\left(3\frac{a}{b} + 2\right)}{3(a+b)}\right] \tag{2.16}$$

- $\sigma_{cr} \geq 3\sigma_Y$:

$$M_m = M_p = \sigma_Y t\left[a(b-t) + 0.5(b-2t)^2\right] \tag{2.17}$$

- $\sigma_Y < \sigma_{cr} \leq 3\sigma_Y$:

$$M_{p'} = M_y = \sigma_Y t b\left(a + \frac{b}{3}\right), \tag{2.18}$$

$$M_m = M_{p'} + (M_p - M_{p'})\frac{\sigma_{cr} - \sigma_Y}{2\sigma_Y} \tag{2.19}$$

In this approach, the angle at which M_m occurs is neglected and only plastic angles are plotted, mainly because the elastic stage is considered to absorb a negligible amount of energy when compared to the collapse stage. On the other hand, since the calculation with Eq. 2.13 results in very high moments for low angles in the $M-\theta$ curve, it is often capped with the value of M_m. The point $(0, M_m)$ may also be connected to the $M-\theta$ curve with a tangent line. Either way, the collapse behavior is completely defined, however, the behavior before collapse is still not defined.

Some of the suppositions by Kecman have been observed by various authors:

- Plastic deformations are only considered to occur along the hinge lines. This supposition generates a kinematic incompatibility, which does not occur on the models by Abramowicz and Jones (1997), T. H. Kim and Reid (2001), Wierzbicki and Abramowicz (1983), and Wierzbicki et al. (1994a, 1994b).
- The rolling radius is obtained through an empiric expression. Even when it guarantees good results for thin-walled shapes made out of steel. It should be checked if it works for medium-thin-walled shapes and hybrid shapes.
- The flow stress σ_0 used is the tensile strength. Other authors suggested that the average between the yield and tensile strength is used.
- The length of the plastic hinge h is considered as the shortest side of the shape. However, this does not always occur as revealed from FEM simulations.

Even when there are observations to the suppositions of the original model, it is still one of the most commonly used theories nowadays, since it is a fast tool to obtain the $M-\theta$ curve.

Wierzbicki and Abramowicz basic folding mechanism

In the work by Wierzbicki and Abramowicz (1983), the compression collapse of hollow shapes is analyzed. The authors proposed a basic folding mechanism for thin-walled shapes. An important addition is the consideration of the energy absorbed by a toroidal and conical surfaces, not considered in Kecman's original analysis. By working in these manner, the kinetic incompatibilities are solved. This model is later used for bending and compression collapse (Wierzbicki et al., 1994a, 1994b).

An important remark is that the authors considered that the nominal flow stress is less than the tensile strength σ_u:

$$0.9\sigma_u < \sigma_0 < 0.95\sigma_u \tag{2.20}$$

Kim and Reid model

The model proposed by T. H. Kim and Reid (2001) does not suffer from the kinematic incompatibilities found in the former models, as it redefines certain geometric parameters and energy terms differently than Kecman (1983). It also adds the influence of the plastic deformation of the toroidal surface marked in Fig. 2.12. The difference between this model and the model by Wierzbicki relies on the way the deformation in the toroidal zone is calculated.

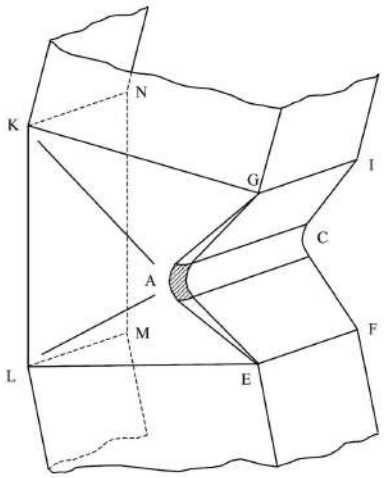

Figure 2.12: Model developed by T. H. Kim and Reid (2001).

Another important characteristic of this model is that it classifies the different hinge lines where plastic deformation occurs. Concretely, three types of hinge lines are defined, as seen in Fig. 2.12.

1. Stationary hinge lines: GI, EF, AC, KG, LE, KL.
2. Rolling hinge lines: GA, EA, KA, LA.
3. Toroidal surface: A

The resulting model fits the experimental data very closely, predicting in most cases a maximum moment slightly less than the one determined by Kecman. Thus, it could be said, that this model is slightly more conservative.

Huang and Zhang model

Recently, Huang and Zhang (2018) developed a theoretical model based on the work by Kecman, to analyze the collapse of thin-walled aluminum hollow shapes. The main characteristics of this model are:

- Three stages are considered:
    1. Elastic stage: is considered as line starting on the origin, up to (θ_e, M_e).
    2. Plastic stage: is considered from the end of the previous stage up to (θ_{max}, M_{max}), and has a parabolic shape, with the maximum moment as the vertex.
    3. Collapse stage: starts from (θ_{max}, M_{max}) and follows Kecman's theory with certain modifications.

- Some of the terms of the collapse stage are obtained using correlations from experimental data, such as M_{max}, h y r.

An important contribution is the classification of three types of collapse, which have an important influence on the post-collapse behavior of the shape. It should also be noted, that depending on the geometric dimensions, the type of collapse may switch midway. The three types are as follows:

1. Indentation: This failure mode is common in shapes with short length or low slenderness, or shapes with large thickness. This failure mode requires high forces to occur. It is not representative at all of the bending collapse mechanism.

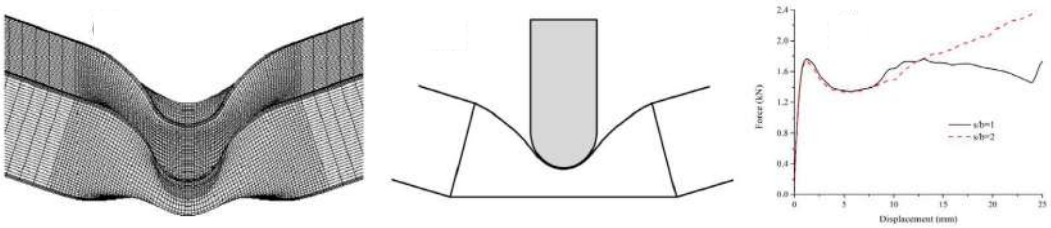

Figure 2.13: Indentation collapse. Source: Huang and Zhang (2018).

2. Bending and indentation collapse: This is a mixed collapse behavior, typically with shapes of medium slenderness, or ratio of length to height $3 \leq h/l_s < 7$. Typically, shapes of medium slenderness will start with indentation collapse and later switch to bending collapse.

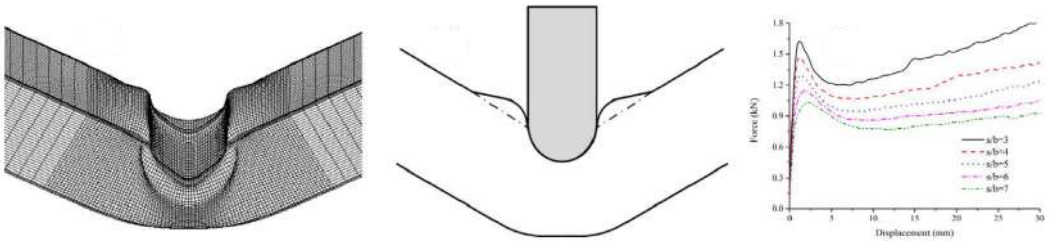

Figure 2.14: Bending and indentation collapse. Source: Huang and Zhang (2018).

3. Bending collapse: This failure mode occurs in shapes with large slenderness or length ot height ratio of $8 \leq h/l_s$. This failure mode is the desired outcome, since is the one suffered by the structural shapes of a bus structure during rollover. It should be also noted, that this failure mode offers less strength and energy absorption than the previously described ones.

This model has a drawback. Since the correlations are found using tests on aluminum specimens, the model may not work properly with other materials. This means that it

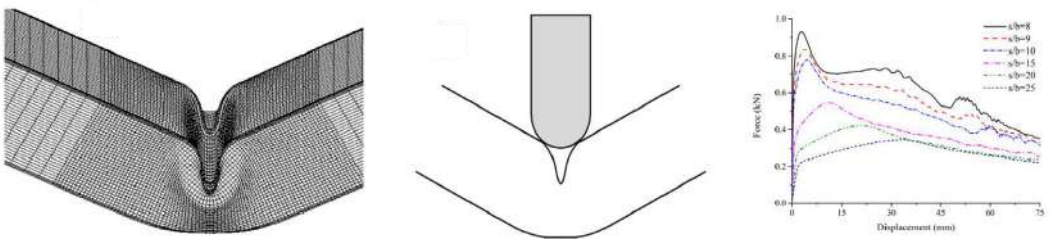

Figure 2.15: Bending collapse. Source: Huang and Zhang (2018).

may not readily applicable for steel hollow shapes, or composite shapes. Alternatively, the developed method could be used to fit data obtained with shapes made of other materials.

It should be noted, that most of the surveyed literature focuses on thin-walled shapes with thicknesses typically thinner than those of commercial shapes.

2.2 Composite materials and adhesive joints

Composites materials, commonly referred to only as *composites* are materials formed by two or more different base materials at different volumetric fractions. Typically, they are composed of base or matrix material, and a reinforcement. Some of the most commonly used composites are fiber reinforced polymers or FRPs, where the matrix consists of an polymer such as epoxy resin or polyamide, and the reinforcement is a fiber of extremely high mechanical properties such as carbon, glass, or para-aramid fiber. The role of the matrix is to keep the fibers together and pass the loads to the fibers, which are the ones that actually carry the load (Kelly & Clyne, 1999). Composites provide excellent mechanical properties in one or two directions and low weight. However, due to their anisotropic nature, they cannot endure all types of loads.

To compare composites with other materials, the specific mechanical properties are often used. These are obtained by dividing the actual mechanical properties by their density, to make the comparison more objective. A short comparison can be seen in Table 2.1. It can be readily seen that composites offer much higher specific strength and stiffness than steel or aluminum

2.2.1 Use of composites in the automotive industry

Even though the use of composite materials in vehicles is not new, it is somewhat limited. Recent years have witnessed a significant growth in their applications, but not yet widespread as structural elements. Some examples are shown in Fig. 2.16, where glass fiber based composites (GFRP) are used as secondary structural elements.

According to Henning et al. (2019), most of the composites currently used in vehicles are made from discontinuous fibers. They are usually used for semi-structural components of complex shapes. González et al. (2017) showed that FRPs have a large energy absorption capability before fracture, in the range of 10 to 50 kJ/m^2, making them an interesting choice for structural applications where energy absorption is an important feature, such as bending collapse (discussed in section 2.1.2). However, this potential application may be limited by the price, and bounded to applications such as competition vehicles such as F1 (Wilson, 2017). This limitation comes from the high production cycles and costs

Table 2.1: Comparison of specific mechanical properties. Adapted from: Matthews and Rawlings (2008)

Material	Young modulus [GPa]	Tensile strength [MPa]	Density [Mg/m^3]	Specific stiffness [GPa/Mg/m^3]	Specific strength [MPa/Mg/m^3]
Nylon 66 + 40% carbon fiber	22	246	1.34	16	184
Epoxy + 70% glass fiber	42	750	1.9	22	395
Epoxy + 60% aramid	77	1800	1.4	55	1284
Steel	210	460	7.86	27	59
Aluminum	69	77	2.7	26	29

(Lauter et al., 2013). Three main factors have been identified by Henning et al. (2019) as the limiting factors for the widespread use of CFRP in the automotion industry:

1. Manufacturing processes are not always completely adaptable for production lines, where the processing times are sometimes less than 3 minutes.
2. Required materials have high associated costs in comparison to typically used structural materials.
3. There are verification processes to detect manufacturing defects, wrinkling of the fibers, internal discontinuities, distortions, and to guarantee the dimensional tolerances, that do not always integrate well into the production line.

In the past years, there have been projects and prototypes to use composite as structural elements, especially in massive transport vehicles such as buses. For instance, the project COMPOBUS had as an objective the design and development of the structure of a bus using polyester resin with carbon and glass fibers, manufactured from filament winding (Castejon et al., 2006). The prototype was able to pass the rollover tests required by the R66, with weight reduction of 1 Ton, in comparison to a similar structure made from steel.

A similar project was Litebus (2009), which had the following design goals: 1) weight and cost reduction of mass transport vehicles by the introduction of multimaterial panels; 2) development of design technologies aimed at reducing production costs, functional integration, easy of repair, and recycling. During this project, there was an extensive use of adhesive joints, mainly due to the need of using multimaterial joints. Even when it was technically possible to build a bus using composites, it was not economically feasible, as the production costs skyrocketed, establishing a total budget of 2 million EUR (Adams, 2017; Litebus, 2009).

2.2.2 Composite structural joints

Welding is often used in bus structures to join together different structural elements (beams, cantrails and columns), since they are almost always made of steel. One of the main problems of introducing composite components is joining them to other materials, since traditional welding is no longer feasible. A variety of alternatives exist and the choice ultimately comes to factors such as: available materials and equipment, costs, type

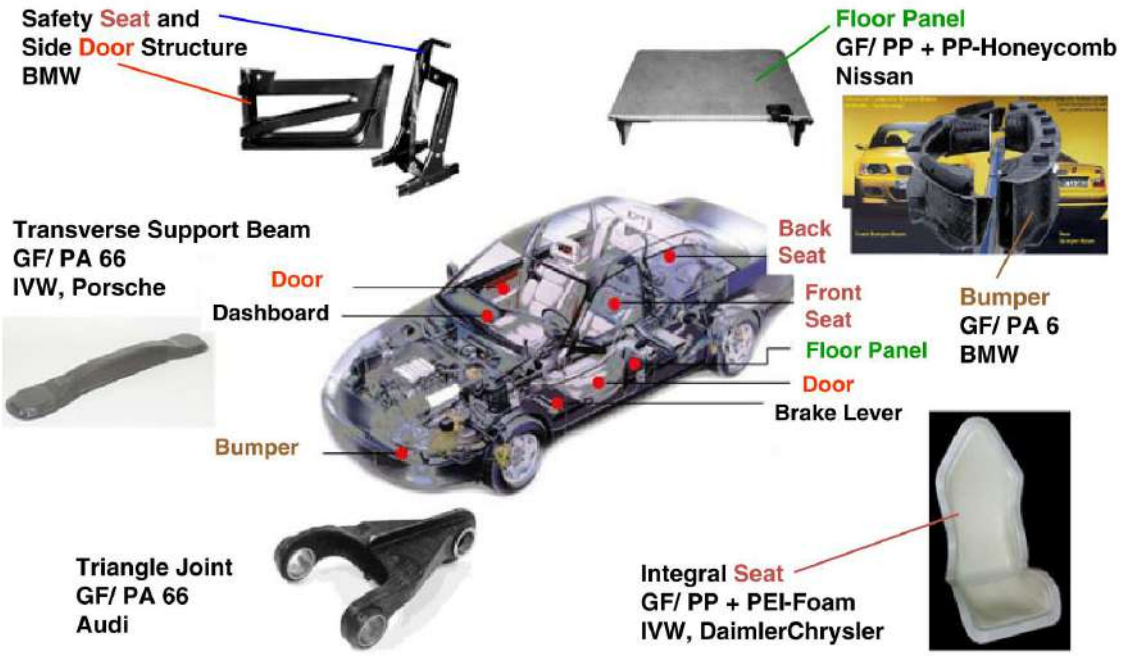

Figure 2.16: Automobile elements made of FRPs. Source: K. Friedrich and Almajid (2013).

of loading, etc. The geometry of the joint, as well as the mechanical properties also have a strong influence on the stress distribution in the joint.

Kah et al. (2014) summarized a series of techniques to join together metals and polymers for structural joints. The main techniques are listed below:

Adhesive joints: these joints are inexpensive and a relatively quick way to join dissimilar materials. Development of high strength and high modulus adhesives has allowed them to be used in structural applications such as aerospace and automotive industries.

Mechanical fastening: refers to the use of elements such as bolts, nuts, rivets or any other additional mechanical element to join two materials. The main advantage of these joints is that they are direct, dismountable, and quick. However, they add extra weight to the assembly, and the preparations (through holes, and threads) produce stress concentration points. These points are extremely dangerous in composites (Adams, 2017).

Welding: There are many techniques to weld dissimilar materials. In all of them, energy is provided in some way to melt down the materials locally. The energy can be provided as heat, friction, laser, ultrasonic vibrations, etc. The most important limitation for welding composites is that the matrix must be a thermoplastic polymer. Research still has to be done in this field.

Special interest is put on adhesive joints. When compared to other joining techniques, they do not require specialized equipment, need little preparation, and are comparatively inexpensive. Another common way to join together composites with other materials is the use of bolted joints. However, the stress concentration from the through holes produce

delamination and permanent damage in the composite, potentially reducing its strength by half (Ataş & Soutis, 2017).

2.2.3 Adhesive joints

As mentioned, adhesive joints are a direct method to joint elements of dissimilar materials. They consist on applying a thin layer of adhesive in between the contacting surfaces. The advantage are 1) the uniform stress distribution (avoiding the stress concentration problem), 2) possibility of joining together dissimilar materials, 3) no corrosion and 4) no large investment in equipment.

An adhesive joint consists on three fundamental parts: the adhesive and two substrates or adherents. The substrates are the parts to be joint and may not always be made of the same material. Depending on the type of load, the available space, manufacturing process, one of the geometric arrangements in Fig. 2.17 can be used. Some of the most commonly used joints are the single lap joints (Araújo et al., 2017), and thus are also standardized in ISO 4587:2003 and EN 11465:2009.

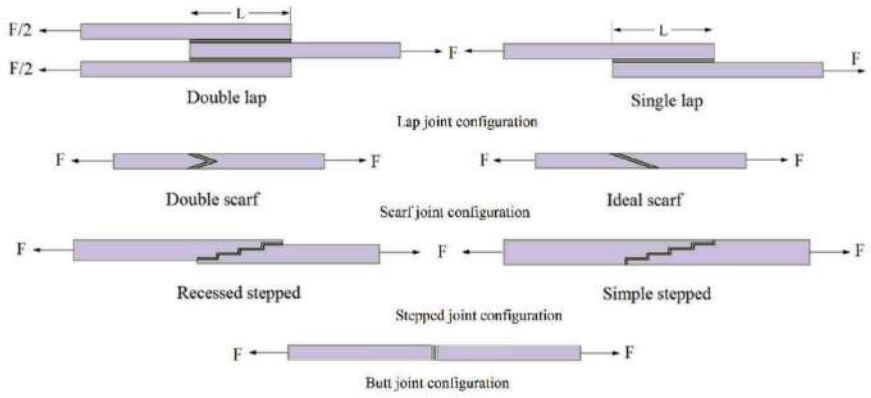

Figure 2.17: Different types of adhesive joints. Source: (Shishesaz & Hosseini, 2018).

2.2.4 Damage model - Cohesive zone modeling

The first theoretical models, proposed by authors such as Allman (1977), de Bruyne (1944), Goland and Reissner (1944), Tsai et al. (1998), and Volkersen (1938), have served to show the stress distributions in the adhesive and to identify the critical points. However, they also pose significant limitations with the inclusion of a non-linearity, such as plasticity in localized areas (Da Silva & Campilho, 2012). In recent years, a large part of the research has been devoted to quantify the damage sustained by the adhesive joint, allowing for more precise predictions (Budhe et al., 2017). Precisely, cohesive zone modeling or CZM is a damage model that allows to model the zone where the material separation is predicted to occur. The main advantage of using CZM is that it is easily integrated into FEM software, and some packages such as Ansys and Abaqus already include it in some form.

The concept of damage due to static loads before the start of fracture was developed first in the 1960s by Barenblatt (1959, 1962) and Dudgale (1960). The general idea of

CZM is to model the fracture zone, in this case the adhesive, with cohesion elements able to separate. This type of models require to know the surface or path that the fracture follows beforehand. Using the so-called traction-separation law (CZM law) in the fracture zone (see Fig. 2.18), the damage can be modeled as the formation and growth of an artificial crack. The crack can be located in the adhesive itself, as shown in Fig. 2.19.

The concept of damage caused by static loading before the apparition of cracks was developed in th early 1960s by authors such as Barenblatt (1959, 1962) and Dudgale (1960). The general idea of CZM is to model the fracture zone, or the adhesive, with cohesion elements that can separate. This modeling technique requires the knowledge of the crack path beforehand in order to add the cohesive elements, which is adequate for adhesive joints. The cohesion elements are defined using a traction-separation law (T-s law) or CZM law, as seen in Fig. 2.18. This law includes the formation and growth of an artificial crack. The cohesive elements can be defined in the mid-surface of the adhesive, as seen in Fig. 2.19, or in the middle of the plies in the case of a laminated composite. Authors such as Heshmati et al. (2018), Neto et al. (2012), and Senthil et al. (2018), among others, have used CZM to study multimaterial joints with accurate results.

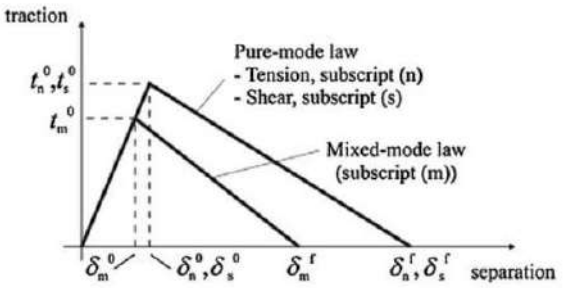

Figure 2.18: Example of a triangular CZM. Source: (Da Silva & Campilho, 2012).

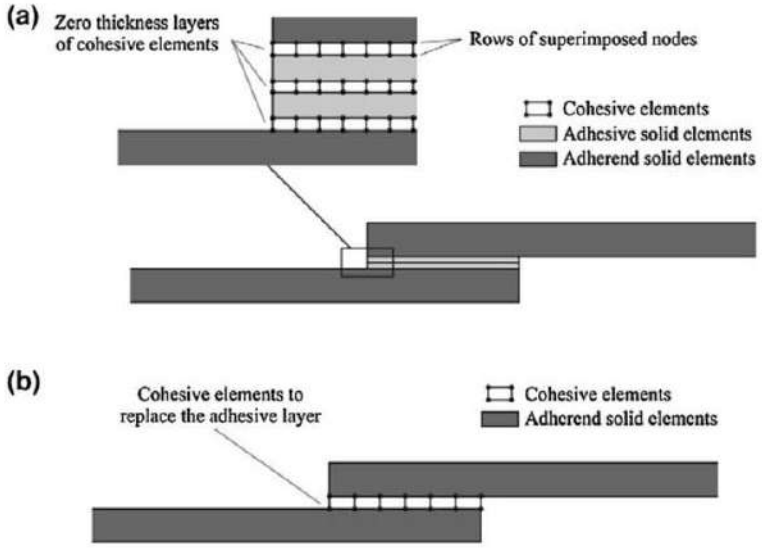

Figure 2.19: Cohesion elements to simulate a crack with no thickness. Source: (Da Silva & Campilho, 2012).

Even though there are research and developments using CZM, this modeling technique

is still to be used widely in the industry. According to Budhe et al. (2017), the lack of use in the industry comes from the high computational costs associated with the mesh-size required. Even when works such as those by Y. T. Kim et al. (2011) showed options to reduce simulation times, there is still room for development.

2.3 Calculation methods

In order to quantify the rollover crashworthiness of a structure, as well as to incorporate the collapse behavior of the shape with reinforcements and structural optimization a mechanical-mathematical model needs to be developed, that adequately represents one of the scenarios seen used by the Regulation 66. Also, complex and detailed FEM models are not completely adequate since many variations need to be tested, and the time required to run and analyze many different design points may be too large. Thus, different alternatives are explored.

2.3.1 Reduction of mechanical models

Static condensation

One of the most commonly used ways to reduce the problem dimension of large models is static condensation or Guyan condensation or reduction (Guyan, 1965). This technique reorders the system equations into those with master and slave degrees of freedom, which are those with and without applied forces, respectively. For a static analysis, where the stiffness of the system $[K]$ and the displacements of each degree of freedom (DoF) q are related to the applied forces F (see Eq. 2.21), the system equations is reorganized with the master DoF first (subindex m), followed by the slave DoF (subindex s), as seen in Eq. 2.22. Note that the terms off the diagonal represent the relationships between the slave and master DoF.

$$[K]q = F \tag{2.21}$$

$$\begin{bmatrix} k_{mm} & k_{ms} \\ k_{sm} & k_{ss} \end{bmatrix} \begin{Bmatrix} q_m \\ q_s \end{Bmatrix} = \begin{Bmatrix} F_m \\ 0 \end{Bmatrix} \tag{2.22}$$

The system equation can be separated into:

$$[k_{mm}]q_m + [k_{ms}]q_s = F_m \tag{2.23}$$

$$[k_{sm}]q_m + [k_{ss}]q_s = 0 \tag{2.24}$$

With the previous equations, an expression for the displacement vector q can be obtained as follows:

$$q = \begin{Bmatrix} q_m \\ q_s \end{Bmatrix} = \begin{bmatrix} I \\ -k_{ss}^{-1}k_{sm} \end{bmatrix} q_m = [T_G]q_m \tag{2.25}$$

The term $[T_G]$ is known as the Guyan transformation matrix, and it is used to obtain the reduced stiffness $[k_G]$ and mass $[m_G]$ matrices of a system:

$$[k_G] = [{T_G}^{\mathrm{T}}][K][T_G] \tag{2.26}$$

$$[m_G] = [{T_G}^{\mathrm{T}}][m][T_G] \tag{2.27}$$

Even when Guyan's reduction is one of the most commonly used for static problems, it has low accuracy for dynamic problems since Guyan only sees the relationship between the master and slave degrees of freedom, and does not take into account the dynamic characteristics of the system (Qu, 2004).

Dynamic condensation

Most of the adaptations of static condensation used for dynamic analyses carry approximation errors and are only valid for a certain range of frequencies. Furthermore, when the Guyan condensation is used to obtain a reduced mass matrix, it does not take into account the inertial effects. Dynamic condensation solves this issue by using the dynamic equation of movement (in terms of the eigenvalues λ and the eigenvectors φ) to separate the master and slave degrees of freedom:

$$([K] - \lambda[m])\varphi = 0 \tag{2.28}$$

$$\left(\begin{bmatrix} k_{mm} & k_{ms} \\ k_{sm} & k_{ss} \end{bmatrix} - \lambda \begin{bmatrix} m_{mm} & m_{ms} \\ m_{sm} & m_{ss} \end{bmatrix} \right) \begin{Bmatrix} \varphi_m \\ \varphi_s \end{Bmatrix} = \begin{Bmatrix} 0 \\ 0 \end{Bmatrix} \tag{2.29}$$

$$[D]\varphi = 0 \tag{2.30}$$

Thus, the dynamic stiffness matrix D can be defined, which can be used for condensation. Thus the reduced dynamic stiffness matrix D_R is deduced:

$$[D_R(\lambda)]\varphi_m = 0 \tag{2.31}$$

where $[D_R(\lambda)]$ is defined in terms of the known terms of the original stiffness and mass matrices:

$$[D_R(\lambda)] = (k_{mm} - \lambda m_{mm}) - (k_{ms} - \lambda m_{ms})(k_{ss} - \lambda m_{ss})^{-1}(k_{sm} - \lambda m_{sm}) \tag{2.32}$$

The matrix D_R can be then used to obtain the reduced mass m_R and stiffness k_R matrices, using Leung's theorem (Qu, 2004):

$$m_R(\lambda) = -\frac{\partial D_R(\lambda)}{\partial \lambda}, \quad k_R(\lambda) = D_R(\lambda) + \lambda m_R \tag{2.33}$$

Note that all the reduced matrices depend on an unknown eigenvalue λ. If $\lambda = 0$ is chosen, then the reduction behaves as Guyan's static condensation. A narrow space of frequencies (and thus eigenvalues) that produces a low variation of m_R is usually searched.

Salvini and Vivio (2007) stated that if two mechanical systems have the same properties and mass distribution but different stiffness matrices, then they should not have different reduced mass matrices. For this reason, they proposed a dynamic condensation method based on a homogeneous stiffness matrix, that guarantees the conservation of mass during the reduction.

Component mode synthesis (CMS)

CMS is one of the most commonly used methods to reduce the number of DoF of mechanical systems. According to Qu (2004), the following steps can be followed for CMS:

1. The original structural problem is divided into components or substructures.
2. FEA (or similar methods) is applied to formulate a discrete model for each component separately. The advantage is that a reduced model can be applied for each component. The reduced models can be obtained either by mathematical formulations or experimentally, for instance, testing of a joint.
3. The reduced models can then be assembled to obtain the global model. The reduced model has a smaller size than a model obtained by discretizing the whole system.
4. Structural analyses can be performed on the reduced model, and the response on the coordinates of the reduced model can be even obtained using inverse substitution.

This technique can even be employed for the redesign and modifications of structures, as explored by Takewaki (1998). It should be noted that this method tries to maintain the same fundamental natural frequency of the original system, as well as the deformation ratios for the fundamental mode.

2.3.2 Concept modelling

Another technique commonly used to reduce the size of the mathematical problem consists of a reconceptualization of the problem. For instance, slender and thin-walled components can be modeled using beam and shell elements instead of more complex brick elements. This change can significantly reduce the size of the model, avoids certain convergence issues, and offers a similar accuracy as a full 3D model, as shown by Kuo et al. (2006). This technique can be extremely useful in the early stages of design, as new materials and geometries can be easily tested. It is also extremely useful for structural optimization, as the time required for function evaluations can be reduced significantly (J. Fang et al., 2017).

One of the main limitations with concept modelling is the model used for structural joints, since they cannot be directly replaced with beams and shells. To overcome this difficulty, joints can be either analyzed separately with reduction techniques (described in the previous section) and be included as a reduced model (see Fig. 2.20) as explored by authors such as Mundo et al. (2010), Mundo et al. (2011) and Stigliano et al. (2010); or they can be modeled as non-linear elements, with the characteristic curves obtained from experiments or theoretical models (Bai, Meng, & Zuo, 2019; Hamza & Saitou, 2003; Li et al., 2021; Weiß, 2018).

Mundo et al. (2010), Mundo et al. (2011) and Stigliano et al. (2010) developed a reduced model for a vehicle as a system of beams and panels, and the joints were modeled as superelements with the corresponding stiffness and mass properties. The accuracy of the reduced model was verified through two types of experiments: static bending and torsional load, and vibration analysis. No impact or rollover tests were carried out, which are important to assess the crashworthiness. The work of the aforementioned authors is summarized in Fig. 2.21.

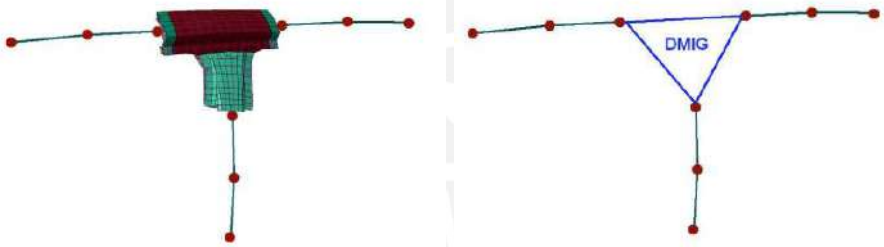

Figure 2.20: Condensation of a joint. Source: (Mundo et al., 2010)

Another application of concept modelling lies in NVH[6] studies. For instance, Doke et al. (2012), Fard and Liu (2015), and Nasrolahzadeh et al. (2013) developed a FEM reduced model of the body-in-white of a vehicle, based on dynamic testing, as seen in Fig. 2.22. Doke et al. (2012) even applied a second Guyan's reduction to the beam - shells for further reduction.

On the other hand, Hamza and Saitou (2003) developed a model to address the crashworthiness of vehicle structures. The model consists of an equivalent plane mechanism, with non-linear springs that represent the structural elements and lumped masses. The author managed to perform the optimization of the structure using a simple model. This would help designers with a fast tool to evaluate different geometries and parameters.

More recently, Weiß (2018) used a simplified model to evaluate the crashworthiness of the fuselage of an airplane, an optimize the position of structural joints made of composite

[6]Noise, vibration and harshness.

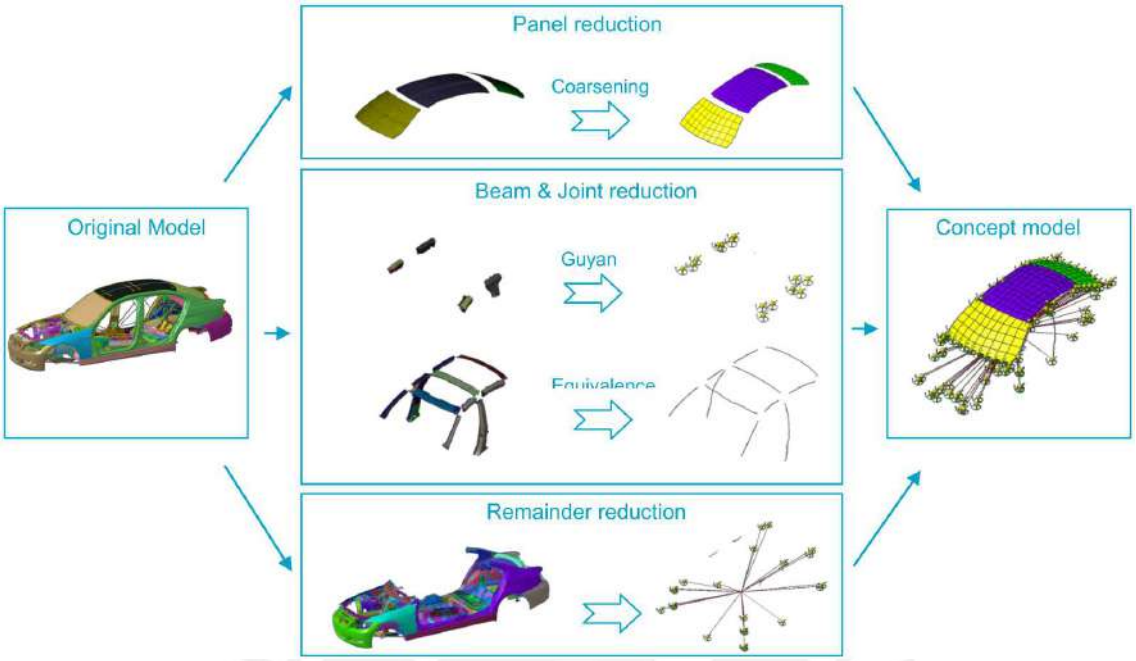

Figure 2.21: Workflow for concept modelling. Source: Stigliano et al. (2010).

materials. In the simplified model, the panels are represented as beam elements connected with non-linear springs as seen in Fig. 2.23. The author showed that by using a simplified model, the time required for each evaluation of the objective functions can be extremely reduced, even with the 40 design variables involved.

2.3.3 Crashworthiness studies with bending collapse

Analysis of rollover crashworthiness and energy absorption of an structure can be performed either with highly detailed models or with simplified models that incorporate the plastic behavior of certain components, i.e. the structural nodes. This behavior can be obtained via experimental tests, detailed numerical models of the nodes, or with theoretical models (such as the ones described for bending collapse shown in Section 2.1.3).

Authors such as Kang et al. (2012) and Liang and Le (2009, 2010a, 2010b), among others, used detailed models for the analysis, design and optimization of the structure. This models typically use SHELL elements for the dynamic simulations. However, they define a function for certain parameters for optimization.

Incorporating the response of a structural node on a concept model has enormous advantages. Authors such as Bai, Meng, Wu, et al. (2019), Bai, Meng, and Zuo (2019), Gui et al. (2018), Li et al. (2021), and Park and Yoo (2008) reached the conclusion that using a concept model, together with the experimental collapse curves of structural nodes, produces a response with similar accuracy as a detailed model with a significant reduction in modelling and calculation time, as shown in Fig. 2.24.

Since they require a reduced computation time, simplified conceptual models can be used to study the sensitivity of a model to certain variable changes, as well as to generate the "exact" responses required to develop surrogate models or metamodels, or used as fast calculation tool in the early design stages.

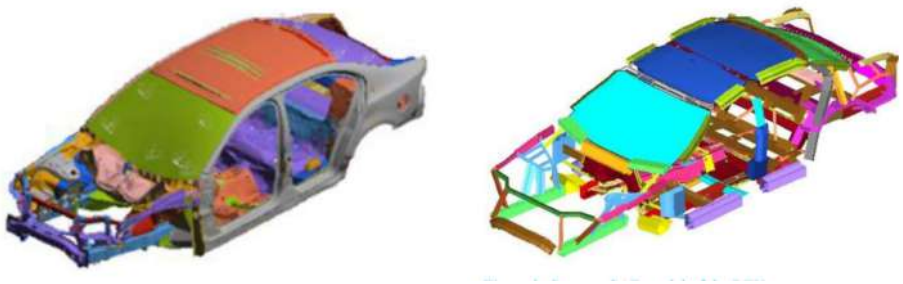

Figure 2.22: Example of the reduction of a complex vehicle model into a simplified model composed of beams and shells. Sources: Fard and Liu (2015) and Nasrolahzadeh et al. (2013).

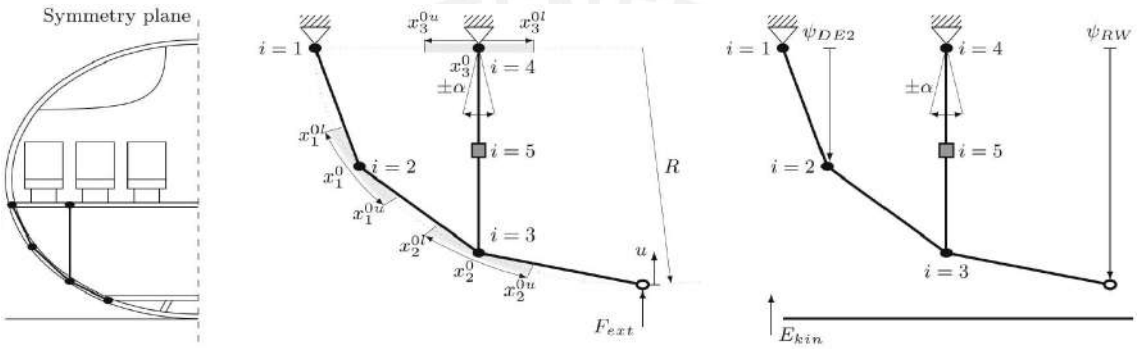

Figure 2.23: Scheme of the simplified model used by Weiß (2018).

2.3.4 Surrogate models or Metamodels

Finite element simulations may require a long time to calibrate, converge and find the adequate response. Although it is not an issue when analyzing a single structure one-time, it can become a serious limitation when multiple iterations are required during design and optimization; as the latter requires multiple evaluations, in this case, simulation runs. This can make optimization problems unbearable and almost impossible to finish. To overcome this difficulty, a surrogate model or metamodel can be a great aid, and they are one of the most commonly used tools for structural optimization (J. Fang et al., 2017).

The metamodels can be based on finite element simulations or experimental tests (Song et al., 2013; Su et al., 2011; Xie et al., 2018; Xiong et al., 2018; F. Xu et al., 2013; K. Xu et al., 2020; R. Z. Xu & Zhou, 2011). In general, metamodels have a straightforward procedure:

1. Design of Experiments (DoE): A DoE explores the design space of a selected number of variables, and samples a number of design points at which the response will be determined. Factorial design and Latin Hypercubes are among the most commonly used methods of DoE.

2. Actual response calculation: The response or output variable(s) is determined at the selected design points, this response points are used to generate the hypersurface of the surrogate model.

3. Generation of the metamodel: The metamodel is built using one of several techniques for interpolation. The selection depends on the complexity and non-linearity of the

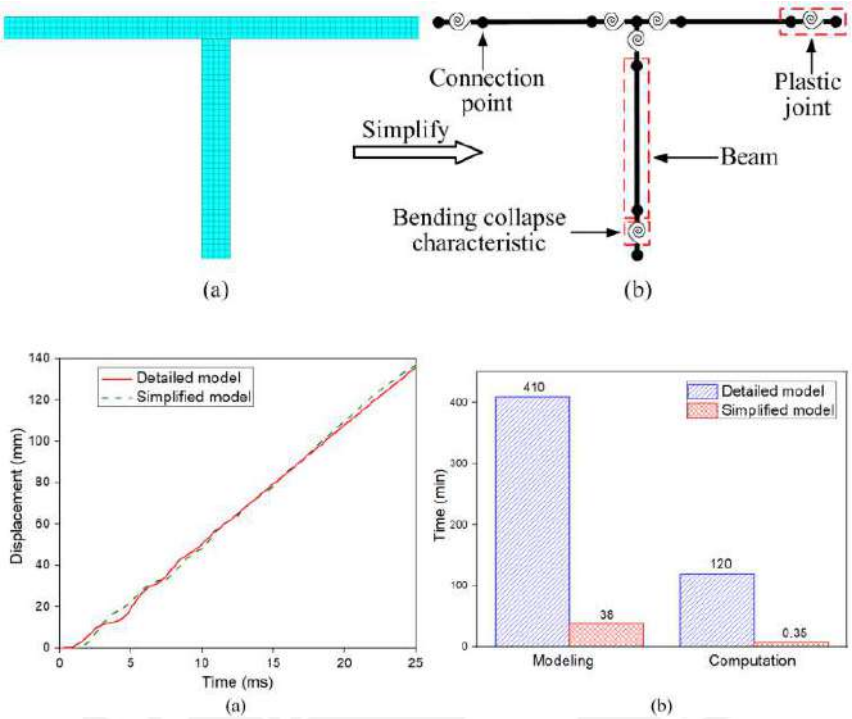

Figure 2.24: Example of a simplified joint using non-linear springs to incorporate bending collapse curves and its effect on the accuracy and modelling and computation time. Source: Li et al. (2021).

response. Some of the methods are explored below.

The steps described above can be further summarized in Fig. 2.25.

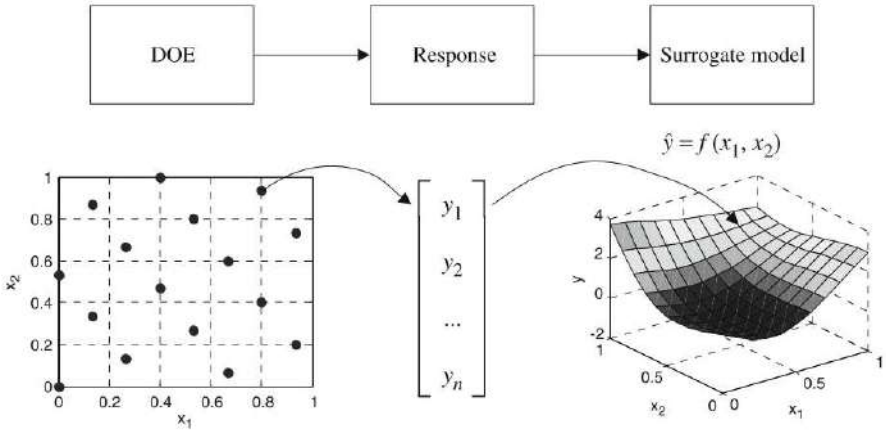

Figure 2.25: General procedure to develop a metamodel. Source: Su et al. (2011).

Response Surface Methodology (RSM)

RSM is one of the most commonly used methods for structural optimization and adequate for non-linear responses. This method is vastly described by authors such as Montgomery (2017), Myers et al. (2016), and Roux et al. (1998). RSM obtains an approximated response $\hat{y}$ based on a series of base functions ϕ and regression coefficients β, as seen in Eq. 2.34, which are obtained using the exact responses y_i from the DoE.

$$y(x) = \sum_{i=0}^{L} \beta_i \phi_i(x) + \epsilon \tag{2.34}$$

where the functions $\phi_i(x)$ are generally second grade polynomials of the shape:

$$1, x_1, x_2, ...x_m, x_1^2, x_1x_2, ..., x_m^2$$

In general, the $\phi_i(x)$ functions can be assembled following Pascal triangle rule, thus Eq. 2.34 takes the following form:

$$y(x) = \beta_0 + \beta_1 x_1 + \beta_2 x_2 + ... + \beta_m x_m + \beta_{11} x_1^2 + \beta_{12} x_1 x_2 + ... + \beta_{mm} x_m^2 + \epsilon \tag{2.35}$$

Grouping terms together and establishing $x_1^2 = x_{m+1}$, $x_1x_2 = x_{m+2}$,...$x_m^2 = x_k$, the following general expression is obtained:

$$y(x) = \beta_0 + \beta_1 x_1 + \beta_2 x_2 + ... + \beta_k x_k + \epsilon = \beta_0 + \sum_{j=1}^{k} \beta_j x_j + \epsilon \tag{2.36}$$

The calculation of the regression coefficients β is based upon the n sample design points of k variables, at which the actual response y_i is known. Thus, n equations can be written using Eq. 2.36, as follows:

$$y_i = \beta_0 + \sum_{j=1}^{k} \beta_j x_{ij} + \epsilon_i, \quad i = 1, 2, ..., n \tag{2.37}$$

or in matrix form:

$$\mathbf{y} = \mathbf{X}\beta + \epsilon \tag{2.38}$$

where:

$$\mathbf{y} = \begin{bmatrix} y_1 \\ y_2 \\ \vdots \\ y_n \end{bmatrix}, \quad \mathbf{X} = \begin{bmatrix} 1 & x_{11} & x_{12} & ... & x_{1k} \\ 1 & x_{21} & x_{22} & ... & x_{2k} \\ \vdots & \vdots & \vdots & \vdots & \vdots \\ 1 & x_{n1} & x_{n2} & ... & x_{nk} \end{bmatrix}, \quad \beta = \begin{bmatrix} \beta_0 \\ \beta_1 \\ \vdots \\ \beta_k \end{bmatrix}, \quad \epsilon = \begin{bmatrix} \epsilon_1 \\ \epsilon_2 \\ \vdots \\ \epsilon_n \end{bmatrix}$$

To obtain the best approximation $\mathbf{b}$ of β, that minimizes the error term ϵ, the least square method is used. In this method, L is defined and minimzed, as follows:

$$L := \sum_{i=1}^{n} \epsilon_i^2 = \epsilon'\epsilon = (\mathbf{y} - \mathbf{X}\beta)'(\mathbf{y} - \mathbf{X}\beta) \tag{2.39}$$

The details of the minimization can be found in (Myers et al., 2016), and $\mathbf{b}$ is found:

$$\mathbf{b} = (\mathbf{X}'\mathbf{X})^{-1}\mathbf{X}'\mathbf{y} \tag{2.40}$$

Thus, the approximation $\hat{\mathbf{y}}$ of y is determined:

$$\hat{\mathbf{y}} = \mathbf{X}\mathbf{b} \tag{2.41}$$

Radial basis function networks (RBF)

Another widely used method in structural optimization, which rollover crashworthiness for different vehicles is RBF (Amouzgar & Strömberg, 2017; S. Chen et al., 1996; Hardy, 1971; Shi et al., 2012; Song et al., 2013; Su et al., 2011; Sun et al., 2010; F. Xu et al., 2013). This method also offers adequate and accurate approximations of non-linear system respones (H. Fang et al., 2005; Su et al., 2011), as seen in Fig. 2.26. In some cases, RBF can be combined with RSM to obtain an even more complex metamodel.

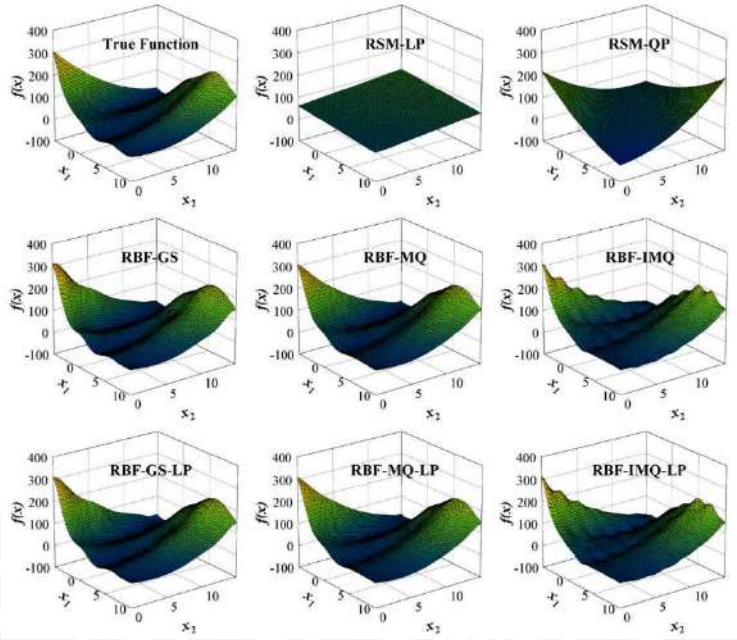

Figure 2.26: Approximation examples of the highly non-linear function "Branin rcos" using different RSM and RBF based metamodels. Source: H. Fang et al. (2005).

The procedure of using RBF is similar to the one used in RSM for Eq. 2.34 and can be written in the following form:

$$y(\mathbf{x}) = \sum_{i=1}^{n} \lambda_i \phi(\|\mathbf{x} - \mathbf{x_i}\|) + \sum_{j=1}^{m} c_j p_j(\mathbf{x}) \tag{2.42}$$

where n is the number of sample points where y is calculated, $\mathbf{x}$ is the vector of design variables, $\mathbf{x_i}$ is the vector of the sample design points, $\|\mathbf{x} - \mathbf{x_i}\|$ is the euclidean distance between points, λ_i is the vector of unknown weight factors, and ϕ are the base functions, which can have different shapes as seen in Table 2.2 and Fig. 2.27.

Table 2.2: Basis functions used in the RBF method. Adapted from: Sun et al. (2010).

Name	Abbrev.	$\phi(r = \|\mathbf{x} - \mathbf{x_i}\|)$
Cubic	RBF-CB	$\phi(r) = r^3$
Thin-plate spline	RBF-TPS	$\phi(r) = r^2 \ln(r)$
Gaussian	RBF-GS	$\phi(r) = e^{-kr}, \quad 0 < k$
Multi-quadratic	RBF-MQ	$\phi(r) = \sqrt{r^2 + k^2}, \quad 0 < k$
Inverse multi-quadratic	RBF-IMQ	$\phi(r) = \frac{1}{\sqrt{r^2+k^2}}, \quad 0 < k$

Additionally, Eq. 2.42 includes a series of polynomial terms $c_j p_j$ (as those shown in RSM), which greatly improve the approximation of linear systems. This method is usually

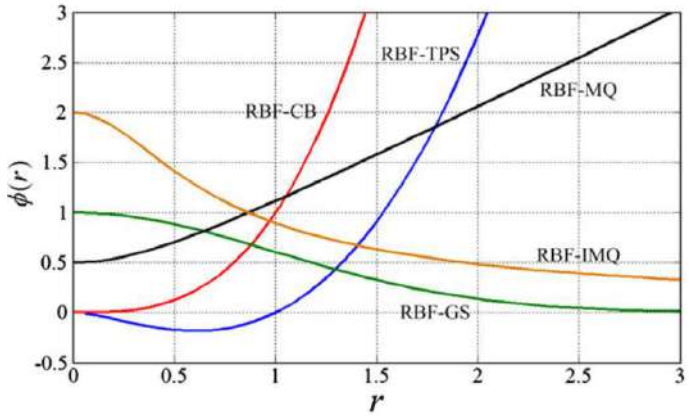

Figure 2.27: RBF basis functions. Source: Sun et al. (2010).

known as Augmented Radial Basis Functions (ARBF) or Hybrid Radial Basis Functions (HRBF) in the literature (H. Fang et al., 2005; Su et al., 2011). However, including these terms in Eq. 2.42 increases the number of unknowns beyond the number of available equations. To overcome this problem, an orthogonality condition is introduced for the λ coefficients:

$$\sum_{i=1}^{n} \lambda_i p_j(x_i) = 0, \quad j = 1, 2, ..., m \tag{2.43}$$

Thus, by combining Eqs. 2.42 and 2.43 for each design points where y is known, the following system can be established:

$$\begin{bmatrix} \mathbf{A} & \mathbf{P} \\ \mathbf{P}' & \mathbf{0} \end{bmatrix} \begin{bmatrix} \boldsymbol{\lambda} \\ \mathbf{c} \end{bmatrix} = \begin{bmatrix} \mathbf{y} \\ \mathbf{0} \end{bmatrix} \tag{2.44}$$

where $\mathbf{A}_{i,j} = \phi(\|\mathbf{x_i} - \mathbf{x_j}\|)$, $\mathbf{P}_{i,j} = p_j(\mathbf{x_i})$, $(i = 1, 2, ..., n, j = 1, 2, ..., m)$, $\boldsymbol{\lambda} = [\lambda_1, \lambda_2, ..., \lambda_n]'$ and $\boldsymbol{c} = [c_1, c_2, ..., c_m]'$. System of Eqs. 2.44 is actually composed of $n + m$ equations, from which factors λ_i and c_j can be determined. It is worth noting that the RBF approximation passes through all sample design points, which means it is impossible to assess the accuracy of the approximation via ANOVA of the surveyed points.

Once the $\boldsymbol{\lambda}_i$ and c_i parameters are determined, they can be used in Eqs. 2.42 and 2.43 to obtain the approximated response at any other point. It should be noted once again, that the inclusion of the second term in Eq. 2.42, specifically $c_j p_j(\mathbf{x})$, is optional.

Artificial neural networks (ANN)

Another method that has gained popularity in the last years is ANN. It is a powerful method capable of formulating relationships between complex sets of input and output variables (J. Fang et al., 2017). An ANN can be composed by a set of layers that perform weighted sums of the previous layer and produce an output value used by the neurons in the next layer. Similar to the previously described methods, an ANN requires the initial data of design points and their responses in order to "train" the network. The training is performed by changing the values of weights (and bias) in each neuron of each hidden layer of the neural network. An example of an ANN is shown in Fig. 2.28.

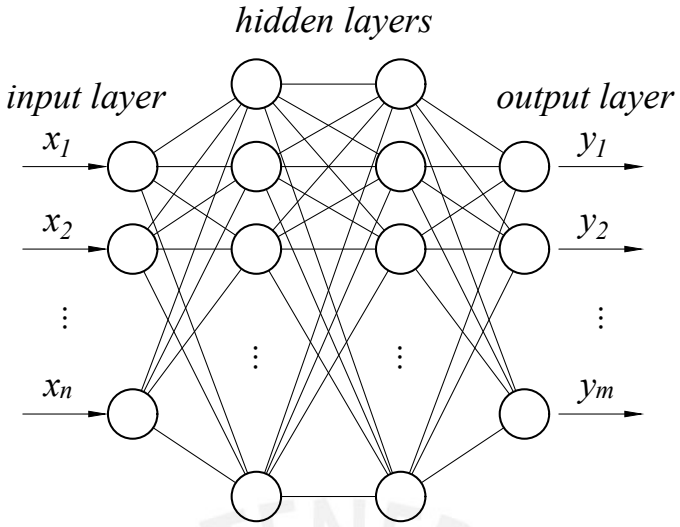

Figure 2.28: Example of a 4 layer neural network.

2.4 Design of Experiments (DoE)

A fundamental step for the development of simplified models, surrogate models, and optimization in general, is the exploration of the design space, by obtaining the actual response y for a series of design points x. Choosing the relative distance and distribution of the design points x is vital for the accuracy of the prediction of the response y (Christensen & Bastien, 2016a), as it allows to:

- determine which variables have a larger influence on the structural response y.
- identify which components have a lesser influence on the response y and can be omitted.
- obtain a representative sample which provides good approximations for y.

2.4.1 Full factorial design (FFD)

A straightforward technique is to fill the design space with a large number of points. Each point is located at every value of every design variable x, making a grid of design points. If there are G variables with k levels of values each, then $N_s = G^k$ experiments must be performed. Although easy to implement, this may require an incredibly large number of experiments, tests or simulations, which may render FFD unfeasible. An example is shown in Fig. 2.29.

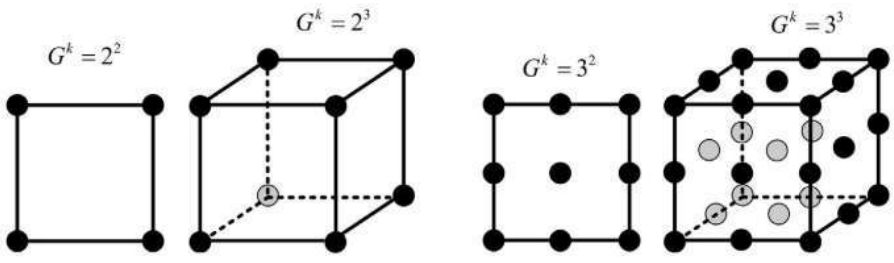

Figure 2.29: Example of a full factorial design. Each axis represents a variable. Source: Christensen and Bastien (2016b).

2.4.2 Latin Hypercube Sampling (LHS)

Latin Hypercube sampling, initially described by Mckay et al. (1979) and later expanded by Florian (1992), Olsson et al. (2003), Shields and Zhang (2016), Stein (1987), and B. Tang (1993), is an alternative to obtain a DoE with a lower number of sample point and similar accuracy as FFD. This technique has been widely used for structural optimization of vehicle structures (Amouzgar & Strömberg, 2017; Christensen & Bastien, 2016b; Chuang et al., 2008; Shi et al., 2012; Song et al., 2013; Su et al., 2011; Sun et al., 2010; Xiong et al., 2018; F. Xu et al., 2013; K. Xu et al., 2020; Zhao & Xue, 2010). According to del Castillo (2007), the LHS can be performed following the next steps:

1. Divide each of the k variables into n intervals, and thus generating n^k cells.
2. Select one cell randomly and pick up a point inside this cell randomly.
3. Cross out all cells that share the same coordinates as the selected cells and mark them as occupied.
4. Continue the process of randomly selecting cells that have not been marked yet.
5. If n cells have been selected, all required points are obtained.

Even when the selection process is random, there is a chance that points may cluster in certain areas. To guarantee a uniform spread, the following techniques can be applied:

- Maximum distance criterion: The minimum distance between any two sample points is maximized.
- Minimum correlation criterion: The correlation between the variables is minimized.

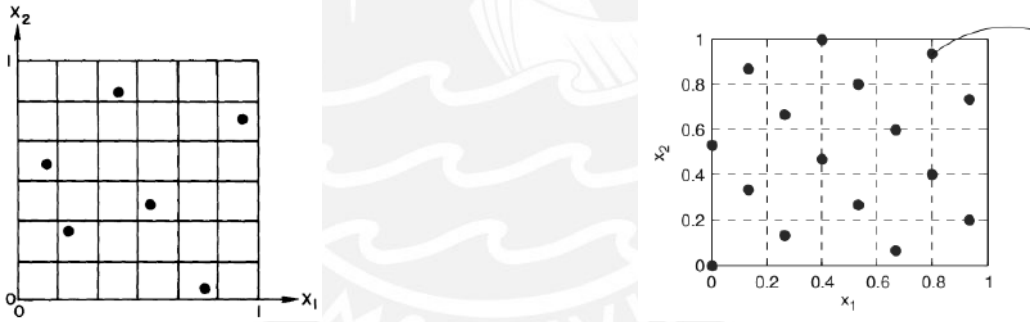

Figure 2.30: Example of sample points obtained using a purely random LHS (left) and an orthogonal LHS (right). Sources: Stein (1987) y Su et al. (2011).

2.5 Concretization of thesis goals

Existing literature shows that there has been a significant amount of research, advances and developments in the crashworthiness of structures during rollover accidents. In this matter, the use of Regulation 66 is mandatory. There has also been advances in the use of composite materials and multimaterial structures, as well as in numerical models to tackle large size problems. From the literature, the use of concept modeling seems to be adequate for the analysis of a bus structure. However, there has only been a handful of works regarding this technique. Furthermore, the use of metamodels appears to be the best way to address the sometimes unbearable computation times during optimization.

As previously discussed in Section 2.1, the structural loops or rings are responsible for most of the energy absorbed during a rollover accident, particularly in the zones near the nodes, that is, the joint between floor and column, column and waist-rails and columns and roof. The behavior of these areas is typically that of bending collapse, and thus, a

numerical and theoretical model is required. Existing theories work well with very thin-walled shapes; however, commercial shapes do not always comply with the existing theories since they have larger thicknesses. Furthermore, theoretical models of bending collapse for reinforced and partially reinforced shapes are still in development. Thus, the need of a theoretical model for shapes with greater thicknesses appears. Also, a theoretical model for reinforced shapes needs to be developed. These theoretical models can be incorporated in the concept model of the bus for rollover analysis.

The use of composite materials in the automotive industry has been on the rise in the last decades, mainly due to the composites' high specific mechanical properties. However, attempts to use composites as main structural parts have resulted in costly projects that may not be financially feasible for the industry. However, this difficulty may be overcome by by using multimaterial structures. In this work, structures with partial and localized reinforcements are proposed, since the bending collapse occurs only in the vicinity of the structural joints.

A comparison of the crashworthiness of the bus structure with and without reinforcements can then be performed, following the specifications of Regulation 66. This comparison can be done in terms of the absorbed energy and overall weight. Concept modeling can be used for to build the models for comparison and an optimization of the structure with and without reinforcements.

Chapter 3

Bus super-structure description and preliminary analysis

3.1 Description of the study case

Previous studies, such as those by Gepner et al. (2014), G. Zhang et al. (2011), and Zhou et al. (2019), among others, show that the structural rings or loops are responsible for most of the absorbed energy during a rollover test. In Fig. 3.1, a section of the super-structure a bus is displayed, in which the structural rings are painted purple. Notice that the rings include the columns, floor and roof. According to UN/ECE 66 (2007), an alternative to the rollover test in laboratory is the calculation of the structural components with experimental information as input. In this study, the structure shown in Fig. 3.1 is used as study case. This structure has been previously used for studies at UC3M. This structure also complies with the requirements of R66 as well as the recommendations suggested by Roca et al. (1997), regarding the good design practices for rollover crashworthiness of bus structures.

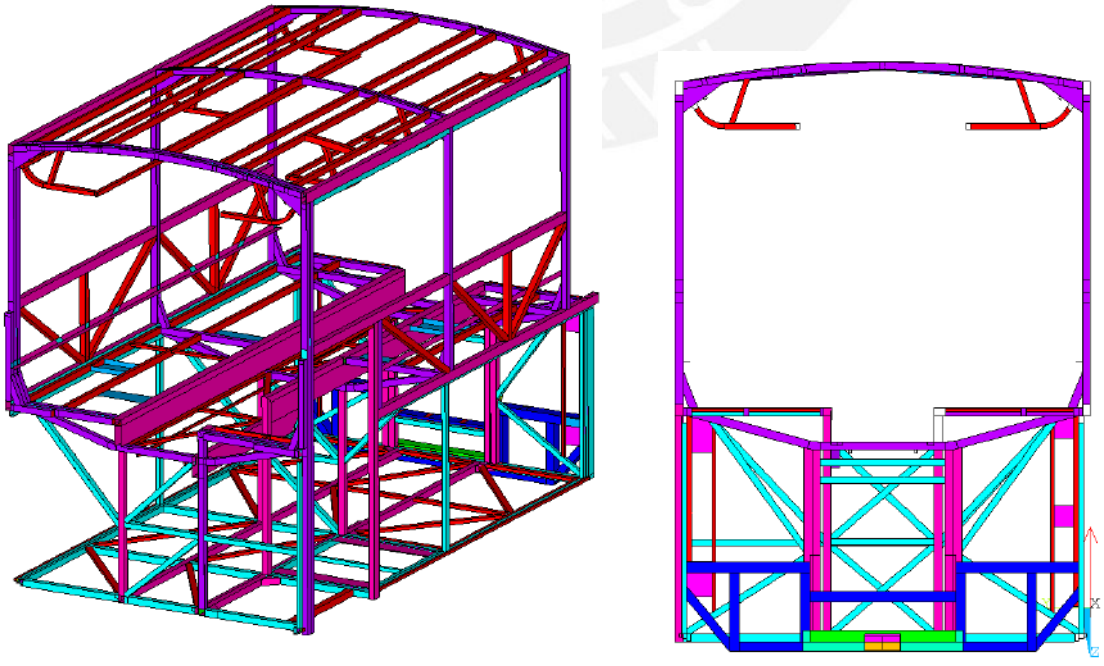

Figure 3.1: Reference bus super-structure for study. Courtesy of MECATRAN - UC3M.

3.2 Initial analysis

3.2.1 Elastic analysis

Due to the nature of the structure, the structural shapes that form the columns, roof and floor can be condensed in a concept model with BEAM elements, that is, Timoshenko-beam line elements, as shown in Fig. 3.2. An initial elastic analysis of the structures, confirms that the critical zones are located in the joints of column-floor and column-roof. As such, they require further detailed analysis.

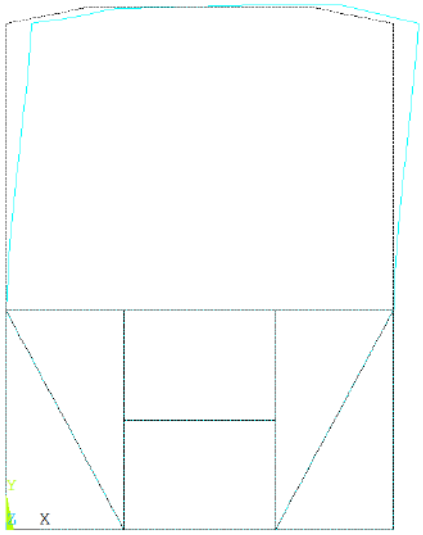

Figure 3.2: Comparison of the undeformed and deformed shape of the super-structure under a static load.

3.2.2 Joint analysis

Following the confirmation of the critical zones of the structure, a more detailed analysis of the joints is performed. In this case, the floor-column joint is analyzed to identify the failure mechanism. Furthermore, the inclusion of a stiffener is also evaluated. The analyzed joints are shown in Fig. 3.3 and are made of ASTM A500 Steel. The mechanical properties used for the model are summarized in Table 3.1. Since rollover crashworthiness involves plastic deformations, a bilinear isotropic hardening rule is used for plasticity.

Table 3.1: Mechanical properties of steel ASTM A500 (2018) for the structure shown in Fig. 3.1.

Property	Value	
Young modulus E_{st}	200	GPa
Poisson ratio ν_{st}	0.3	
Yield strength σ_{Y-st}	290	MPa
Ultimate strength σ_{B-st}	400	MPa
Minimal elongation (50 mm ref.) ΔL_{min}	23	%
Tangential modulus E_{T-st}	0.5% E_{st}	GPa

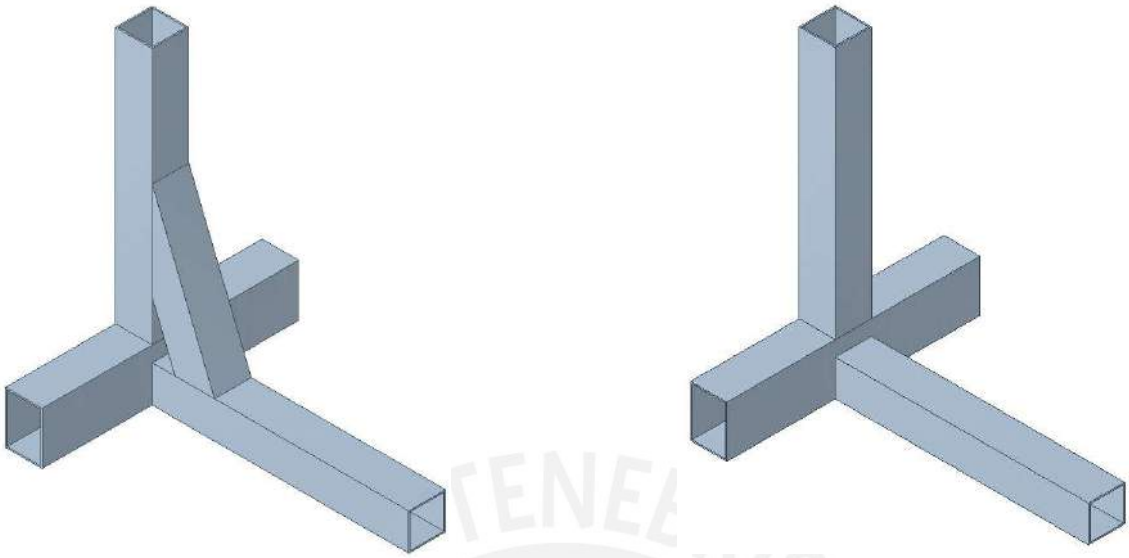

a) b)

Figure 3.3: 3D model of the structural column-floor joint, a) with and b) without stiffener.

The value of 0.5% of the Young's modulus for the tangential modulus produces a value of 1000 MPa, which is in range of the tangential moduli used by various researchers in different fields (Lotfollahi et al., 2016; Nargund & Williams, 2016; Rincón-Dávila et al., 2019). Further studies require validation of the hardening model via experiments, a multilinear isotropic hardening rule based also on experiments is also a viable option.

The structural node is modeled using 8-node SHELL elements (SHELL281) in Ansys Classic. It is then connected to BEAM elements of the same cross section, using rigid contact elements (node-to-line contact), as shown in Fig. 3.4. The boundary conditions are then applied to the free-end of each of the line segments. The ends that correspond to the floor-rails are fixed, whereas the one corresponding to the column is subjected to a horizontal displacement of ±200 mm, to replicate the behavior of both sides of the structure. Since the model is connected to the boundary conditions using beam elements, it can also be rapidly incorporated into the concept model of the super-structure.

Remark 3.1 *The connection between the BEAM and SHELL elements can be performed in different manners. Several of them where explored during the development of the thesis. The main objective of the connection is to transfer the loads seamlessly between the elements, for both small and large displacements. A common way of connecting this types of elements is via constraint equations. The node at the end of the beam element is regarded as the master node, and the nodes at the shell elements are named slave nodes. The program then establishes kinematic compatibility equations between the displacements of the master and slave nodes. An alternative form of connecting both types of elements is via rigid link elements. However, it was found these two methods are only adequate for small displacements. Instead, a rigid contact between the master and slave nodes is established. In this way, the loads are adequately transferred between nodes with large displacements, albeit with a small discontinuity in the stress field.*

A similar analysis is also performed on a joint without the stiffener to observe its effect on the strength of the structure. Both models are evaluated with loads that "open" and "close" the joint, and the rotation of the plastic hinge is measured, as seen in Fig 3.5. It

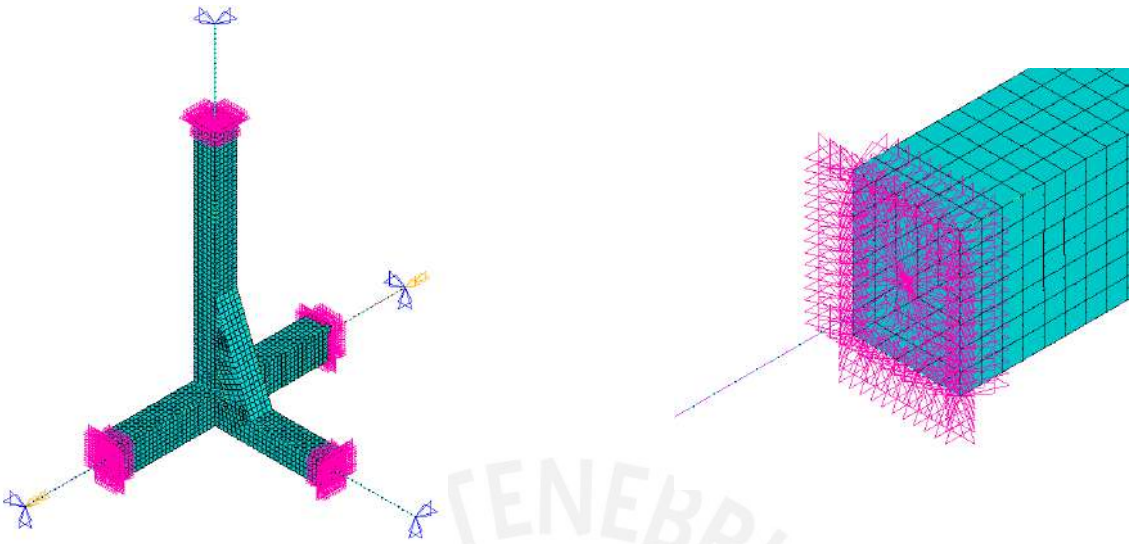

a) b)

Figure 3.4: a) FEM model of the structural node and its boundary conditions. b) Detail of the BEAM-SHELL connection using contact elements.

is worth noting that both curves (with loads in the opposing directions) are symmetrical, meaning that the stiffener has little influence on the plastic collapse hinge.

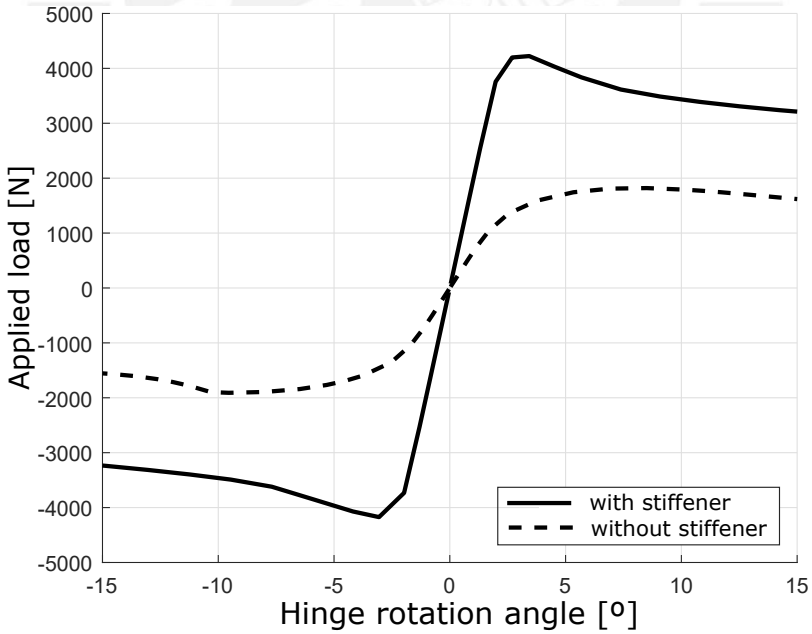

Figure 3.5: Load - deflection curve for the floor-column joint with and without reinforcement. The negative portion of the curve indicate that the joint is being "opened".

Although the improvement of the inclusion of stiffeners is rather obvious, in the whole super-structure, the stiffeners guarantee continuity in the structural loop or ring, as recommended by Roca et al. (1997). Furthermore, if the stiffener is not well connected or welded, then there will be no continuity, and the joint behaves as if the stiffener does not exist, as shown in Fig. 3.6. If continuity is not guaranteed it is unlikely that the

super-structure does not pass the rollover test specified in Regulation 66.

Figure 3.6: Example of stiffeners with an adequate (left) and inadequate (right) stiffener weld.

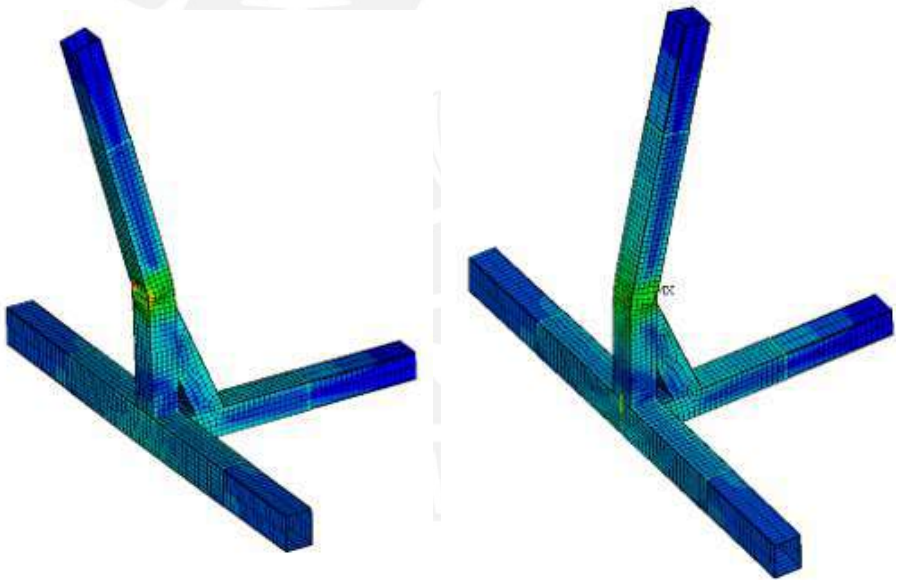

Figure 3.7: Equivalent stress distribution on the structural node when opening (left) and closing (right). The bending collapse zone concentrates most of the plastic deformations and absorbed energy.

Bending collapse is observed to be the main failure mode in both cases as shown in Fig. 3.7. The bending collapse behavior is described in the previous chapter for thin-walled shapes. It could be argued that the shape of the collapse zone is affected by the HAZ and the stiffener; however, research by Rincón-Dávila et al. (2019) has shown that this influence is minimal. Furthermore, this can be considered as an indication that the bending collapse models can be applied with the presence of the stiffener.

The collapse hinge concentrates most of the absorbed plastic energy, as depicted in Fig. 3.8. These results agree with those found by several authors of the surveyed literature, such as Hashemi et al. (2009) and Zhou et al. (2019) among others. In Fig. 3.9, the experimental test of a structural joint is displayed and similar to the numerical simulations, bending

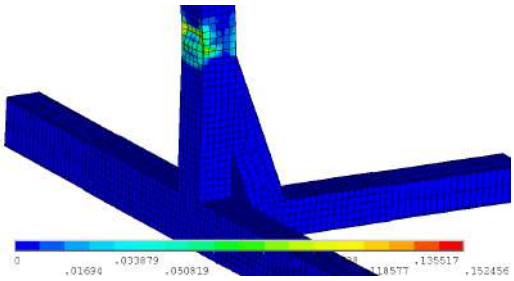

Figure 3.8: Detail of the plastic collapse zone. Note that it concentrates all the plastic deformations.

collapse is the main failure mode.

Figure 3.9: Bending tests performed on the structural joint of a bus. Note that the bending collapse is the dominant failure mode.

3.3 Initial proposal for composite reinforcements

Once the main failure mode has been identified and the influence of the stiffeners over the shape of the collapse zone regarded as negligible, proposals of reinforcements are posed. Since bending collapse is a localized phenomenon, the reinforcement can be applied near the joints. Furthermore, the reinforcements must not require large modifications to existing designs, since once of the goals is to keep the weight as low as possible. Large modifications could end up in large additional costs in research and development, since the influence on other design aspects would also be required to be accounted for, as established by H. E. Friedrich (2017) and Klein (2013).

Composites are optimal alternatives for reinforcements, since they can increase the stiffness and strength significantly without an important weight increase. Carbon fiber reinforced polymer (CFRP) is proposed as the material for the reinforcement. In order to join the CFRP with the structural steel, an adhesive joint is proposed. Several reinforcement configurations are proposed and evaluated in terms of their complexity, manufacturing requirements and costs.

3.3.1 Reinforcement proposal 1

The first proposed modification consists of replacing the stiffener (usually made from steel and welded) for a stiffener made from CFRP. Since bending collapse must be avoided

in both directions, two sets of reinforcements are designed, as shown in Fig. 3.10. All contacting zones are kept together with adhesives. The final joint is shown in Fig. 3.11.

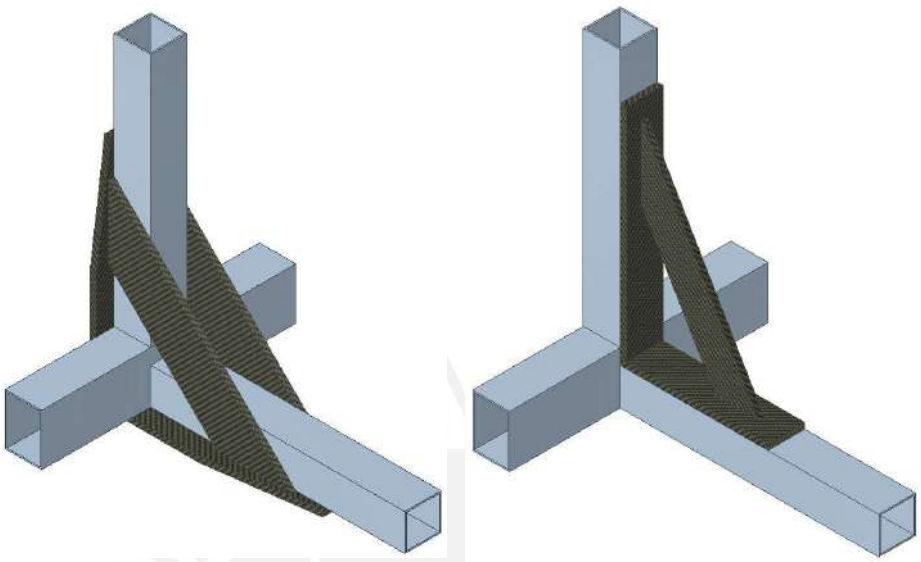

Figure 3.10: Parts of the reinforcement proposal 1.

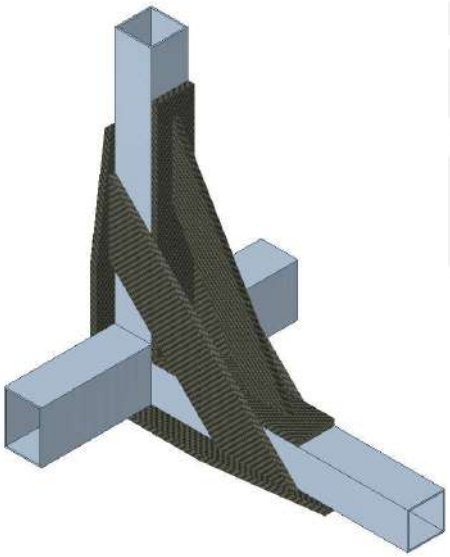

Figure 3.11: Reinforcement proposal 1.

The main advantage of the first proposal is that the geometry is fairly simple, as it is made from strips of CFRP. A small weight reduction is also made by replacing the steel stiffener by one of CFRP. Finally, there is no HAZ near the collapse zone, as the CFRP can be joined with adhesives. On the other hand, this proposal also has disadvantages. The main one is that the connection of the strips between the horizontal and vertical beams are critical. If the manufacturing process is not adequate, then the continuity of the structural loop may be compromised.

3.3.2 Reinforcement proposal 2

The second proposal is based on the work by Galvez et al. (2017) and is depicted in Fig. 3.12. This proposal consists of replacing the structural node with a core made from CFRP. The core has extensions that can be inserted in the rest of the structure. The core itself has a stiffener incorporated for higher stiffness and overall strength.

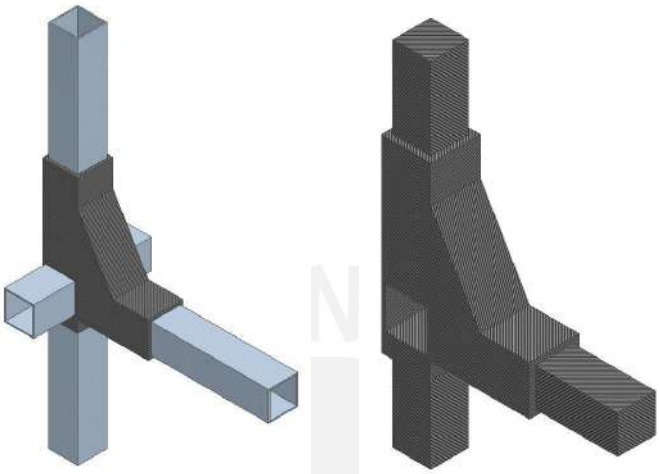

Figure 3.12: Reinforcement proposal 2. Left: reinforcement assembled on the node. Right: node made of CFRP.

The main advantage of this proposal is that it guarantees the continuity of the structural loop. Also, by inserting the CFRP core into the structural shape, there is an increase in the bending collapse strength and stiffness. Moreover, no welding is required, only adhesives to join together each part. However, this proposal requires large quantities of CFRP and a mold to manufacture the reinforcement. This translates into higher material and manufacturing costs. Additionally, only new structures may benefit from this reinforcement, since existing structures would require extensive modifications in order to include them.

3.3.3 Reinforcement proposal 3

The third proposal consists of covering the structural node with a shell made from CFRP. The shell guarantees the continuity of the structural loop as long as good adhesion is guaranteed. To simplify installation, it can be built in two parts.

Similar to the previous proposal, the continuity of the structural loop is also guaranteed. The extra layer of CFRP also increases the crashworthiness, as the overall thickness of the shape grows. This proposal also has the advantage that it can be installed quickly on new and existing structures. Despite its advantages, the most significant drawback of this proposal is the need of a mold to generate each shell. Different tube sizes would also require different molds, which increases the cost.

3.3.4 Reinforcement proposal 4

The last reinforcement proposal covers only a pair of surfaces of the collapse zone with CFRP strips joined using a structural adhesive, as seen in Fig. 3.14. The reinforcements can cover either the webs or the flanges of the steel shape. By adding these localized reinforcements, focused on the collapse zone, the strength and energy absorbed by the collapse hinge can be vastly increased, without significantly adding up weight and manufacturing costs.

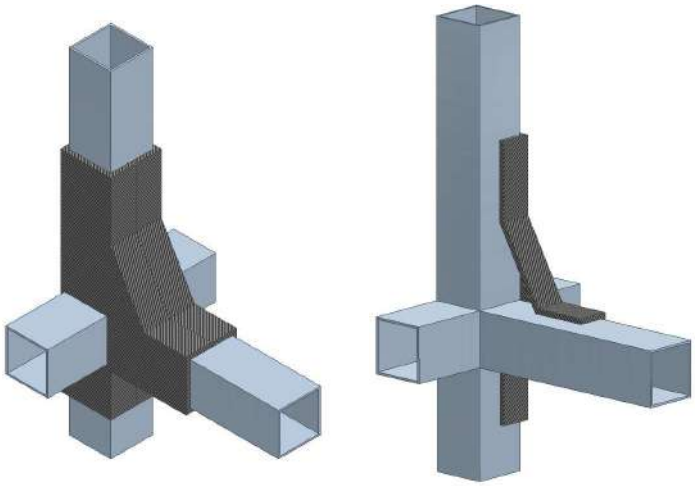

Figure 3.13: Reinforcement proposal 3. Left: reinforcemente assembled on the node. Right: section of the reinforcement.

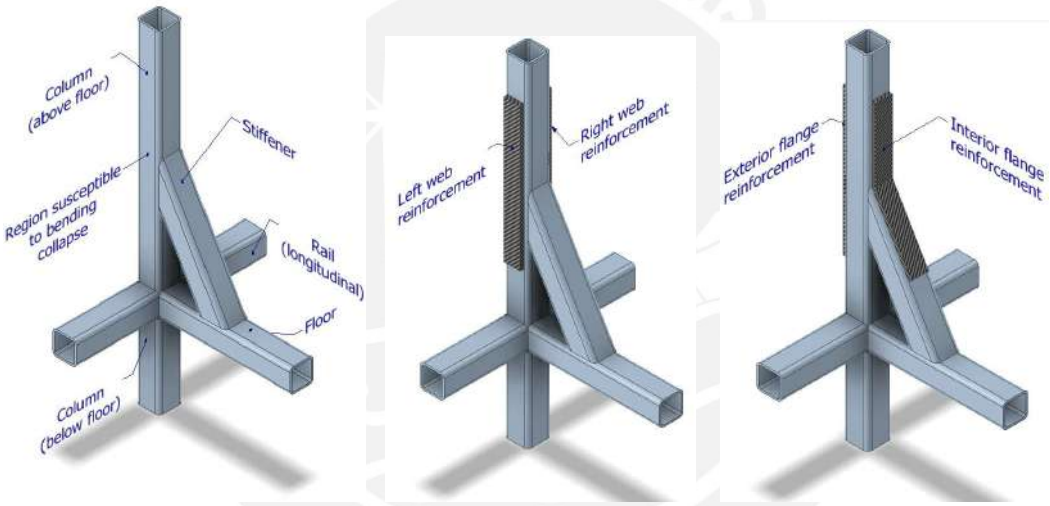

a) b) c)

Figure 3.14: Reinforcement proposal 4 (both variants). a) Original structural node from a bus structure, b) node with the webs reinforced, c) node with the flanges reinforced. This assembly can be replicated in several lightweight structures.

In this final proposal, the continuity of the structural loop is always guaranteed with the stiffener, while the CFRP strips add strength and crashworthiness with a minimal increase in weight. The main advantage is that the manufacturing is the simplest and least expensive, since only rectangular strips are required. Moreover, since the whole tube is not reinforced, there is space free for welding and further assembly.

3.4 Preliminary observations

From all reinforcement proposals, the fourth one seems to be the most adequate for new and existing super-structures. The main reason for this choice is the fact that they do not require complex or time-consuming manufacturing procedures and already provide a significant increase in the strength and absorbed energy (further details in Chapter 5).

There are two phenomenons that need to be taken into consideration for the following analysis:

- The main failure mechanism is bending collapse, as evidenced in Figs. 3.7 and 3.9 and it concentrates almost all plastic deformations. This means that a concept model of the super-structure with the collapse zones characterized by their response curves is a viable alternative for calculation. However, there is an evident difference between the Kecman collapse model (shown in the previous chapter) and the collapse hinges shown in Fig. 3.9, as in the latter the plastic hinge lines are not clearly defined. This discrepancy is further explained and solved in Chapter 4.
- The reinforcement can only work if there is an adequate load transfer between the steel and the CFRP. For the fourth proposal, mode II is the most likely failure mechanism for the adhesive, since the shear stresses are responsible for the load transfer. The structural adhesive used must be able to withstand the maximum shear loads during testing, more about this is explained in Chapter 5.

Chapter 4

Bending collapse analysis for thin and medium-thin-walled square and rectangular hollow shapes

This chapter consists of the publication: Lavayen-Farfan et al. (2021).
Thin-walled hollow shapes are of great interest in many industries with weight constraints due to their availability, low price, and strength to weight ratio. However, they are also prone to localized bending collapse, which can be used as an energy absorption mechanism during deformation. Up until now, industrial applications have relied on numerical simulations, non-standardized tests, and a handful of theories to address the bending collapse behavior. In this paper, a modification to the most widely used theory is presented and adapted for hollow shapes with greater thickness that cannot be considered "thick". To verify the accuracy of the proposed modification, a comparison with a detailed FEM model, validated through various three-point bending collapse experimental tests, has been performed. The results seem to show that the proposed modifications can predict the maximum load and collapse stage behavior of hollow shapes with more accuracy than the original analytical model. Thus, the proposed modification may be used to predict the collapse behavior of commercially available square and rectangular hollow shapes in different fields of application.

4.1 Introducción

One of the design rules of lightweight design consists of using the full load capacity of the material (H. E. Friedrich, 2017; Klein, 2013). This means that unlike classical mechanical design where only the elastic region is taken into consideration for calculations, lightweight design also considers the plastic deformation regions of the material to take it to its maximum load capacity. This is particularly useful in the automotive and aerospace industries, where structures have to be light and, at the same time, able to withstand high loads and to absorb the kinetic energy from impacts and collisions. The absorption of energy is typically performed by plastic deformations. For instance, the superstructure of a bus or coach must be able to absorb the kinetic energy from an impact and dissipate it as plastic deformations in certain parts of the structure. However, if this deformation is too large, then the deformed structure may crush the passengers, resulting in severe injury or death. Therefore, a correct and accurate calculation of the plastic and even collapse behavior of the structures and materials is needed, especially in the early stages of design.

When working with light structures, thin-walled, hollow shapes are preferred since they provide acceptable resistance and stiffness with low weight. Steel square hollow shapes (SHS) and rectangular hollow shapes (RHS) are extensively used in numerous manu-

facturing industries with weight constrains and high load requirements because of their availability, relatively low price, and different sizes. The problem with these structural shapes is that, due to their thin walls, they are prone to localized plastic collapse when a large bending moment is applied. It has been found, however, that localized collapse is a major energy absorption mechanism in these structures. The main difficulty with studying this failure mechanism is that "classical" theories cannot describe it, since it happens at a specific zone of the structure. Numerical simulations and experimental tests are an option and have been proven to offer accurate results, but they are often time-intensive and/or expensive, thus inadequate in the early stages of design. There has also been a handful of theoretical analyses devoted to bending collapse.

The earliest works by Kecman (1979, 1983), in the 1980s, have set the basis of study of bending collapse and were performed in order to assess the energy absorption of thin-walled RHS used in structures for buses. Also during those years, Wierzbicki and Abramowicz (1983) and Wierzbicki et al. (1994a, 1994b) performed a more detailed study on axial and bending collapse of hollow shapes and found certain similarities between both. Later works by T. H. Kim and Reid (2001), Shin et al. (2002), Y. Liu and Day (2008), H. C. Kim et al. (2013) as well more recent ones by Huang and Zhang (2018) and Huang, Zhang, and Fu (2020), offered different analytical approaches to the bending collapse of thin-walled shapes, all based on Kecman's work, addressing its limitations, offering corrections, and even expanding to include composite reinforcements. The bending collapse phenomenon has been validated through extensive experimentation and numerical simulations. However, even after addressing its limitations, Kecman's original model is still used by many researchers and engineers to study the bending collapse of thin-walled closed shapes. The main way to address the collapse behavior is through a bending moment–angle ($M-\theta$) curve for the plastic hinge that forms in the component under bending load, as well as the maximum moment reached and area under the curve, which consists of the energy absorbed through plastic deformation.

Experimental setups to determine the collapse behavior through the $M-\theta$ curves have also changed during the years. The earliest test rigs consisted of a cantilever beam setup. In this configuration, the free end of the cantilever is loaded through a system of cables and pulleys. The fixed end is either clamped to larger I-shapes fixed to the ground or casted into a concrete block. These testing rigs have been used by Kecman (1979) and Brown and Tidbury (1983). However, later research works have moved to a simpler setup consisting of a three-point bending test of the corresponding hollow shape. Authors such as Lee, Kim, et al. (2006) and Lee, Kim, et al. (2006), Y. Liu and Day (2008), Ruiz et al. (2009), Eksi and Genel (2013), Kadir et al. (2013),Phadatare and Hujare (2017), Q. Liu et al. (2017), Huang and Zhang (2018, 2020), Huang, Zhang, and Fu (2020), and Huang, Zhang, and Yang (2020), you Xie (2020), among others have used the three-point bending test. The advantage of using a three-point bending setup is that it can be easily installed on almost any universal testing machine; unlike the cantilever test setup, which requires additional preparations for the fixed support and load application. Moreover, Kecman's theory, despite having been tested and corroborated with a cantilever test, has also been used to compare results with three-point bending test results.

Currently, the only instance, with cantilever-like setups, is to assess the energy absorption in structural nodes of buses, according to the UN/ECE 66 (2007) for the rollover test of bus structures. Although this method is more frequently used in the industry and testing institutions, there has been research based on these test setups, such as Hashemi et al. (2009), Liang and Le (2009, 2010a, 2010b), Rincón-Dávila et al. (2019), all related to bus structures. Both test methods (cantilever bending and three-point bending) generally seem to produce similar results under certain circumstances.

It is also worth noting that a formal definition of how thin are thin-walled shapes has

yet to be found. The most important factor is not the thickness itself but thickness-to-height ratio (t/b). Most of the aforementioned authors, who focus on collapse theories for thin-walled hollow shapes, typically analyze hollow shapes with a thickness-to-height ratio lower than 0.03. However, not much research has been found that focuses on ratios $0.03 < t/b < 0.1$, which are typically commercially available and can still be considered thin and used by numerous manufacturers.

4.2 Theoretical analysis

4.2.1 Basic collapse theory

The original theory by Kecman (1979) (described in Chapter 2) has been proven to give a fairly good approximation for the collapse response of SHS and RHS. However, three major limitations have been encountered when applying it to medium-thin-walled shapes, defined by the authors as those with thickness-to-height ratios in the range of $0.03 < t/b < 0.1$, which are used by many manufacturers and cannot be defined as thick-walled. The first encountered limitation seemingly comes from the fact that Kecman's theory considers that all points in the through-the-thickness direction go into yielding at the same time, which is not the case for the medium-thin-walled shapes. Most of the surveyed literature focuses on ratios of t/b in the range of $t/b < 0.03$, where this assumption is fairly acceptable. Furthermore, the second limitation is related to the material model used. Most of the surveyed research has been performed with materials that can be represented fairly well with a elastic-perfectly plastic behavior. Even when this is not an explicit assumption of Kecman's model, the fact that certain terms of the energy absorbed by the hinge lines are expressed in terms of a constant flow stress, regardless of the deformation, shows that it is in fact an "implicit" assumption. Since material models with plastic hardening are not fully contemplated, some modification in the original model is required. This is especially important, since the maximum moment may be significantly underestimated for thicker shapes. Finally, the third and last limitation encountered is related to the fact that Kecman's model only considers the $M - \theta$ after the maximum moment is reached, in other words, it only considers the collapse stage. The energy absorbed before reaching this point is assumed to be negligible as it corresponds to elastic deformations with a minuscule rotation angle θ_m, where the maximum moment M_m occurs. In other words, θ_m is set to zero and only plastic angles are plotted. This approximation may be adequate for thin-walled shapes, however, it no longer applies when the thickness increases, as shown in Fig. 4.1.

All the aforementioned limitations are evident when comparing the resulting $M - \theta$ curves of shapes with different thicknesses (see Fig. 4.1). When a medium-thin-walled, rectangular or square hollow shape is used, the maximum moment is significantly increased (which is expected since the second moment of inertia is also increased); however, a not-so-evident consequence is that θ_m, corresponding to M_m, is no longer negligible. This fact indicates that the collapse does not occur immediately after the elastic portion (which is an assumption for very thin shapes). This phenomenon was also observed by Huang and Zhang (2018) and is explained as the failure mode switches from pure bending collapse to collapse with indentation, or even pure indentation (depending on the length of the shape). An alternate explanation is proposed for medium-thin-walled shapes: since the yielding does not occur at all points in the through-the-thickness direction at the same time, there is a significant portion of the $M-\theta$ curve with simultaneous elastic and plastic deformations. Thus, the maximum moment is not reached immediately after the load reaches the elastic limit value, instead it happens after most of the points have suffered yielding. The most notable consequence of it being that the energy absorbed before reaching the maximum moment is no longer negligible.

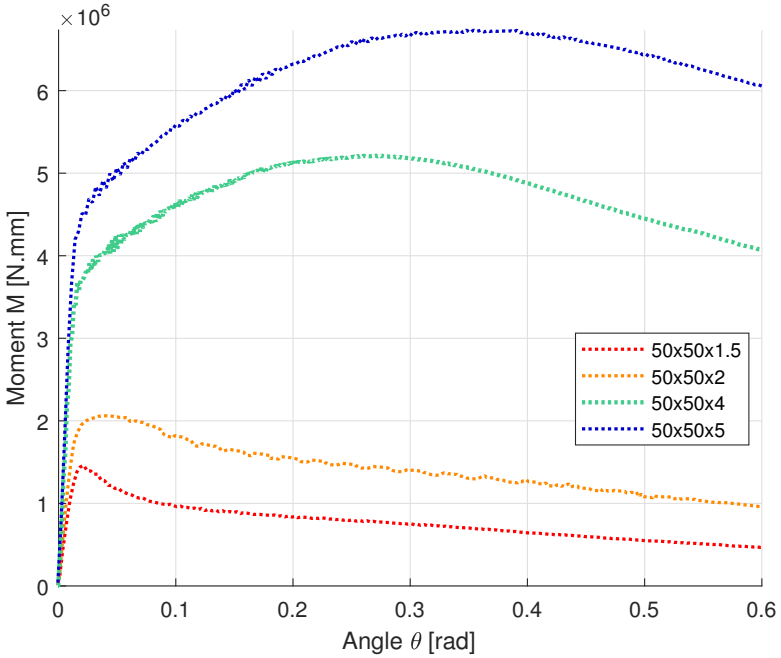

Figure 4.1: Moment- angle $M-\theta$ curve for different SHS 50x50 with various thicknesses. Results obtained with numerical simulations of a three-point bending test and steel S275.

4.2.2 Proposed modifications to the collapse theory

To address the limitations in Kecman's theory for medium-thin-walled shapes, certain modifications are proposed in this section. Kecman's model has already been modified in the past. The first modifications consist of correcting some kinematic incompatibilities, however, these corrections provide little improvements to the results accuracy as shown by T. H. Kim and Reid (2001). Other modifications consist of changing some terms of the collapse theory, to include the influence of additional materials, specifically changing the term m_p to a more general m_0, as well as the Eq. 2.4 to 2.12 (Shin et al., 2002). Other modifications have been made to include the elastic and elastic-plastic regions of the $M-\theta$ curve (Huang & Zhang, 2018). However, it was found that some of these approximations seem to work only for certain materials, since they were constructed by fitting experimental results of only one material (e.g. aluminum). In general, a modification to the theory should include all stages of deformation, namely: elastic, elastic-plastic, and collapse (Fig. 4.2), since θ_m cannot always be approximated to zero. These stages are shown in Fig. 4.3. These modifications should be able to address most of the aforementioned limitations, evident experimentally in the fact that with larger ratios of t/b, the hinge lines are no longer well defined, as seen both in Figs. 4.2 and 4.4.

Elastic deformation stage

The initial stage considers only the effect of elastic deformation, up to the point where plastic deformation starts. The maximum elastic moment M_e and corresponding angular deformation θ_e can be estimated when the normal stress at the top (or bottom) flange of the shape reaches the yield strength. For a beam in the three-point bending test configuration, the following equations from technical mechanics, for a simply supported beam with a concentrated load in the middle, can be used:

$$M_e = 0.9\frac{\sigma_Y(ab^3-(a-2t)(b-2t)^3)}{6b} \tag{4.1}$$

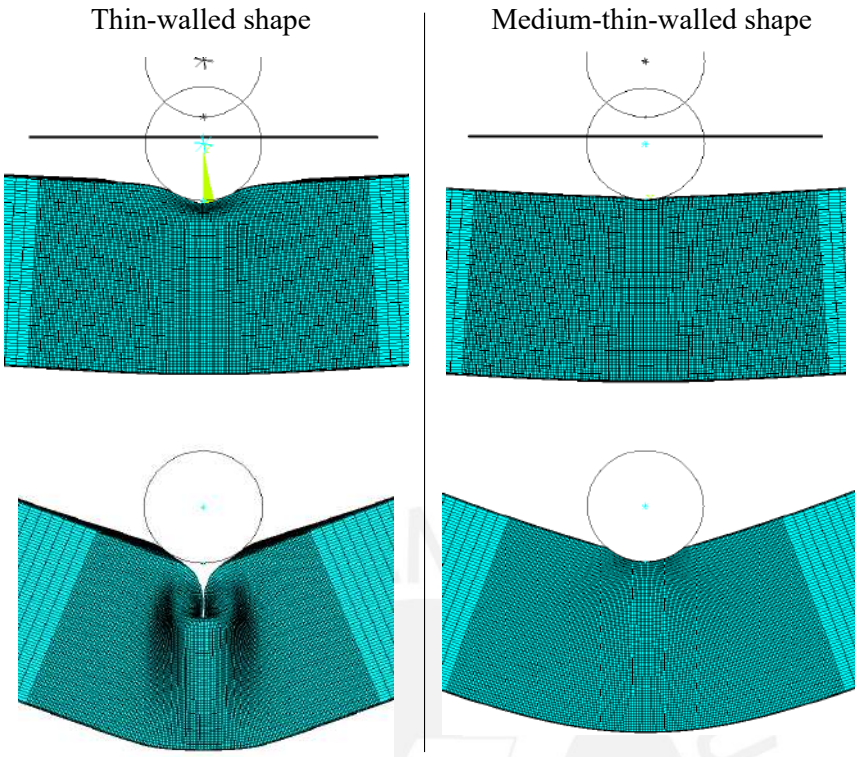

Figure 4.2: For thin-walled SHS (left) collapse begins with low displacement in the three-point bending test and closely follows Kecman's model; for thicker medium-thin-walled SHS (right), the collapse requires a larger displacement from the force applicator and includes some indentation and subsequently a larger θ_m. Thus, θ_m cannot be neglected with thicker shapes.

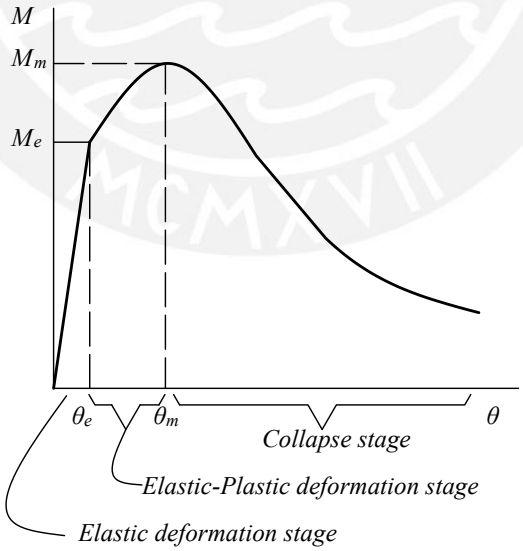

Figure 4.3: General shape of a $M - \theta$ curve, showing three main stages.

$$\theta_e = \frac{3M_e l_s}{Eb^2t(b+3a)} \tag{4.2}$$

where σ_Y is the yield strength of the material; E is the elasticity modulus; b, a and t are the height, width and thickness of the hollow shape, respectively; and l_s is the span in between supports of the three-point bending test, as shown in Fig. 4.5.

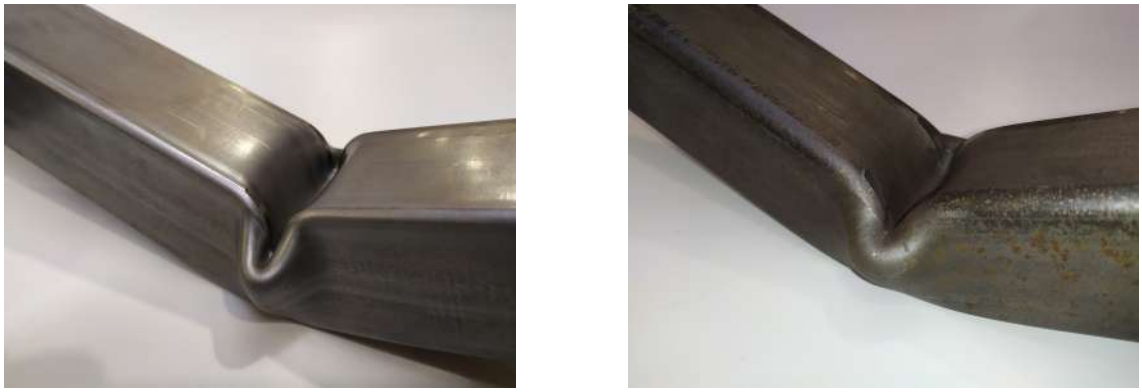

Figure 4.4: Comparison between collapsed test specimens with $t/b = 0.04$ (left) and $t/b = 0.08$ (right). Notice that the thicker specimen (right) does not show well defined hinge lines, thus a correction is needed.

The elastic deformation zone is then defined as a line between the origin and the elastic limit point (θ_e, M_e). Notice that depending on the thickness of the shape, this expression may sometimes slightly overestimate the value of M_e, thus the value of 0.9 is introduced to compensate. This seemingly occurs merely because the force applicator tends to initially crush the cross sections directly under it.

Elastic-plastic deformation stage

During the elastic-plastic deformation stage, there are two phenomena occurring simultaneously: there are cross sections with both elastic and plastic deformations, and the zones with plastic strains also endure hardening. This stage typically occurs quickly in thin-walled shapes, but it is significant in medium-thin-walled shapes, as shown in the comparison in Fig. 4.2. This region can be approximated by a parabola, that passes through the points (θ_e, M_e) and (θ_m, M_m). However, this information is not enough to fully define the parabola. The maximum moment M_m, defined later in the collapse stage, cannot be surpassed, which means that the point (θ_m, M_m) can work as a vertex of the parabola. Since there is no analytical expression for the angle θ_m, it is proposed that its value is obtained by fitting the results from the numerical simulations. The procedure is further detailed in the following section.

Collapse stage and modifications

A comparison for the collapse stage in thin-walled and medium-thin-walled shapes is shown in Fig. 4.2. The first modification to the original theory was described by Kecman himself. The numerical derivation mentioned in Eq. 2.13 typically results in extremely high bending moments for very low angles (typically 10 to 20 times than the actual maximum bending moment). Kecman initially attempted to overcome this limitation, by calculating M_m and connecting the point $(0, M_m)$ (neglecting θ_m) to the curve $M - \theta$ with a tangent line. Since this procedure is empirical, later authors usually intersect the $M - \theta$ with an horizontal line that passes through M_m, and thus obtaining θ_m. In this research, it is observed that the initial correction by Kecman can still be used for "medium-thin-walled" SHS and RHS. However, the resulting M_m and θ_m are usually underestimated so further modifications are introduced.

All terms for the energy absorbed during collapse depend on Eq. 2.3; and in turn,

this equation is dependent on the flow stress σ_0. During the formation of the hinge lines, not all points reach the yield stress σ_Y and the flow stress σ_0 at the same time, thus the approximation $\sigma_0 = \sigma_B$, as well as the use of σ_Y are no longer adequate. Wierzbicki et al. (1994a, 1994b) estimated that the nominal flow stress is actually less than the ultimate strength σ_B; whereas T. H. Kim and Reid (2001) estimated that, depending on σ_{cr} (see Appendix, Eq. 2.14), the nominal flow stress can be estimated as the average of both σ_Y and σ_B. In this work, an effective yield strength σ_{Ye} and an effective flow stress σ_{0e} are defined based on a linear relationship between σ_Y and σ_B:

$$\sigma_{Ye} = a_e \cdot \sigma_Y + (1 - a_e) \cdot \sigma_B \tag{4.3}$$

$$\sigma_{0e} = c_e \cdot \sigma_Y + (1 - c_e) \cdot \sigma_B \tag{4.4}$$

where $0 \leq a_e \leq 1$ and $0 \leq c_e \leq 1$. These factors are in turn dependent on the thickness-to-height ratio t/b for SHS, as well as the height-to-width ratio b/a for RHS. For this work, the reference $M - \theta$ curves are obtained from numerical simulations of the three-point bending test (described in the following section), and each factor is determined from said results as follows:

- a_e: This factor determines the effective yield strength, and is directly responsible for the maximum moment M_m. Thus, only the M_m is used to determine a_e for different t/b proportions for SHS (and b/a for RHS). M_m is obtained through numerical simulations, and the relationship of a_e and t/b and b/a can be fitted from the simulation results for different ratios (see Fig. 4.11 and 4.12 in the results section).

- c_e: This factor describes the behavior after the maximum moment is reached, as the Eq. 2.3 (which is needed for Eqs. 2.4 to 2.11) requires the effective flow stress. This value is determined by minimizing the difference between the energy absorbed after collapse from numerical simulations and the energy absorbed after collapse using the proposed model. Both absorbed energy values are obtained using the area under each curve after M_m is reached.

- θ_m, i.e. the angle where M_m occurs, is obtained with numerical simulations for various values of t/b and b/a. This value is used to "offset" the collapse stage obtained by the original model. The relationship between θ_m and t/b can also be fitted from the numerical results (see Figs. 4.13 and 4.14 in the results section).

These factors are calculated and obtained for various calibration sizes of SHS and RHS corresponding to different ratios. These calibration sizes are displayed in Tables 4.2 and 4.3. Next, the obtained factors a_e, c_e and θ_m are tested and verified by predicting the complete behavior in SHS and RHS for sizes not used in the calibration. The sizes used to verify the accuracy of the proposed modification are displayed in Tables 4.4 and 4.5. Using the factors a_e, c_e and θ_m, the following procedure is proposed to obtain the bending collapse behavior:

1. Determine the maximum collapse moment M_m (see appendix), which depends on factor a_e, which in turn depends on the ratio t/b (and b/a for RHS). Depending on the case, a_e can be determined with a curve fit (SHS) or a surface fit (RHS), both are shown in the next section.

2. Calculate modified Kecman curve, based on factor c_e, and define a tangent line that crosses the point $(0, M_m)$. This corresponds to the original Kecman modification. Depending on the case, c_e can be determined with a curve fit (SHS) or a surface fit (RHS), both are shown in the next section.

3. Offset the resulting curve horizontally, until the top of the curve reaches the point (θ_m, M_m). By offsetting the curve, the elastic and elastic-plastic stages can be included. Depending on the case, θ_m can be determined with a curve fit (SHS) or a surface fit (RHS), both are shown in the next section.

4. Connect the origin with point (θ_e, M_e) with a line, which describes the elastic stage.

5. Connect the point (θ_e, M_e) with point (θ_m, M_m) with a parabola, with vertex at (θ_m, M_m). This parabola describes the elastic-plastic stage.

It should be noted that even though we propose that the values of a_e, c_e and θ_m should be obtained by numerical simulations (validated through experimental tests), they could also be determined using experimental tests if different shape sizes are available.

4.3 Procedure

4.3.1 Experimental test setup

As mentioned above, there are two alternatives to obtain a bending collapse (either with experiments or simulations): a cantilever test and a three-point bending test; the latter being the most commonly used in recent literature and simpler to reproduce. In this work, a three-point bending test is performed of different hollow shapes, with different values of ratios t/b, but maintaining a ratio of $l_s/b = 10$ to ensure bending collapse with minimum indentation. The scheme in Fig 4.5 is used as the base for the experimental setup, seen in Fig. 4.6. The tested sizes are shown in Table 4.1. Since the hollow shapes are manufactured by welding, the weld is always kept in the bottom part (in contact with the supports), so that it is subjected to traction along the weld, thus limiting its possible influence on the collapse behavior.

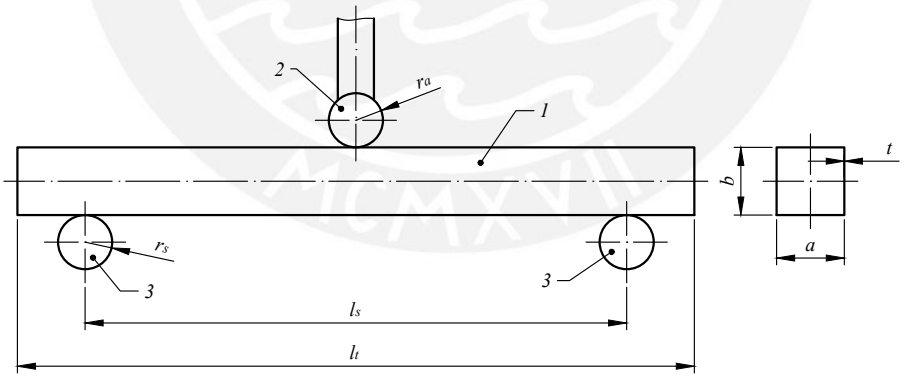

Figure 4.5: Three-point bending test scheme. 1: test specimen (RHS or SHS), 2: force applicator, 3: supports

For all tests, the force applicator consists of a cylinder with 30 mm diameter, connected to a force sensor capable of measuring up to 200 kN. Two pairs of support cylinders have been used. The first pair consist on the supports shown in Fig. 4.6, which also have a diameter of 30 mm. However, for the tests of the specimens SHS50x50x2 and SHS50x50x4, a pair of supports with 48 mm of diameter are used, which have a stronger base. The reason for the switch is the fact that the larger shapes required a larger l_s to obtain bending collapse, and the lateral force that the supports must endure is larger than the maximum lateral force that the first pair of supports could withstand. All tests are performed with a velocity of 1 mm/s.

Figure 4.6: Experimental setup for the three-point test scheme.

Table 4.1: Dimensions of tested specimens.

Nomenclature	height b (mm)	width a (mm)	thickness t (mm)	ratio t/b (-)	Span l_s (mm)
SHS25x25x1.5	25	25	1.5	0.06	250
SHS25x25x2	25	25	2	0.08	250
RHS30x80x1.5	30	80	1.5	0.05	300
SHS50x50x2	50	50	2	0.04	475
SHS50x50x4	50	50	4	0.08	475

Material properties are extracted from coupons obtained from the sides of the hollow shapes. For each shape size, two coupons are obtained. The geometry of the test coupons is defined according to standard ASTM A370. The resulting engineering stress and strain curves are shown in Fig. 4.7.

It is worth noting that one of the resulting stress and strain curves shows an elastic-perfectly plastic behavior, however, the other coupons do exhibit plastic hardening. Even when all shapes are sold as S275, they do not have the same actual values for yield and ultimate strengths although they satisfy the minimum requirements to be classified as such. This is most likely due to the manufacturing process for each shape. It should be noted, that the forming process of hollow shapes requires plastic deformations of the base material, which increases both the yield and ultimate strengths.

4.3.2 Numerical simulation setup

The scheme in Fig. 4.5 is used as a base to build the numerical model, seen in Fig. 4.8. The FEM model is built in Ansys Classic (APDL) 2019R1, with the dimensions and material properties as input parameters, which are changed for the different sizes and material properties. The parameters are defined in Matlab, where a script modifies the APDL input files. Once modified, they are sent to Ansys via the toolbox Ansys AAS (Ansys as a server) (ANSYS Inc., 2021a). The results of each simulation are then

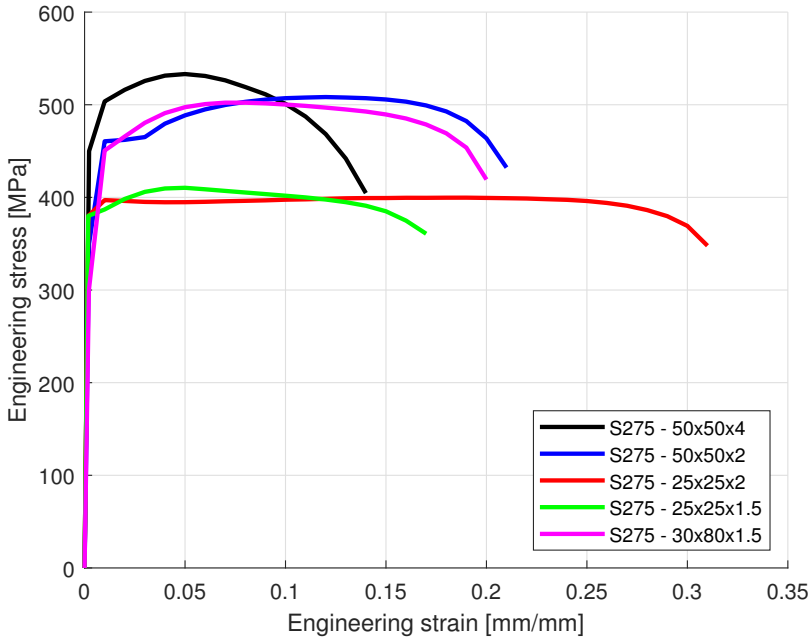

Figure 4.7: Engineering stress-strain curves from the coupons extracted from the test specimens. Averaged results. All samples are rated as S275.

exported and can be read in Matlab for further post-processing. The FEM model consists of 8-node brick elements with 3 elements in the through-the-thickness direction of the shapes. Furthermore, the mesh is refined near the contact zone of the force applicator, with elements of 1 mm of length in the longitudinal direction. The top and bottom faces near the force applicator and supports are covered with penalty-based contact elements. The force applicator and the supports are modeled using one target element each, which is shaped as a hollow rigid cylinder with its movement constrained through a pilot node at its axis. This configuration offers adequately accurate results, with less elements and allows the boundary conditions to be set on pilot nodes at the center of the cylinders. The results do not differ significantly from previous simulations, where the supports and force applicator were meshed with a finer mesh and numerous elements in the cylinders (and longer simulation time). Since the focus of the research is on the collapse of the hollow shapes, the cylinders are modeled as rigid bodies. Pilot nodes are also added at both ends of the test specimen, to restrict the average movement out of the bending plane, without restricting each particular node to move in the out-of-plane direction. These constraints are added for stability and produce near-zero reaction forces. All models have up to 205000 nodes and up to 162000 elements. The supports are initially in contact with the SHS (or RHS), and the force applicator is initially located with an offset of 5 mm above the top face of the test specimen, so there is no initial contact. The model and its details can be seen in Fig. 4.8.

The model also includes fillets with radii that depend on the dimensions of the shape, according to standards EN 10219 and EN 10305. Authors such as X. Zhang, Zhang, and Ren (2016) have found that the presence fillets may have a significant influence in the maximum moment and later response. It has been theorized by the aforementioned author, that the fillets act as triggers for the collapse. In fact, the hollow shape standards EN 10219 and EN 10305 establish a range of acceptable fillet radii according to the size. Thus, fillets are included in the geometry for the FEM simulations. It is worth noting that their influence appears to be present only on the maximum moment, not in the collapse

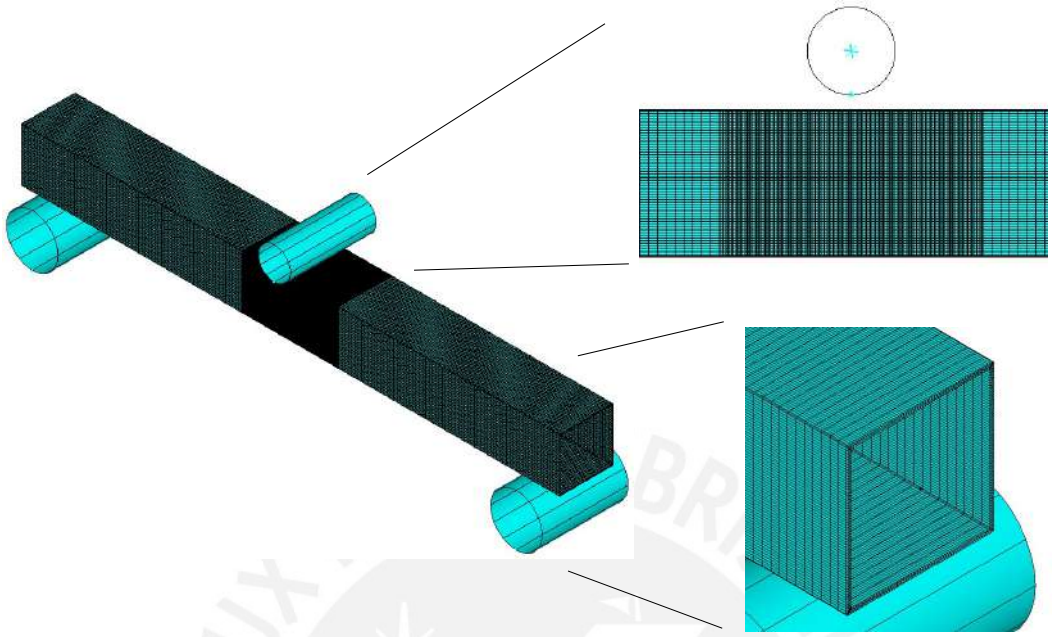

Figure 4.8: Numerical model for the bending collapse. Details of the numerical model: Top right: force applicator in the initial position and refinement of the mesh in the collapse portion. bottom right: Mapped meshing in the through-the-thickness direction.

stage itself, thus its influence is included in a_e. The theoretical model (seen in Fig. 2.10) does not take the fillets into account. It can be argued that since the arc length of the fillets is rather small when compared with the height or width of the shape, its influence on the collapse stage is negligible.

The velocity of load application is also important since the response and $M-\theta$ curves change for static and impact loads. Dynamic response can also be approximated from the static loading, by multiplying the static response curve by a factor K_d that depends on the material, in case of steel $K_d = 1.2$ (UN/ECE 66, 2007). Thus, only a quasi-static test scenario is performed. The selected force applicator velocity is set to 1 mm/s. The SHS and RHS are made of steel S275. A linear elastic model is used for the elastic portion of the stress-strain curve; since plastic deformations are expected, a piecewise plastic hardening rule is also used. The plastic hardening rule is based on the true-stress and true-strain curve obtained from Fig. 4.7 (for the validation of the numerical model) and from (Krolo et al., 2016) (for the calculation of different sizes).

The main outputs of the simulation are the imposed vertical displacement u_y and the reaction force on the pilot node of the force applicator f_y. These results cannot be used to make a direct comparison between the numerical simulations and the proposed analytical model; since the output of the latter is a $M-\theta$ curve instead of a $f_y - u_y$ curve. These results are also highly dependent on the length between supports l_s (seen in Fig. 4.5). In order to make a comparison between the two approaches, the internal bending moment

from the numerical simulation is determined using the section method (from technical mechanics) and assuming a quasi-static process, both for a simply supported beam (Eq. 4.5). On the other hand, the angle θ can be approximated by a geometric relationship (Eq. 4.6), assuming that the bending angle along the beam is negligible and the center portion of the beam acts as a hinge:

$$M = \frac{f_y l_s}{4} \tag{4.5}$$

$$\theta = 2 \arctan\left(\frac{2u_y}{l_s}\right) \tag{4.6}$$

4.3.3 Results and validation of the numerical simulation

Using the results from the three-point bending experiment, as well as the mechanical properties obtained from the coupons, the accuracy of the numerical model can be evaluated and the model validated. It is important to note that the material properties are not the same for every size, and the corresponding properties are taken from Fig. 4.7. The model includes characteristics such as fillets (average fillet radius) and can be used for materials with either perfectly plastic behavior or plastic hardening. The comparison of the results is performed by using the $M - \theta$ curves as shown in Fig. 4.9.

The numerical model seems to adequately reproduce the experimental results. Each experimental test was performed three times, except for the 50x50x2 shape. For this last one, the test was also performed with the longitudinal weld in the lateral and top positions. No significant difference or apparent influence of the weld on the collapse behavior or the maximum moment has been found.

4.3.4 Dimensions for the test specimens in the numerical simulations

Different dimensions are chosen to obtain $M-\theta$ curves and fit the results for the parameters a_e, c_e and θ_m. The results are analyzed in function of certain ratios for the SHS and RHS. The thickness-to-height ratio t/b is used to address the relative thickness of the test specimen, for both SHS and RHS. The height-to-width ratio b/a is also used to address the influence of the width of the test specimen. In order to better understand the meaning of the last factor, the following visual aid is provided in Fig. 4.10.

To guarantee a bending collapse failure instead of indentation, a minimum proportion of $l_s/b \geq 9$ is chosen (Huang & Zhang, 2018); simulations were also run to verify this value. The length $l = 500$ mm is selected to guarantee bending collapse for all tested specimens, which corresponds to $l_s = 450$ mm, giving 50 mm to both extremes. This means that a maximum height b of 50 mm is used. Different thicknesses for various heights are then chosen to obtain t/b ratios in the range of $0.03 \leq t/b \leq 0.1$, which correspond to the medium-thin-walled shapes, the focus of this study. These values are detailed in Table 4.2.

It is also worth noting, that the length between supports has a minor influence on θ_m, as long as bending collapse is guaranteed. Bending collapse occurs due to the influence of only the bending moment in the beam, thus the maximum moment should not be significantly affected by different lengths l_s. However, θ is determined through an approximation (recall Eq. 4.6) which depends on u_y; thus, larger values of l_s give larger u_y and, in turn, make θ grow. The authors did not find a significant difference in the maximum moment when l_s is increased, and only a slight increase in θ_m. It should be noted, however, that in case that a more compliant material was used (e.g. aluminum), a larger increase should be expected.

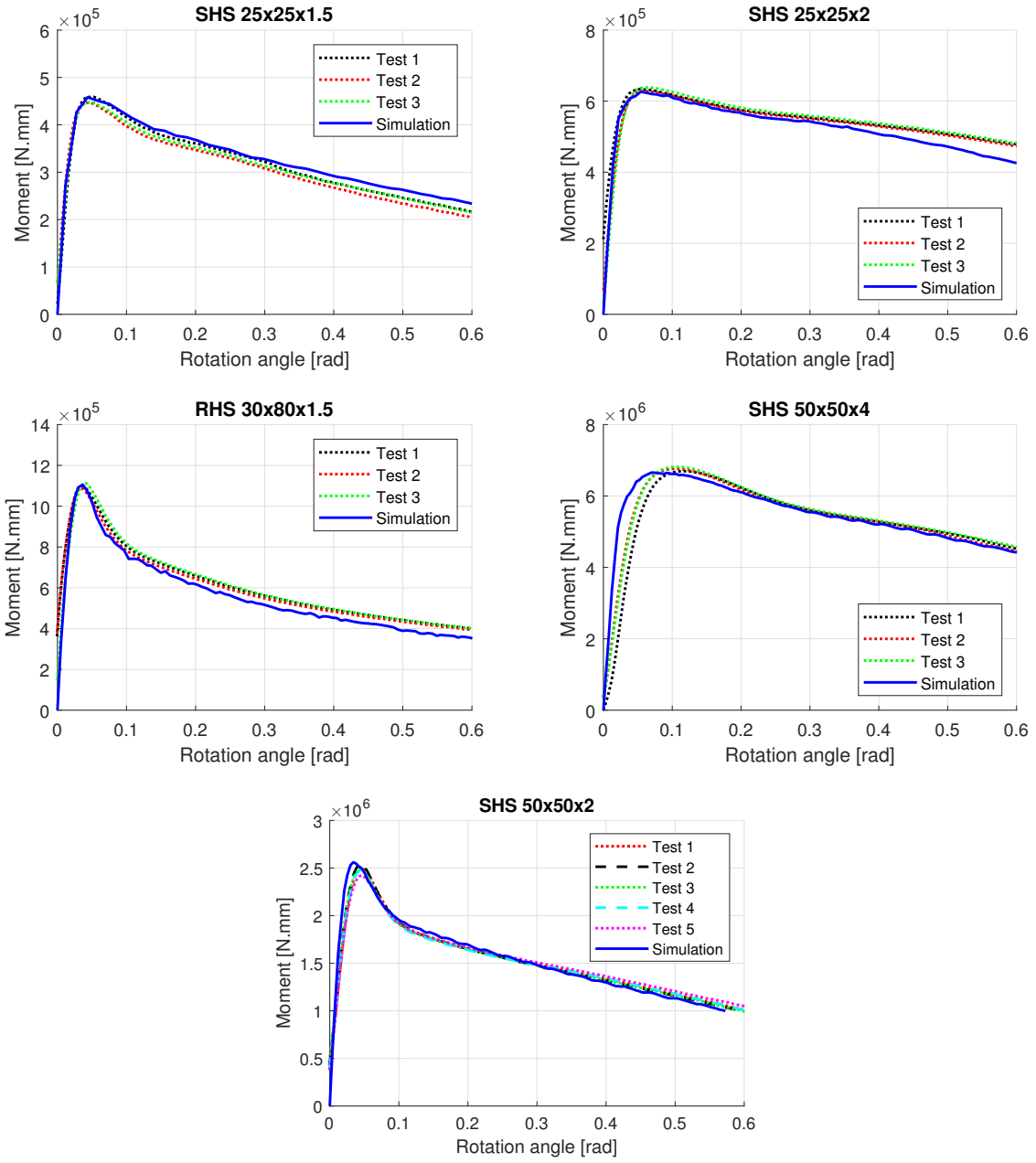

Figure 4.9: Comparison of the experimental results and numerical results with different shape sizes.

For the RHS, the standard EN 10305 and material S275 are also used. The chosen dimensions must satisfy the same conditions for the SHS: cover a range of values of t/b. Moreover, the influence of the ratio b/a also has to be analyzed. There are various combinations of t/b and b/a. In order to avoid analyzing each possible combination of ratios and having to deal with an excessive sample size and computational time, Latin-hypercube sampling is used to obtain a reduced sample size. However, even when there are numerous possible combinations (around 73 in the considered range), only around 8 different levels are identified based on the commercially available sizes. Introducing more levels is not feasible, since the resulting Latin hypercube levels must be rounded to the nearest available commercial size. This may result in repeating values, and defeating the purpose of the Latin-hypercube sampling. The selected sizes are shown in Table 4.3. Note that some

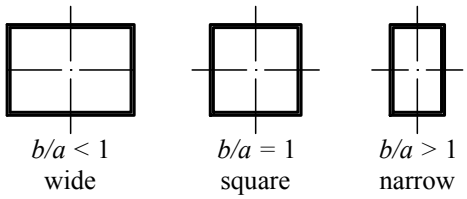

Figure 4.10: Visual aid showing wide and narrow rectangular hollow shapes.

Table 4.2: SHS dimensions for calibration- all taken from standard EN 10305.

SHS ($b \times b \times t$)	t/b	Thickness
25x25x1.5	0.06	medium-thin
25x25x2	0.08	medium-thin
30x30x2	0.067	medium-thin
40x40x1.5	0.038	medium-thin
40x40x2	0.05	medium-thin
50x50x1.5	0.03	thin
50x50x2	0.04	medium-thin
50x50x4	0.08	medium-thin
50x50x5	0.1	medium-thin

levels are inevitably repeated.

Table 4.3: RHS dimensions for calibration- all taken from standard EN 10305.

RHS ($b \times a \times t$)	t/b	b/a
45x45x1.5	0.033	1
50x80x2	0.04	0.625
50x30x2.5	0.05	1.667
35x70x2	0.057	0.5
40x60x2.5	0.0625	0.667
30x15x2	0.0667	2
40x60x3	0.075	0.667
40x27x3	0.075	1.48

The results obtained with the dimensions selected in Tables 4.2 and 4.3 are used to calibrate the modifications of the theoretical model, i.e. factors a_e, c_e and θ_m. Numerical simulations are also run on the dimensions of the commercially available shapes, shown in Tables 4.4 and 4.5, to compare the accuracy of the proposed modifications.

The material properties for the numerical simulations used for the different shapes have a great influence on the results. Even when they are made from the same steel, the manufacturing process has a large influence on the final yield and ultimate strengths as discussed before. To ensure a proper calculation tensile tests should be carried out first. However, performing them defeats the purpose of fast and accurate calculations of the maximum bending moment at the early stages of design. There is also the possibility that the properties change from different suppliers. Thus, the calculations of factors a_e, θ_m, and c_e are carried out using the nominal properties of steel S275, which are shown in Table 4.6.

Table 4.4: SHS dimensions for testing- all taken from standard EN 10305.

SHS ($b \times b \times t$)	t/b
30x30x1.5	0.05
35x35x2	0.057
40x40x3	0.075
45x45x2	0.044
45x45x3	0.067

Table 4.5: RHS dimensions for testing- all taken from standard EN 10305.

RHS ($b \times a \times t$)	t/b	b/a
30x50x2	0.067	0.6
40x20x2	0.05	2
40x60x4	0.1	0.667
40x27x1.5	0.038	1.481
50x30x2	0.04	1.667
50x70x2	0.04	0.714
50x100x4	0.08	0.5

4.4 Results and discussion

In this section, the results obtained with numerical simulations are used to approximate the relationship between the factors a_e, c_e, and θ_m for the various ratios t/b and b/a. The obtained fits are then tested with sizes not used in the calibration. Furthermore, the resulting $M - \theta$ curves obtained by the proposed model are compared to the numerical simulation to test its accuracy, and to Kecman's original theory to verify the improvement for medium-thin-walled shapes.

4.4.1 Parameters for the proposed modification of the collapse stage

Effective yield stress factor a_e

The resulting a_e curve for SHS shows a clear tendency downwards with increasing t/b, as shown in Fig. 4.11. This means that the effective yield strength increases with larger ratios of t/b (lower a_e translates into a higher σ_{Ye}). However, the relationship between a_e and t/b is not linear. A polynomial (3rd degree) fit is proposed, obtaining the following relationship:

$$a_e(t/b) = 1472(t/b)^3 - 192.9(t/b)^2 - 7.015(t/b) + 1.357 \tag{4.7}$$

The goodness of the fit is measured through R-square, resulting in 0.9934; and a SSE, resulting in 0.004387. The polynomial fit can be seen in Fig. 4.11.

It is worth noting that values of a_e larger than one, would mean that there is collapse before yielding, which may occur with very thin-walled shapes. Also, Kecman's models consider that $a_e = 1$ and gives good results for thin-walled shapes. Larger values of t/b mean that the profile is not that thin anymore, and the prediction of the maximum moment is not accurate without the factor a_e. For $t/b > 0.1$, a_e seems to converge at around 0.2 for SHS.

As for the RHS, the factor a_e tends to decrease with thicker shapes, which indicates that yielding in the through-the-thickness direction does not occur at all points at the

Table 4.6: Mechanical properties of S275, taken from Krolo et al., 2016.

Property	Value	Units
Young modulus	200	GPa
Poisson ratio	0.3	-
Minimum yield strength σ_Y	275	MPa
Ultimate strength σ_B	480	MPa

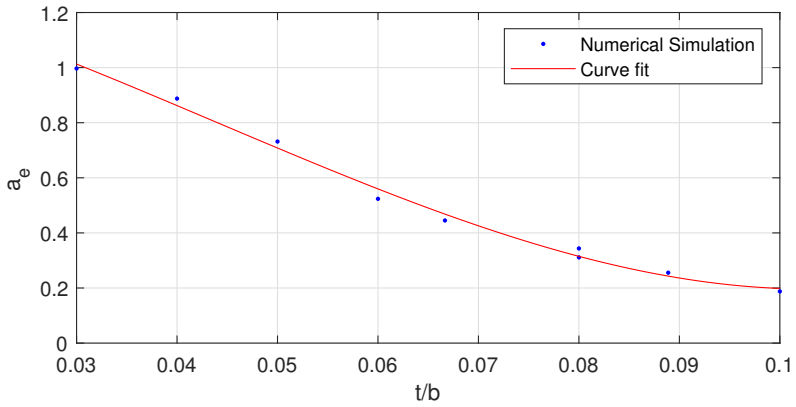

Figure 4.11: Relationship between a_e and t/b.

same time. Moreover, the ratio b/a also influences the behavior of a_e significantly. Lower values of b/a tend to increase a_e, meaning that "narrow" RHS tend to collapse later than "wider" RHS of the same height b. This behavior can be explained by the fact that, for a set height b, a larger a (ergo lower b/a) makes the hollow shape also relatively thin-walled in the direction perpendicular to the bending plane, making it more prone to collapse, with faster formation of hinge lines. The relationship between a_e vs t/b and b/a is shown in Fig. 4.12.

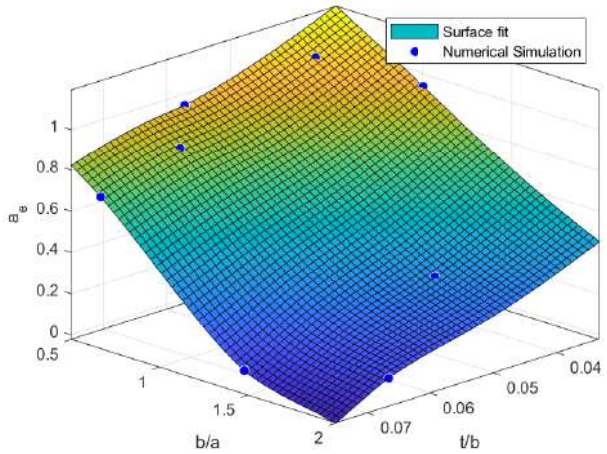

Figure 4.12: Surface of the relationship between a_e and ratios t/b and b/a obtained through a thin-plate spline interpolation.

Angle θ_m at which M_m occurs

Similarly, the angle θ_m can also be related to the ratio t/b as shown in Fig. 4.13. It is found that for low values of t/b or very thin-walled shapes, this angle is almost zero. This fact agrees with the works by previous authors, such as Kecman Kecman, 1983 and Kim T. H. Kim and Reid, 2001, who consider that this angle is negligible. However, when the thickness increases, the angle θ_m grows as well and tends to reach the value of around 0.35 radians. Due to the shape of the simulation points, a sigmoid fit is proposed as follows:

$$\theta_m(t/b) = \frac{0.3484}{1 + \exp\left(-\dfrac{t/b - 0.05972}{0.009577}\right)} \tag{4.8}$$

The sigmoid-like fit achieves an R-square of 0.9763 and a SSE of 0.003257.

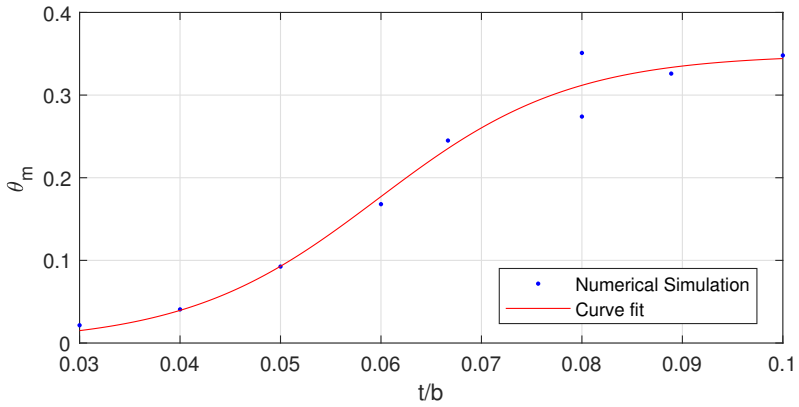

Figure 4.13: Relationship between θ_m and t/b.

The behavior of the angle θ_m is explored for the RHS cases as well, and a similar behavior of the one shown in Fig. 4.13 is found. It is observed once again that thicker shapes tend to increase θ_m significantly. However, this increase depends also on the ratio b/a as narrow beams tend to increase θ_m even more, as shown in Fig. 4.14. This behavior can also be explained. For larger a lengths, or wider RHS, the shape becomes thinner in the horizontal direction (perpendicular to the bending plane) and, similarly to a_e in Fig. 4.12, the shape becomes more susceptible collapse, as hinge lines form rapidly with ease.

Effective flow stress factor c_e

In contrast to a_e, c_e and t/b do not seem to have a clear relationship. However, many simulations show that $0 \leq c_e \leq 0.5$ (Fig. 4.15), meaning that the effective flow stress lies between $0.5(\sigma_Y + \sigma_B)$ and σ_B, which seems to agree with previous authors such as T. H. Kim and Reid (2001), and Abramowicz and Jones (1997). There are some points with very high values of c_e, meaning that there is a low value of σ_{0e}. This behavior can be explained by showing a second relationship, between c_e, t/b and b/l_s (see Fig. 4.16). It can be seen that the three apparent outliers with c_e near 1 are also those with a high ratio b/l_s, which translates into shorter test specimen and in turn some indentation. When using short specimens $b/l_s > 0.125$ (or $l_s/b < 8$) there is a significant amount of indentation in the test specimen (Huang & Zhang, 2018).

When including the ratio b/a in the comparison (for RHS), more insight into the factor c_e can be extracted, as shown in Fig. 4.17. In general, thin and wide shapes tend to have a slightly higher value of c_e, however, this value lies in the 0.4 to 0.6 range. This result,

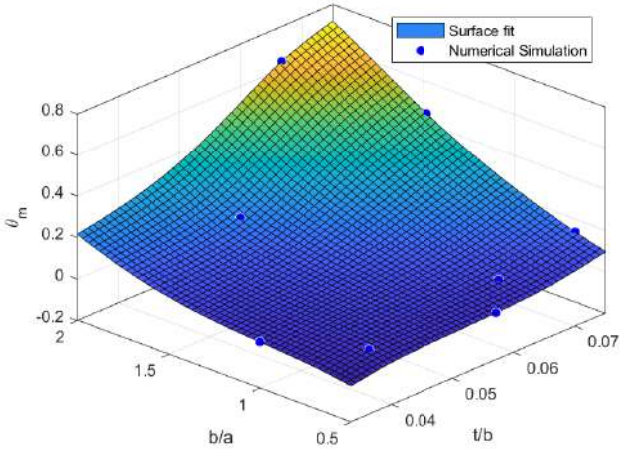

Figure 4.14: Surface of the relationship between θ_m and ratios t/b and b/a obtained through a thin-plate spline interpolation.

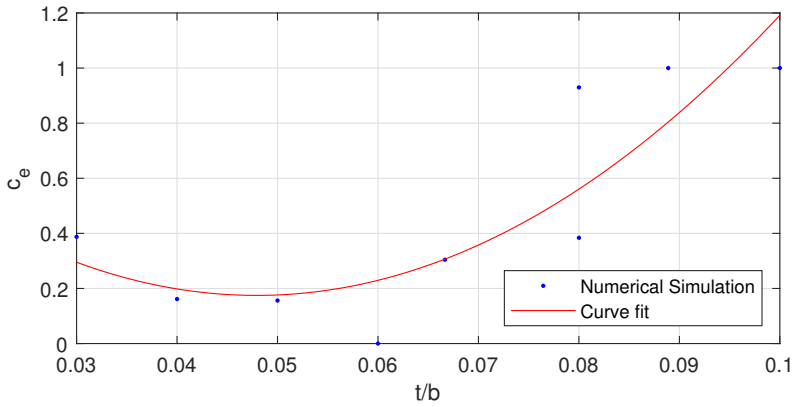

Figure 4.15: Relationship between c_e and t/b.

as the one for SHS, agrees with the assumptions by previous authors who make fixed approximations for the nominal flow stress. For narrow and thicker shapes, c_e tends to be also slightly larger, meaning that the flow stress is actually lowered. An explanation for this behavior is proposed as the cross section under the force applicator tends to be crushed, and the failure mode is actually collapse and indentation (recall Fig. 4.2). This means that points near the cross section actually require less load to reach the flow stress, since they are already deformed due to the indentation.

4.4.2 Verification of the parameters with test sizes

All parameters a_e, c_e and θ_m are calculated using the curve and surface fits shown above and used to obtain the corresponding $M-\theta$ curves, which are then compared to numerical simulations. The accuracy of the prediction of the original model is computed as well to determine which model is better at predicting the collapse behavior for thin and medium-thin-walled shapes. The accuracy is measured using an error percentage, with the numerical model results as reference, as indicated in Eq. 4.9 and 4.10.

$$Error = \frac{|M_{numerical} - M_{proposed}|}{M_{numerical}} \times 100\% \tag{4.9}$$

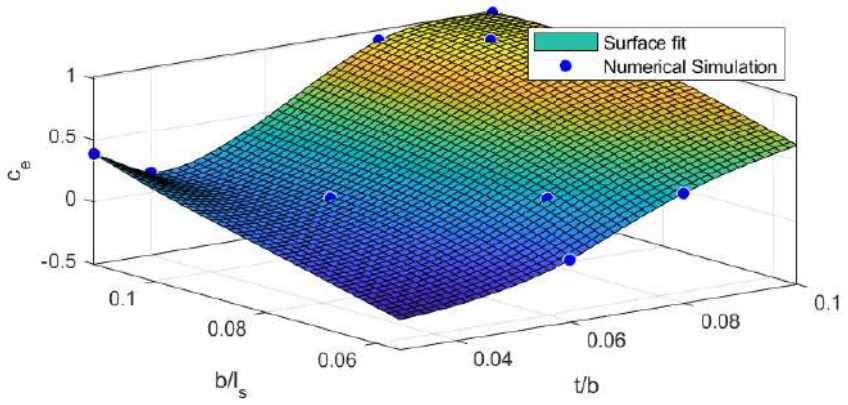

Figure 4.16: Relationship between c_e and t/b and b/l_s using a thin-plate spline interpolation.

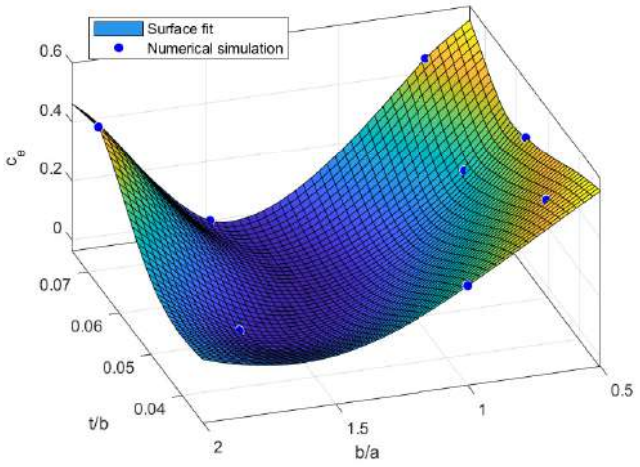

Figure 4.17: Surface of the relationship between c_e and ratios t/b and b/a obtained through a thin-plate spline interpolation.

$$Error = \frac{|M_{numerical} - M_{original}|}{M_{numerical}} \times 100\% \tag{4.10}$$

Square hollow shapes

The comparison $M - \theta$ curves for SHS using the approximations for a_e, c_e, and θ_m are shown in Fig. 4.18. The obtained curves show that for most cases the error for the proposed analytical model is kept at less than 5% most of the time, with few exceptions in points where the error grows as large as 10%. In contrast, the error for the Kecman original model can be as large as 20% and in some cases up to 30%; with both errors tending to decrease for large values of θ. In most cases, the largest error occurs at θ_m for the original model which shows a poor prediction for M_m. Factor a_e and θ_m seem to almost completely overcome this problem, for the proposed model. Factor c_e apparently reduces the error for $\theta > \theta_m$. There is also apparently an extremely large error for $\theta = 0$. This apparent large error occurs mainly because the original model does not predict the elastic behavior. For all SHS examined, the proposed model with modifications can estimate the numerical prediction with better accuracy than the original theory. This improvement is more noticeable with the relatively thicker shapes SHS40x40x3 and SHS45x45x3, which

confirms the capacity of the proposed model to predict the maximum moment and collapse behavior for "medium-thin-walled" shapes.

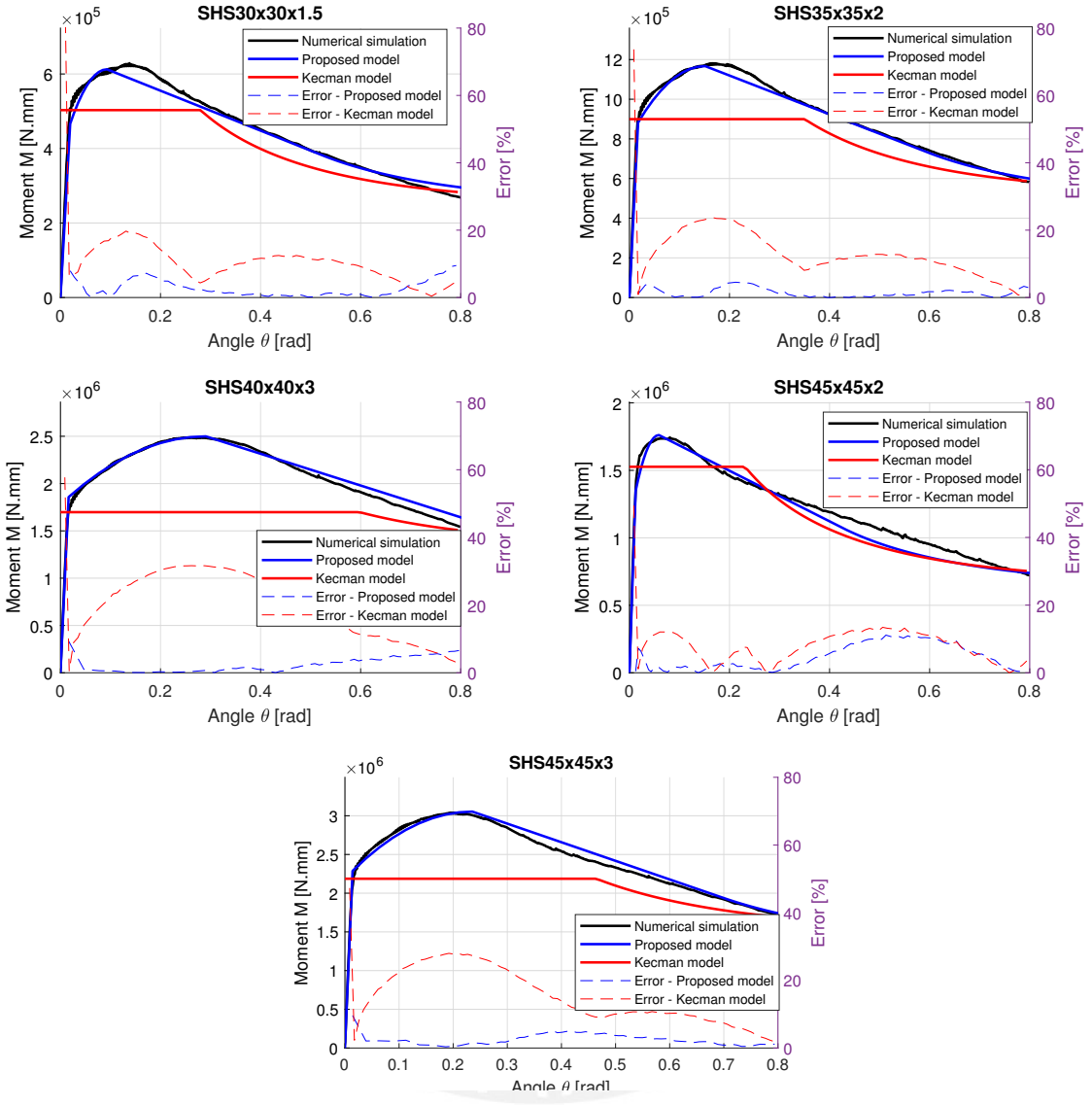

Figure 4.18: Comparison between the $M - \theta$ curves for the various SHS tested.

Another important comparison is the energy absorbed by each approach, which can be calculated by the area under each one of the aforementioned curves. The energy absorbed or work results for each case is detailed in Table 4.7 along with its error with respect to the numerical simulation result. These results seem to also indicate that the proposed corrections are able to reproduce the results obtained by numerical simulations with a better accuracy than the original model. The largest error in Table 4.7 for the proposed approach reaches 3.98%, whereas the highest error for the original model reaches 20.57%, which corresponds to shape with highest t/b ratio. On the other hand, the shape where the original model has the lowest error is also the one with the lowest ratio t/b. This further confirms that the introduced parameters are useful in predicting not only the maximum load, but the energy absorbed as well.

Table 4.7: Comparison between the energy absorbed (area under the curve) calculated by each method for the SHS.

Size	Numerical simulation	Theoretical (proposed)	Theoretical (original)	Error (proposed)	Error (original)
30x30x1.5	356.66 J	351.34 J	322.75 J	1.49%	9.50%
35x35x2	717.41 J	705.635 J	624.26 J	1.64%	12.98%
40x40x3	1671.06 J	1691.01 J	1327.34 J	1.19%	20.57%
45x45x2	959.36 J	921.19 J	907.08 J	3.98%	5.44%
45x45x3	1946.45 J	1966.68 J	1638.32 J	1.04%	15.83%

Rectangular hollow shapes

A similar analysis is performed for the RHS using the corresponding surface fits and is shown in Fig. 4.19. The approximation for RHS seems to generate larger errors than the SHS, reaching 10% and, in one case, up to 30 % for the proposed model, and around 30% for the original model. The cases that display larger errors seem to be those where the maximum moment or M_m occurs at a "plateau" and tends to overestimate θ_m, meaning that the proposed modification still has some trouble at predicting where this load occurs. Furthermore, the error seems to oscillate in some scenarios. This oscillation occurs because c_e is obtained by matching the energy absorbed (area under the curve) using the numerical model after the maximum load is reached, thus it tries to compensate the areas under the curve.

It is important to notice that for shapes with low ratios of t/b (thin-walls) and low ratios of b/a (wide), both predictions of the maximum moment (proposed model with modifications and Kecman's) provide almost the same value of M_m. However, the proposed model shows better performance at predicting the maximum moment in all cases. The original model also shows deficiencies when making predictions for narrow shapes. For instance, two positions for the same shape RHS30x50x2 and RHS50x30x2 are tested. In both cases, the prediction by the proposed model offers a better approximation of the numerical curve but the error for the original model significantly grows when this shape is switched from RHS30x50x2 to RHS50x30x2. This last comparison is important, since it gives insight into the importance of a ratio of thickness and width t/a. However, even when this parameter is not directly investigated, its influence is indirectly included and taken into account in the surface fits for RHS.

Similarly as with the SHS, the area under each curve of each RHS verification case is calculated and shown in Table 4.8. In general, the proposed model seems to predict thee area under the curve better than the original model; however, there are some cases with apparent exceptions. The first apparent exception is the case where the original model predicts the area under the curve with less error than the proposed model, precisely RHS 30x50x2. It is worth noting that the difference between errors is almost negligible (2.89% to 1.65%) and the proposed model has a better prediction for the maximum moment. The second exception occurs with RHS 40x60x4, where both errors are larger than 10%. This large error is due to an overestimation of θ_m for these dimensions, most likely due to M_m occurring at a "plateau", and not at an exact point.

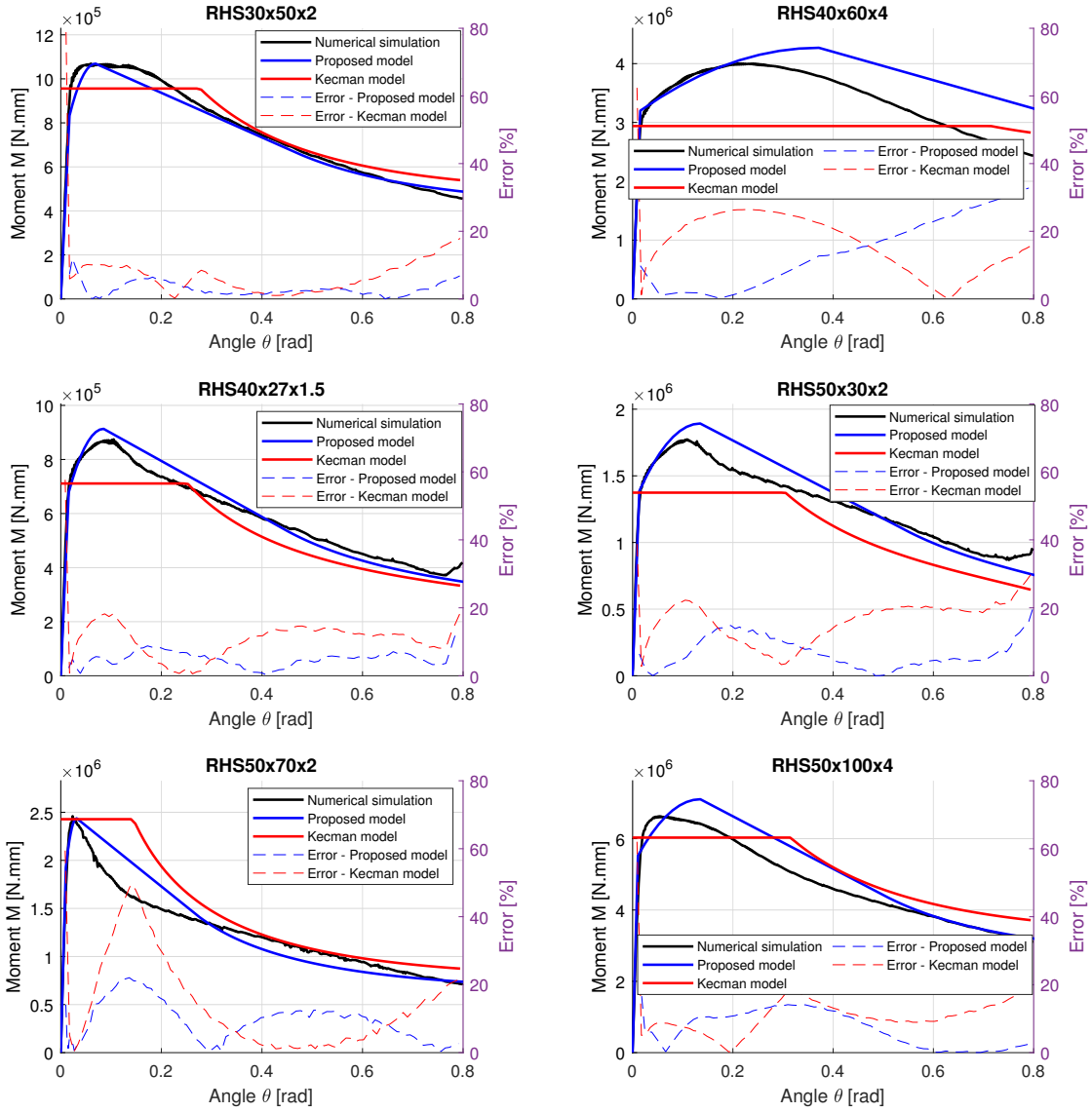

Figure 4.19: Comparison between the $M - \theta$ curves for the various RHS tested.

Table 4.8: Comparison between the energy absorbed (area under the curve) calculated by each method for the RHS.

Size	Numerical simulation	Theoretical (proposed)	Theoretical (original)	Error (proposed)	Error (original)
30x50x2	603.29 J	585.81 J	613.23 J	2.89%	1.65%
40x20x2	829.68 J	862.05 J	498.52 J	3.90%	39.9%
40x27x1.5	471.48 J	472.64 J	427.50	0.24%	9.32%
40x60x4	2701.53 J	3022.72 J	2329.42 J	11.89%	13.77%
50x30x2	1024.15 J	1059.39 J	872.18 J	3.44%	14.84%
50x70x2	1004.79 J	1024.39 J	1168.79 J	1.95%	16.32%
50x100x4	3794.85 J	4049.37 J	4055.56 J	6.70%	6.87%

Comparison with experimental results

Another important observation can be made when comparing the experimental test results with those from the proposed model. Four sets of results are compared against the exper-

imental curves in Fig. 4.20: 1) the proposed model with the actual mechanical properties and real θ_m (extracted from tensile tests in Fig. 4.7), 2) the proposed model with the nominal mechanical properties (from Table 4.6), 3) the original Kecman model calculated using the nominal mechanical properties, and 4) the original Kecman model using the actual mechanical properties. The goal of this comparison is to verify the capabilities of the proposed model to predict the actual $M - \theta$ curves based on the nominal mechanical properties, as well as to check its accuracy when using the experimental data. The most evident improvement of the proposed model when compared to the Kecman model is, once again, the prediction of M_m, even when using the nominal mechanical properties. This prediction is further improved when the experimental data is used. It should be noted, that this improvement is more noticeable with thicker shapes (SHS25x25x2 and SHS50x50x4). It should also be noted that for the thinner shapes such as (SHS 50x50x2 and RHS30x80x1.5), all predictions seem to agree, which means that the proposed model also works with thin-walled shapes. However, the model apparently still lacks the ability to adequately determine θ_m with nominal material data. The authors theorize that the origin of this difference comes from the strain at which the ultimate stress occurs in the material model (probably due to loss of ductility in during forming), which directly affects how "soon" the maximum moment occurs. The material model used for simulations and posterior calculations does not take into account the loss of ductility from manufacturing, which cannot be known without a tensile test. However, in the early stages of design, having a better prediction with nominal data is of great importance.

4.5 Conclusions

A modified approach to calculate the maximum moment and collapse behavior, for steel SHS and RHS is proposed. The proposed modification is mostly based on Kecman's theory and serves to includes the so-called "medium-thin-walled" shapes, commercially available by steel distributors, and widely used in many industries, such as the automotive industry when constructing bus structures. The bending collapse behavior of the thinner shapes can be described by Kecman's original theory with acceptable accuracy. However, the behavior of thicker or "medium-thin-walled" shapes is better described when including the proposed modifications. The thickness is found not to be the issue, but the thickness relative to the height of the hollow shape, or thickness-to-height ratio t/b. The influence of the width ratio b/a is also explored for RHS. It is found that larger values of b/a, or narrower shapes, tend to increase the load required for bending collapse. Also, the thicker and narrower a hollow profile is, the larger θ_m grows. This last observation is of major importance, since many of the previous works consider that, the behavior previous to the collapse, along with θ_m, is negligible, which is not true for the sizes evaluated in this study.

The reasons for which the original Kecman theory fails to identify the maximum load and collapse behavior in "medium-thin-walled" hollow shapes have also been explored. The main reason is that apparently, due to the larger relative thickness t/b, not all points in the through-the-thickness direction of the cross section suffer yielding at the same time, and a larger load is required to completely form the corresponding hinge lines. This fact has three major implications: (1) First, the maximum bending moment is significantly increased. (2) Since the rest of the beam is still deforming until the real maximum bending moment is reached, θ_m also increases, meaning that the behavior previous to the collapse, namely the elastic–plastic stage (see Fig. 4.3), is no longer negligible. (3) Hinge lines can no longer be clearly defined (recall Fig. 4.4), and thus the kinematic incompatibilities in the original model, found by some authors such as T. H. Kim and Reid (2001), may play a larger role. The limitation of the original model is addressed by including two parameters a_e, c_e, which are used to determine an effective yield stress σ_{Ye}, and effective

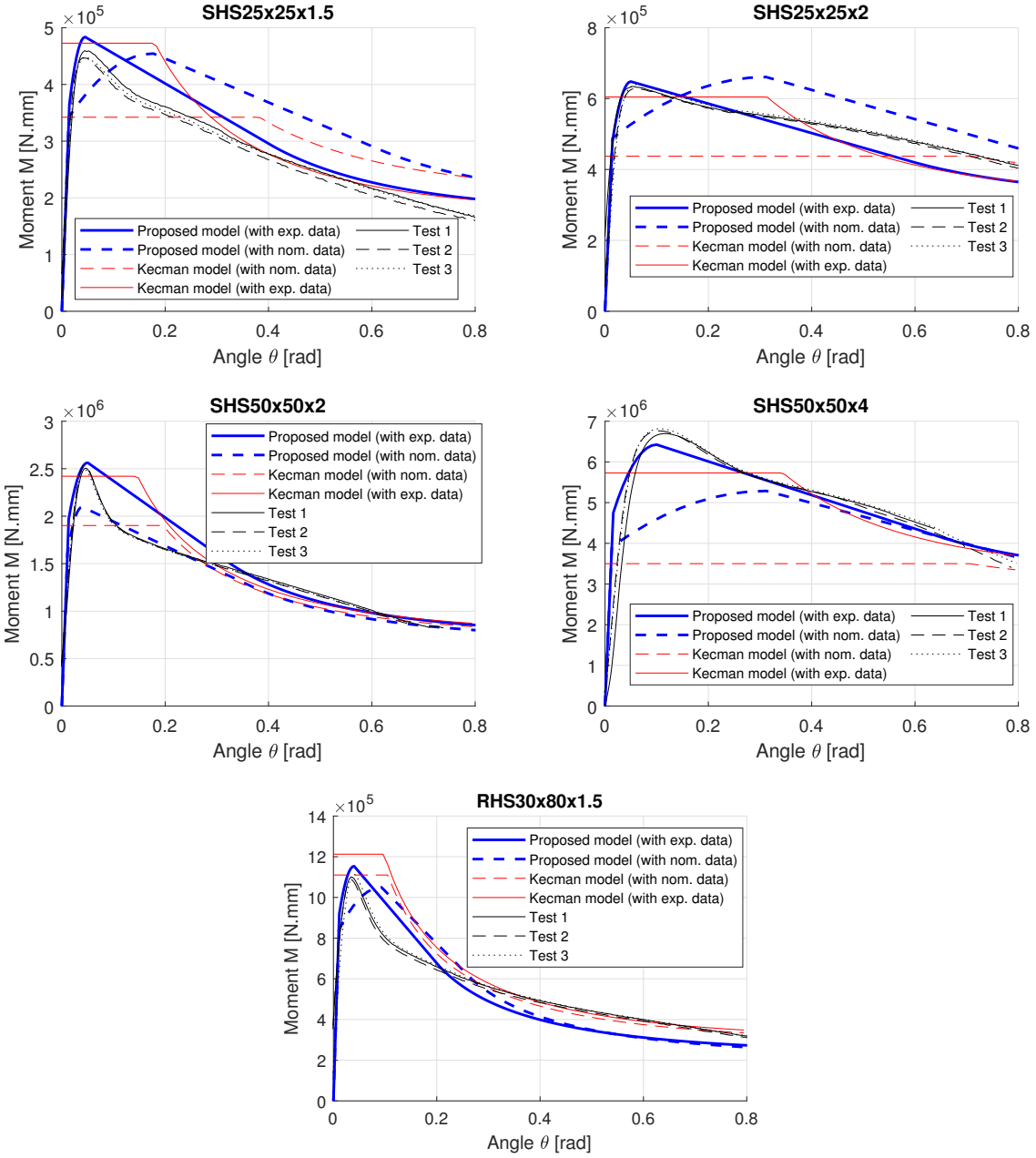

Figure 4.20: Comparison between the experimental and proposed theoretical models, using the nominal properties for S275.

flow stress σ_{0e}, respectively; as well as a prediction for the angle θ_m. All three parameters are dependent on the ratios t/b and b/a. In general, the parameters seem to provide better predictions for the SHS than for the RHS. However, this may be due to the fact that there are relatively less sampling points for RHS. Even considering this limitation, the inclusion of parameters a_e, c_e and θ_m seems to significantly improve, in most cases, the predictions for both SHS and RHS. This improvement is far more noticeable in the prediction for M_m through a_e, which indicates than an alternative for factor c_e would be useful.

An important remark is that the proposed model can offer improvements in the approximation of a real $M-\theta$ curve. The results obtained with the nominal material data could be considered as a "fast" approximation of the actual curve, as it does not require experimental data fed. In Fig. 4.20, it can be seen that the results offered by the proposed model, even when using the nominal data, are improved when compared to the

original model. The proposed model can further improve its prediction if the experimental data is provided. The proposed model can be thus considered an adequate adaptation of Kecman's model for medium-thin-walled shapes.

This study also serves the purpose to continue the research into thin-walled structures used in various industry, especially as it provides the means to predict the maximum load and energy absorption characteristics of SHS and RHS. In turn, this research can help with better design choices in early design stages; since the calculation times are in the order of seconds and offer better approximations than Kecman's model with nominal material data, whereas the time needed for the numerical simulations or experimental tests is in the order of hours. Better design choices early can result in lighter and safer structures.

Chapter 5

Theoretical and experimental study of the bending collapse of partially reinforced CFRP-Steel square tubes

This article consists of the publication: Lavayen-Farfan et al. (2022).
Bending collapse of thin-walled steel tubes is a major energy absorption mechanism in lightweight structures, especially for crashworthiness. External composite reinforcements can increase the energy absorption and strength of steel tubes. However, to this date there are still difficulties to determine the maximum load and the collapse behavior of reinforced, multi-material shapes, e.g., steel shapes covered by CFRP. In this work, a theoretical analysis of the collapse of a partially reinforced CFRP-Steel tube is performed, which encompasses the calculation of both the peak bending moment and the bending collapse curve of tubes with either the flanges or webs with reinforcements. The theoretical approach is validated with three-point bending experimental tests and an adequate agreement with experiments is found. The results also show an important increase of up to 57% in the peak load and 45% in the specific energy absorbed for partially reinforced tubes, with a maximum 14% increase in weight, when compared with unreinforced tubes. The developed theoretical model enhances even further the existing bending collapse theories, as it incorporates reinforcements in the model and provides a powerful tool for engineering analyses, and can be implemented in concept models, and optimization algorithms with ease. These findings can be used for enhancing existing and new lightweight structures and improving the crashworthiness of several automotive structures.

5.1 Introduction

Hollow steel shapes are widely used in manufacturing of lightweight structures, for their availability, price, and strength-to-weight ratio. However, when they are under high bending loads, they are prone to localized collapse, which generates a plastic collapse hinge in the zone with the largest bending moment. The formation process of the plastic collapse hinge can be used as a major energy absorption mechanism in many fields, especially as a safety measure in case of accidental impacts. Lightweight design requires the use of the full load capacity of a material, which means using and taking advantage of the plastic deformation process, well beyond the elastic limit (K. Friedrich & Almajid, 2013; Klein, 2013). In lightweight design, energy absorption mechanisms refer to the means in which the structure absorbs and dissipates kinetic energy, typically by suffering plastic defor-

mations in specific zones. Bending collapse and axial crushing of thin-walled tubes can be used to dissipate the kinetic energy of an impact in a structure as these processes are associated with large plastic deformations in specific zones. Thus, the energy absorption capability of a structure can be used as a measure of its crashworthiness. For instance, in vehicle structures, such as buses (UN/ECE 66, 2007), competition vehicles (Federation Internationale De l' Automobile, 2018), and heavy machinery, the plastic deformation zones of the rollover or safety cages can be used to provide protection during accidents: the structure deforms and suffers plastic deformations, absorbing energy in controlled manner to avoid severe injuries for the occupants and even heartbreaking fatalities. Thus, an adequate design and calculation of the structure is required and a considerable amount of research (Bambach, 2014; Fragassa et al., 2020; Gepner et al., 2014; Hashemi et al., 2009; Hong & Huang, 2014; Liang & Le, 2009, 2010a; Q. Liu et al., 2013; Roca et al., 1997; Su et al., 2011; Yu et al., 2015; Zhou et al., 2019) has been devoted regarding the localized collapse of tubes under bending and its influence on structures under static and dynamic loads. As another example, the interior structure of wind turbine blades can also be susceptible to collapse and even modeled as a hollow shape, as shown by X. Chen (2017) and J. Tang and Chen (2018).

Kecman (1979, 1983) was among the first authors to describe the bending collapse of thin-walled square and rectangular tubes in the early 1980s. This work was followed by studies of bending and axial collapse by Abramowicz and Jones (1997), Wierzbicki and Abramowicz (1983), and Wierzbicki et al. (1994a, 1994b), Brown and Tidbury (1983), T. H. Kim and Reid (2001), among others in recent years (Huang & Zhang, 2018; Huang, Zhang, & Fu, 2020; Lavayen-Farfan et al., 2021). The analyses are often based on the formation of numerous hinge lines along the webs and flanges of the zone prone to collapse, and the computation of the energy absorbed by each hinge line. Related research has also been devoted to increase the energy absorption and maximum load that can be endured. For instance, authors such as X. Zhang, Zhang, and Wang (2016) worked on shapes with variable thicknesses and found that optimizing the thickness in the upper portions of the webs provides a significant increase in the absorbed energy. As an alternative, multicell shapes can also be used (Bai, Meng, Wu, et al., 2019; Du et al., 2019; you Xie, 2020) or even corrugated reinforcements inside the shape itself (Vignjevic et al., 2019). On the other hand, numerous authors opted for reinforcing the exterior of the shape with a composite, typically Carbon or Glass Fiber Reinforced Polymers (CFRP and GFRP, respectively) (Dhaliwal & Newaz, 2020; Eksi & Genel, 2013; Huang & Zhang, 2020; Huang, Zhang, & Yang, 2020; Jung et al., 2009; H. C. Kim et al., 2013; Lee, Kim, et al., 2006; Ma et al., 2020). Lee, Kim, et al. (2006) found that an increase in the absorbed energy can also be achieved if the reinforcement layers are set on the top and bottom flanges, instead of all around it. This is a valuable observation, since it is not always possible to reinforce all around the shape. Some of the reinforcements shapes found in the literature are displayed in Fig. 5.1.

However, few authors have worked on theoretical approaches on reinforced tubes. Most of the developed works are experimental and numerical, such as Bambach (2014), Gliszczyński and Czechowski (2017), and Jakubczak et al. (2017). In the surveyed literature, no method to calculate the maximum or peak bending moment for collapse has been found. Only procedures to determine the response during collapse stage have been found, which are heavily based on Kecman's theory (originally thought for thin-walled metal shapes). An alternative to a theoretical approach is the use of numerical methods (namely FEM), which has been widely used; nevertheless, they often require of very long simulation times and computational power, as well as several experimental data as input. The advantage of a theoretical model is that it can be employed for design, evaluation and optimization of structures without the long implementation times.

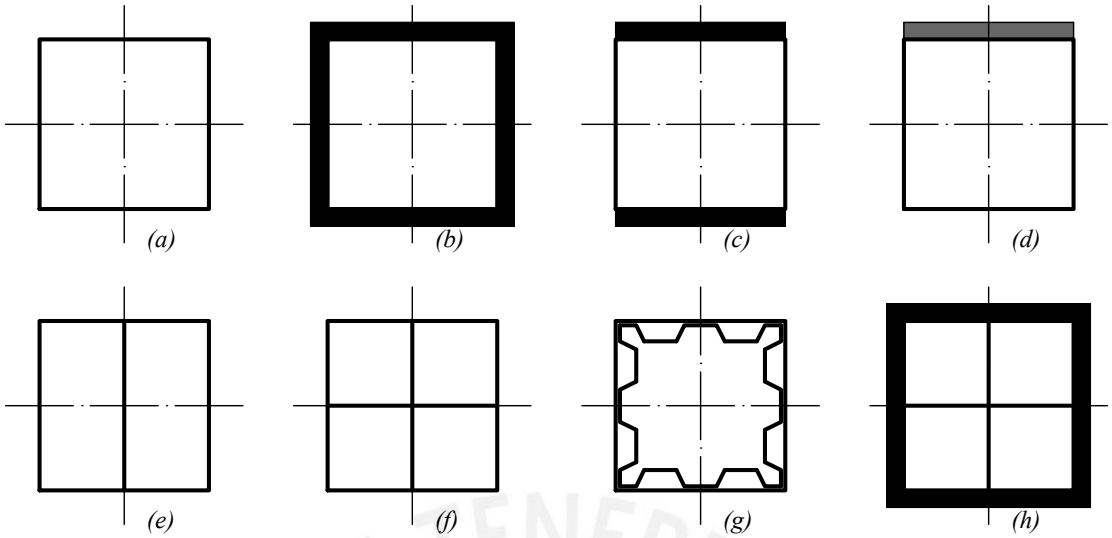

Figure 5.1: Different types of reinforcements for tubes found in the literature. a) no reinforcement, b) covered all-around with a composite, c) composite on the flanges, d) only on the top flange (or bottom flange), e) two-cells, f) four-cells, g) corrugated reinforcements, h) multi cell covered in composite.

In this work, the authors propose a method a determine the maximum collapse load of a reinforced square tube under bending load. The original hollow shape is considered to be medium-thin-walled, which itself requires certain modifications from Kecman's theory. Furthermore, two sets of reinforcements are used. The first set consists of flange reinforced shapes (UD reinforcements), which has been found in the literature and can be considered as a common and intuitive way of reinforcing a structural shape. The second set consists of web reinforced shapes (LR reinforcements), which seem counter-intuitive at first glance; however, the webs are the zones which absorb the most energy during bending collapse. The motivation for this work is to develop a theoretical model to determine the bending collapse curves for reinforced shapes in order to optimize the crashworthiness of a bus structure. These models have been proven to be extremely valuable when addressing the crashworthiness of lightweight structures. When studying frame structures, the moment-angle curves can be used to develop simplified FEM models with similar accuracy of detailed FEM models, with the advantage of reduced modeling and simulation times, as evidenced by Bai, Meng, Wu, et al. (2019), Bai, Meng, and Zuo (2019), Gui et al. (2018), and Park and Yoo (2008).

5.2 Design of the reinforcements of the square tubes

The goal of the reinforcement is to increase the energy absorption capabilities of the collapse zone of a structure. The critical zones are typically located near structural joints, since the internal bending moment usually reaches its maximum in these zones. An additional problem with these areas comes from welding. The zones prone to collapse are usually inside or near the HAZ (heat affected zone), reducing its ability to absorb energy. Additionally, reinforcing the whole shape all around may not be feasible, since other parts of the structure may need further assembly: either welding, bolting or riveting. This means that certain reinforcement types are actually not adequate for all applications. To overcome this difficulty, a partial reinforcement is proposed for these areas. Since bending collapse is a localized phenomenon, the reinforcement should not need to be applied in the whole length of the shape, only near the critical zones.

The proposed partial reinforcements have two possible variations: 1) reinforcements on the flanges, or up and down (UD reinforcements), and 2) reinforcements on the webs, or the left and right sides (LR reinforcements), not found in the surveyed literature.

As an example, both of the proposed reinforcements are modeled into an existing structural joint that is prone to collapse, seen in Fig. 5.2. Either reinforcement type leaves space to further assemble more components later on, either to the webs or to the flanges. The structural joint shown in Fig. 5.2 corresponds to the floor-column joint of a bus structure. It is worth noting that this joint is susceptible to bending collapse during a rollover.

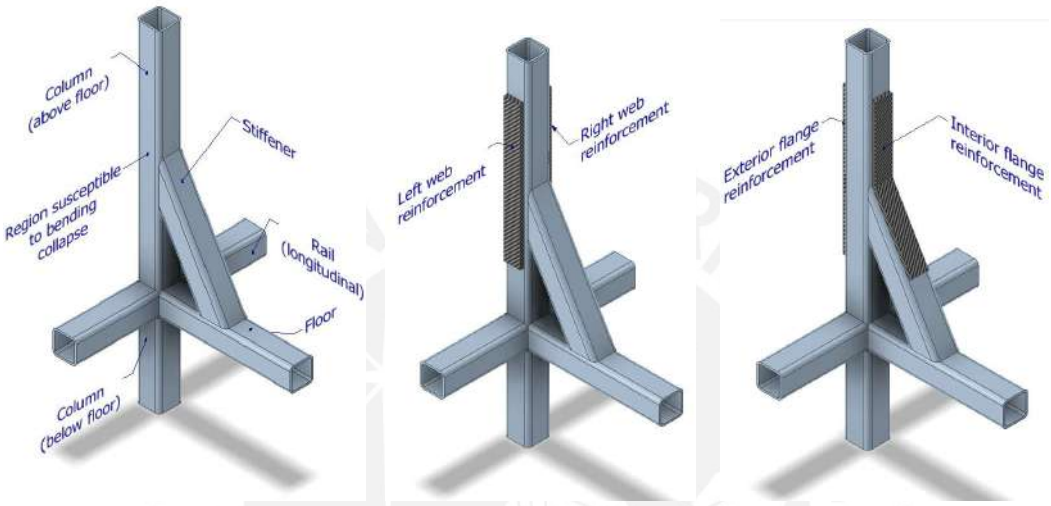

a) b) c)

Figure 5.2: Example of implementation of the proposed reinforcements on a floor-column joint of a bus. a) Original structure, b) Webs reinforced (LR reinforcement, c) Flanges reinforced (UD reinforcement). This assembly can be replicated in several lightweight structures.

In order to address the energy absorption capabilities of each type of proposed reinforcement, a three-point bending test of a representing test specimen is performed. The representing test specimen consists of a square, hollow, straight shape, with the reinforcements either on the flanges or the webs. A diagram of the three-point bending test is shown in Fig. 5.3. In this manner, the influence of the location of the reinforcement on the whole collapse behavior can be evaluated. To join together the steel shape and the composite reinforcement, a commercial impact-resistant adhesive is to be used in all test-specimens (more details in the Experimental setup section). The influence of components that might be further assembled near the reinforcement (on the free surface) is out of the scope of this study.

5.3 Theoretical analysis of the bending collapse with reinforced webs and flanges

The theoretical model by Kecman (1979, 1983) calculates the energy absorbed by each of the plastic hinge lines that form during the collapse stage of a metallic, thin-walled, hollow shape. The present analysis for reinforced shapes is based upon the original collapse theory by Kecman with modifications to include the medium-thin-walled shapes (Lavayen-Farfan et al., 2021), as well as further modifications to include composite reinforcements for the collapse stage (H. C. Kim et al., 2013; Mamalis et al., 1991), and an analysis of the critical

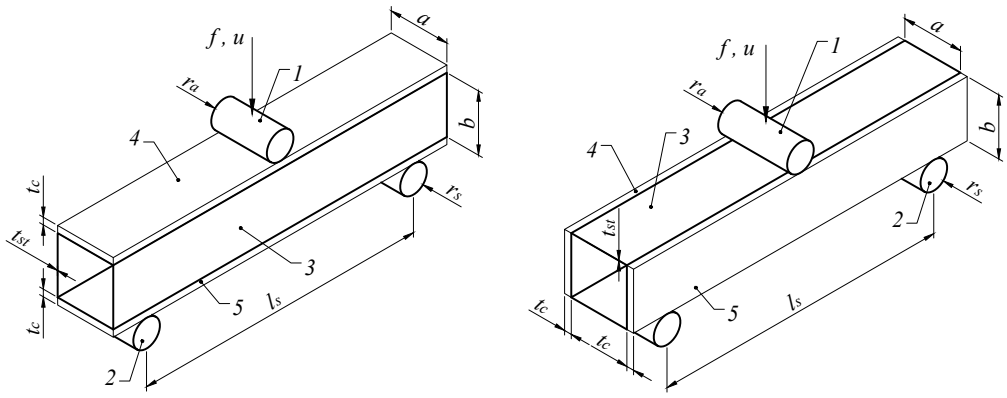

Figure 5.3: Three-point bending test scheme. 1: force applicator, 2: supports, 3: steel tube, 4 and 5: reinforcements for the flanges (left figure) and webs (right figure).

curvature for the maximum load, proposed by the present authors. Kecman's collapse theory calculates the energy absorbed by each of the plastic hinge lines that form during the collapse stage. Then, by performing a numerical derivation, the bending moment M at the hinge can be determined as a function of θ as follows:

$$M(\theta) = \frac{d}{d\theta}W \approx \frac{W(\theta + \Delta\theta) - W(\theta)}{\Delta\theta} \tag{5.1}$$

where $W = \Sigma W_i$ is the total energy absorbed by each of the hinge lines in the form of plastic deformation (each W_i term is described in the Appendix). It is important to note that not all hinge lines absorb the same amount of energy for a given angle θ. In Fig. 5.4, it becomes readily apparent that hinge lines associated with W_6 and W_7 are the ones that absorb the largest amount of energy. This means that the webs of the hollow shape (specifically the "bulge" portion) are the ones responsible for the most energy absorbed.

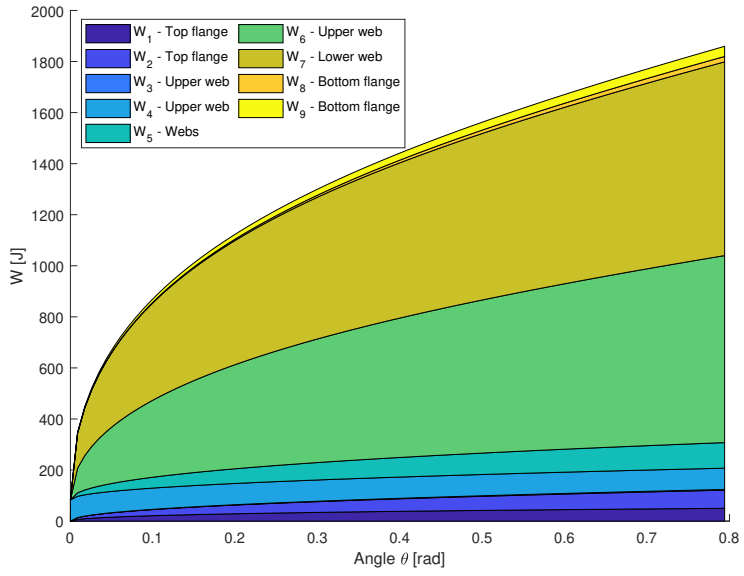

Figure 5.4: Comparison of the different W_i for each hinge line. Curve obtained using Kecman's original model with a S50x2 made of S275.

The calculation of each term of W_i also requires the determination of the hinge moment per unit length M_0. In the original Kecman model (Kecman, 1979, 1983), its value depends

on the nominal flow stress and the thickness of the shape, as shown in Eq. 5.2. However, this expression is only valid for a shape with no reinforcements. If a reinforcement, of any form, is to be implemented in a hollow shape then this equation needs to be adapted.

$$M_0 = \frac{1}{4}\sigma_0 t^2 \tag{5.2}$$

It is also worth noting, that medium-thin-walled shapes are used, which do not always follow Kecman's collapse theory and require a modification in the yield (σ_y) and flow stresses (σ_0), which are replaced by the effective yield (σ_{Ye}) and effective flow (σ_{0e}) stresses, as follows:

$$\sigma_{ye} = a_e\sigma_y + (1 - a_e)\sigma_B \tag{5.3}$$

$$\sigma_{0e} = c_e\sigma_y + (1 - c_e)\sigma_B \tag{5.4}$$

where a_e is the correction factor for the yield stress, c_e is the correction factor for the plastic flow stress, and σ_B is the ultimate strength. Both of these factors are dependent on the ratios t_{st}/b and a/b, as shown by Lavayen-Farfan et al. (2021).

For the FRP reinforcements, depending on their location, they may suffer a fracture after the maximum stress is reached. In the works by H. C. Kim et al. (2013) and S. Y. Kim et al. (2017), it is theorized that if the normal stress in the reinforcement reaches its tensile strength, then it will no longer be able to carry more loads and will be carried by the steel alone. This value is reached during the start of the collapse according to H. C. Kim et al. (2013) and S. Y. Kim et al. (2017). Thus, the hinge lines where the reinforcement is in tension may suffer fracture and will not carry any more load during the collapse stage. Only the hinge lines where the reinforcement is in compression will carry load during the collapse stage. The investigations by Mamalis et al. (1991) (although focused for axial crushing but still applicable) found an expression for the hinge moment per unit length for a composite hinge line (Eqs. 5.5 and 5.6), that depends on the thicknesses t_{st} and t_c, of the steel and composite, respectively; as well as on the flow stress of the steel σ_0 and the tensile strength of the composite σ_c, as seen in Eq. 5.5. However, this expression only holds true when $\sigma_0 t_{st} > \sigma_c t_c$. If this condition is not met, then Eq. 5.5 can be rewritten as 5.6. Previous works by other authors (H. C. Kim et al., 2013; S. Y. Kim et al., 2017; Lee, Kim, et al., 2006) showed that both equations work successfully for bending collapse in shapes completely covered with composite reinforcements.

$$M_0 = \frac{\sigma_0 t_{st}}{4}\left(1 + 2\frac{\sigma_c}{\sigma_0}\frac{t_c}{t_{st}} + 2\frac{\sigma_c}{\sigma_0}\left(\frac{t_c}{t_{st}}\right)^2 - \left(\frac{\sigma_c}{\sigma_0}\frac{t_c}{t_{st}}\right)^2\right) \tag{5.5}$$

$$M_0 = \frac{\sigma_c t_c}{4}\left(1 + 2\frac{\sigma_0}{\sigma_c}\frac{t_{st}}{t_c} + 2\frac{\sigma_0}{\sigma_c}\left(\frac{t_{st}}{t_c}\right)^2 - \left(\frac{\sigma_0}{\sigma_c}\frac{t_{st}}{t_c}\right)^2\right) \tag{5.6}$$

These expressions (Eqs. 5.5 and 5.6) can be then used in the calculations of W_i (seen in the Appendix), with the care that the hinge lines without the reinforcements should be calculated with Eq. 5.2. Note that, unlike works by previous authors, in the present work it is considered that the moment of the hinge lines, where the composite is under tension, can be calculated using Eqs. 5.5 or 5.6. This decision is taken due to the fact that the composite layers do not fracture immediately after the beginning of the collapse stage. Instead, they progressively deform and partially fracture. Furthermore, even when the collapse stage can be determined using Eq. 5.1 (based on the energy terms shown in Eqs. 2.4-2.12), it cannot obtain the maximum moment M_m by itself. In this work, it is proposed that M_m can be approximated using the maximum moment of a shape without reinforcements and adding the moment required to bend the reinforcements to the same

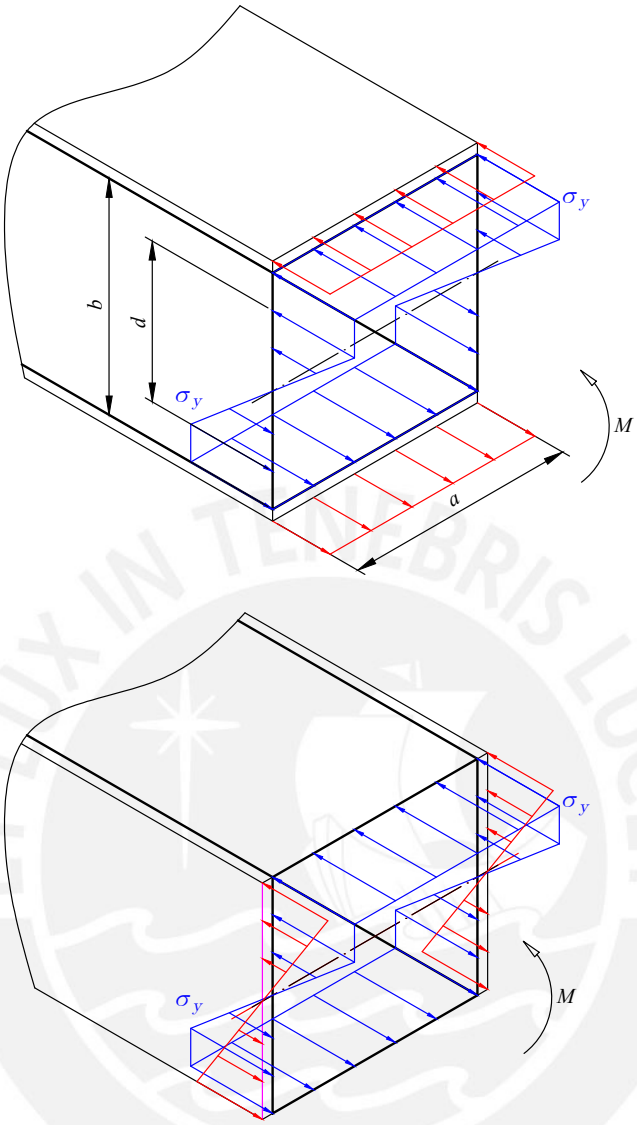

Figure 5.5: Stress distribution on the cross section of the steel shape (blue) and reinforcements (red) showing partial plastic stress in the steel portion.

curvature as the unreinforced shape, as shown in Eq. 5.7 or, in other words, by calculating the total moment obtained by the stress distribution depicted in Fig. 5.5.

$$M_m = M_{\text{m-steel}} + M_{\text{m-reinf}} \tag{5.7}$$

In Eq. 5.7, $M_{\text{m-steel}}$ can be determined using Eqs. 2.14 to 2.19, which are based on the works by Kecman (1979) and Rhodes and Harvey (1971) and corresponds to the moment determined with the stress distribution in blue in Fig. 5.5. The term $M_{\text{m-reinf}}$ can be then determined using the stress distribution along the reinforcements, which corresponds to the moment calculated with the stress distribution in red in Fig. 5.5. It is also considered that the composite plates have the same curvature as the deformed steel shape $\kappa = \kappa_{\text{crit}}$, produced by $M_{\text{m-steel}}$, as seen in Eq. 5.8. The reinforcements are assumed to still behave in their elastic stage as revealed by footage taken during the experiments using a high speed camera.

$$M_{\text{m-reinf}} = \kappa_{\text{crit}} E_c I_c \tag{5.8}$$

From Eq. 5.8, all terms can be readily defined: E_c is the Young modulus of the

composite; I_c is the moment of inertia of the cross section of the reinforcements measured from the neutral axis of the square tube, the thickness of the adhesive layer needs to be considered in this term when required; κ_{crit} is the curvature produced by $M_{\text{m-steel}}$. It can be noted, that $M_{\text{m-steel}}$ is generally obtained by considering that some portion of the whole SHS section is under plastic stress (defined by the dimension d in Fig. 5.5) and the value of the critical stress σ_{cr} (Eq. 2.14). If the collapse is elastic, d can be set to b and the curvature can be set to the corresponding κ_y (produced when the outermost part of the shape reaches the yield stress σ_y). If the collapse is elasto-plastic, d is lower than b and the curvature κ depends on how large is the plastic portion (defined using the parameter $\lambda = \kappa/\kappa_y$ in Eq. 5.9). Lastly, if the collapse is plastic, d is set to zero. For this last case, the maximum moment is actually an asymptote for λ (this occurs regardless of the cross section (Megson, 2019)).

$$M_{\text{m-steel}} = M_y + \frac{\sigma_y t_s t b^2}{6}\left(1 - \frac{1}{\lambda^2}\right) \tag{5.9}$$

Since an infinite value of λ cannot be used, this value should be approximated. Analyzing the behavior of λ and its influence on $M_{\text{m-steel}}$, it is theorized that a value of λ between 2 and 4 should be enough to guarantee at least 95% of the fully plastic moment M_p (see Eq. 2.17) and correctly predict the maximum moment obtained in testing. However, the adequate value of λ has to be determined experimentally.

The collapse stage is then calculated using Kecman's model, using Eqs. 5.5 and 5.6, the consideration of medium-thin-walled shapes shown in Eqs. 5.3 and 5.4, and a further empirical modification to the so-called rolling radius, to account for the different materials and increased thickness. The original, empirical expression used by Kecman is adapted for this case as follows:

$$r_{roll} = \left(0.07 - \frac{\rho}{200}\right) h \tag{5.10}$$

Once the collapse stage and the maximum moment M_m are defined, the elastic and elastic-plastic stages can also be defined. The elastic stage is defined as a line that connects the origin with the point (θ_y, M_y) (when the outer zones of the steel reach the yield stress). Whereas the elastic-plastic zone is defined as a parabola that connects points (θ_y, M_y) and (θ_m, M_m), and has its vertex on (θ_m, M_m). This procedure is also described by Lavayen-Farfan et al. (2021).

It is also worth noting that the properties of the adhesive are not considered in any part of the theoretical analysis for the maximum load and collapse stage. It is considered that the adhesive completely transfers the load from the steel to the reinforcement. This supposition is based on the fact that the chosen adhesive is a high strength, impact resistant, structural adhesive. To further verify this supposition, a single lap joint test is performed on the adhesive to obtain its peak shear stress.

5.4 Experimental setup

5.4.1 Materials and preparation

The hollow shapes follow the standard EN 10219 and EN 10305 and are made from steel S275. These shapes were provided by a local supplier. The reinforcements are manufactured from a plate 2.5 mm thick of CFRP. The polymer matrix of the CFRP is epoxy resin Sicomin 8500 with the hardener Sicomin SD8601 (both supplied by Sicomin Epoxi Systems, Chateauneuf-les-Martigues, France). The fiber is the balanced, woven, bidirectional carbon fiber GG600T (supplied by Mel Composites, Barcelona, Spain). The CFRP plate is manufactured by hand lay-up of four layers of carbon fiber and cut to strips of the desired dimensions after curing. The strips of CFRP are then fixed to the

sides of the steel shapes using Sikapower 1277 two-component adhesive (provided by Sika SAU, Spain), which is based on epoxy resin and has micro-spheres to guarantee a constant thickness. This structural adhesive has a high mechanical resistance and is also adequate for impact scenarios. The surface of the steel shapes are previously prepared by sanding them with P180 sandpaper, followed by a cleaning process with ethanol. The CFRP is also cleaned with ethanol to remove any impurities. The adhesive layer has a thickness of 1 mm. Any excess of adhesive is removed before it cures.

5.4.2 Three-point bending test

In order to verify the strength and the energy absorption capabilities of both reinforcement types, three-point bending tests are performed. Unlike cantilever tests used by Kecman, three-point bending tests do not require complex preparations and can be set up on a universal testing machine as long as sufficient length between supports is provided to avoid indentation (Lavayen-Farfan et al., 2021). Three square hollow shape sizes are picked, with different thickness-to-height (t_{st}/b) ratios. Each of these shapes is reinforced with both reinforcement types, the detailed list of explored sizes is shown in Table 5.1. The first three rows of Table 5.1 describe the unreinforced specimens used as control or baseline. The unreinforced shapes and their results correspond to a previous study by the authors (Lavayen-Farfan et al., 2021).

Table 5.1: Test specimens sizes and reinforcements

Designation	Base shape $b \times a \times t_{st}$	Reinforcement	t_{st}/b
S25x1.5	25x25x1.5	none (baseline)	0.06
S25x2	25x25x2	none (baseline)	0.08
S50x2	50x50x2	none (baseline)	0.04
UD25x1.5	25x25x1.5	Up and down	0.06
UD25x2	25x25x2	Up and down	0.08
UD50x2	50x50x2	Up and down	0.04
LR25x1.5	25x25x1.5	Left and right	0.06
LR25x2	25x25x2	Left and right	0.08
LR50x2	50x50x2	Left and right	0.04

*b, a and t_{st} are expressed in milimeters.

The separation between supports l_s must be large enough to guarantee bending collapse, that is: $l_s/b > 8$ (see Fig. 5.3) (Huang & Zhang, 2018). For the test specimens with sides of 25 mm, a set of support cylinders of $r_s = 15$ mm is used, with a separation $l_s = 250$ mm. For the larger specimens with sides of 50 mm, a larger set of support cylinders of $r_s = 24$ mm is used, with a separation of $l_s = 450$ mm. For all sizes, the applicator has a radius of $r_a = 15$ mm. The experimental setups for both reinforcements can be seen in Figs. 5.6 and 5.7.

Testing is carried out in a Microtest-brand universal testing machine (set in compression mode) with a maximum load of 200 kN. The load is applied downwards via the force applicator in the middle, which descends at a rate of 1 mm/s. The support cylinders are kept in place during the whole experiment. The testing machine registers data of the reaction force and displacement of the force applicator, which can be used to graph a $f_y - u_y$ curve. Notice that for a better comparison, the $f_y - u_y$ curves from the testing machine are not used, but instead they are converted to bending moment - hinge angle $M - \theta$ curve. To perform the conversion, formulas from technical mechanics for a simply

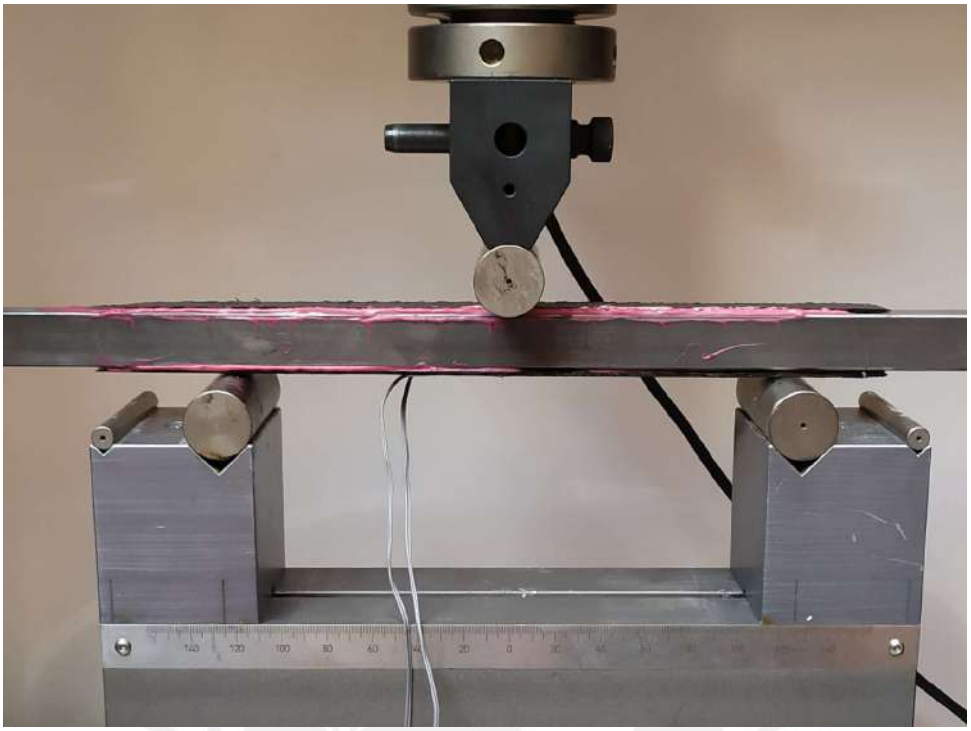

Figure 5.6: Square shape with UD reinforcements before the test.

supported beam with a concentrated load in the middle can be used:

$$M = \frac{f_y l_s}{4} \tag{5.11}$$

$$\theta = 2 \arctan\left(\frac{2u_y}{l_s}\right) \tag{5.12}$$

For each size and reinforcement variant, the test is repeated three times to ensure the repeatibility of the results.

5.4.3 Material properties characterization

It is also important to characterize the steel, the CFRP, and the adhesive for the theoretical analysis. For the steel used in the base tubes, tensile test of coupons are taken from the sides, which comply with the dimensions specified on ASTM A370. Two coupons were obtained from each shape provided by the manufacturer. It should be mentioned that although the shapes were commercialized under the same designation S275, they do not necessarily have the exact same mechanical properties. However, they do comply with the minimum requirements to be classified as S275. The averaged results of the tensile tests can be seen in Fig. 5.8.

Table 5.2: Tensile test results for the structural shapes

Shape	Yield stress [MPa]	Tensile stress [MPa]	Elongation [%]
S25x1.5	380	410	17
S25x2	380	400	31
S50x2	350	508	21

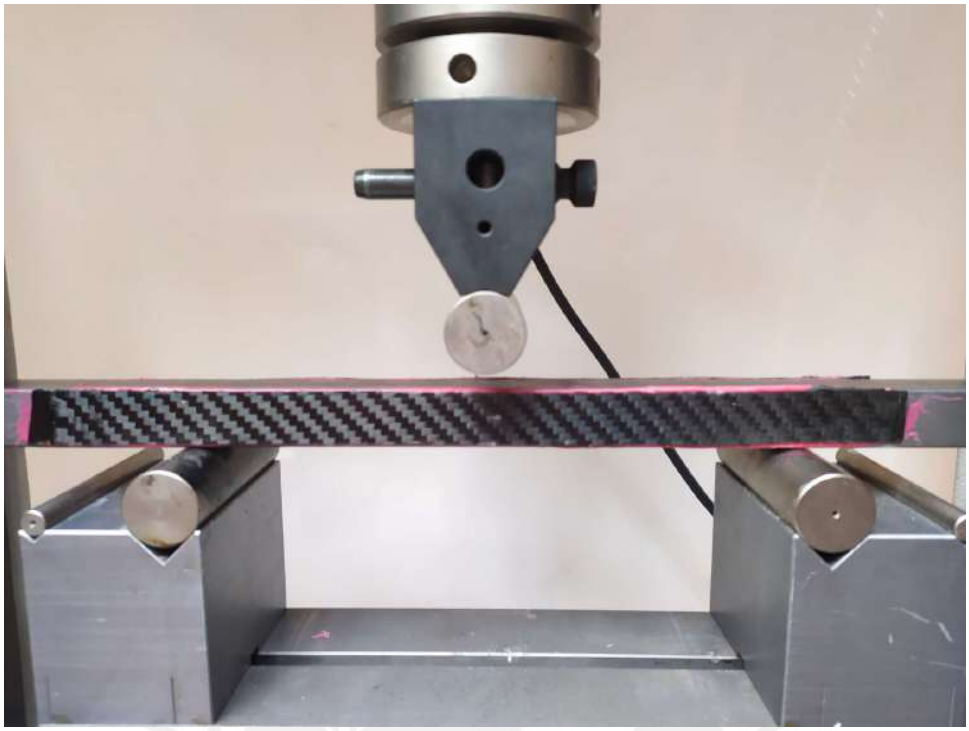

Figure 5.7: Square shape with LR reinforcements before the test.

Moreover, the mechanical properties of the CFRP also need to be determined. For this purpose, bending tests are performed on strips obtained from the same plates used for the reinforcements. Since the plates are made from bidirectional woven carbon fibers, the properties are assumed to be the same in the longitudinal and transverse directions. The results can be seen in Fig. 5.9.

The adhesive must be also characterized to quantify its shear strength. The adhesive is tested using a single lap test, and the maximum load is recorded. The peak load reaches a value of 6.85 kN. The average shear stress for the aforementioned peak load is 21.92 MPa.

5.5 Results and discussion

The experimental results of the reinforced tubes show an important increase in both the maximum moment and the absorbed energy when compared with the unreinforced shapes. A comparison between the $M - \theta$ curves for shapes with and without reinforcements can be seen in Figs. 5.10 to 5.12. The unreinforced shapes serve as control specimens to quantify the increase in strength and SEA. An important remark is that for each tested variant, similar results and failure modes are encountered. Each reinforcement type shows a distinctive failure mode which is discussed below.

5.5.1 Up and Down (flange) reinforcements

One of the main failure modes found in the flange reinforcements is shear delamination or mode II failure in the "down" reinforcement of UD25x1.5 and UD25x2. This failure produces the sudden drop in resistance shown in Fig. 5.10 and 5.11. From applied mechanics, it is known that during a three-point bending test, the shear force along the whole length of the specimen is constant and independent of the length. This means that both the adhesive and the composite are subjected to the same shear stresses along the length

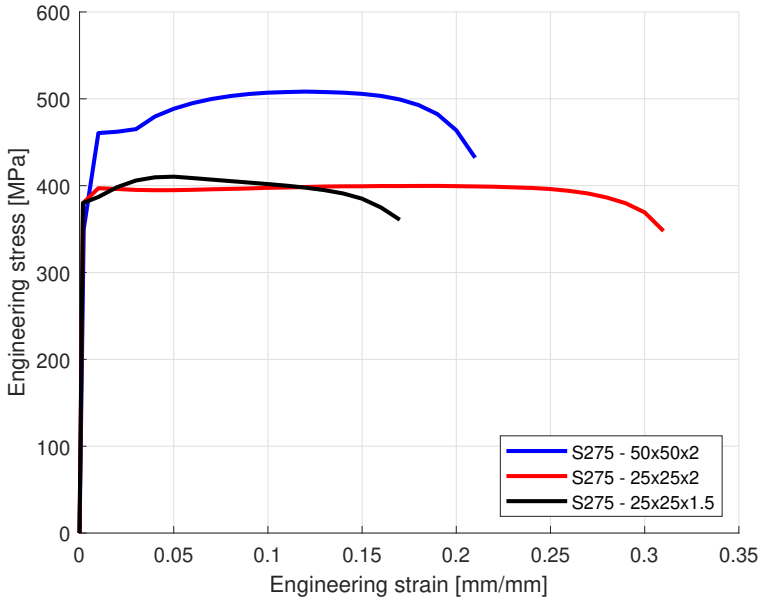

Figure 5.8: Stress and strain tests results for steel coupons of S275.

(produced by the shear force). Since the shear force is independent of the span between supports, so is the shear stress. This means that when the adhesive (or composite) fails under mode II, it fails and fractures along the whole length simultaneously, which can be seen in Fig. 5.13 and in the sudden drops in Figs.5.10 and 5.11. Out of the UD50x1.5 and UD50x2 tests, mode II failure on the CFRP occurred in 4 of them and separated the "down" reinforcement in half, as seen in Fig. 5.13. It should be also noted, that the remaining plies of CFRP (still attached to the steel shape) are still able to withstand the applied load and start to show signs of bending failure. In two cases, the CFRP failed due to excessive bending strain in the lower portion of the plastic zone, as seen in Fig. 5.14, where the failure can be clearly seen.

Due to the distribution of shear strain in the cross section (a parabola with the vertex in the middle), the adhesive actually is under a larger shear strain than the CFRP, however, it is observed that the CFRP is more likely to fail in mode II. It can be then deduced that the choice of adhesive is adequate for this application, as the CFRP fails before the adhesive. However, it should also be noted that not all fibers are actually breaking when delamination occurs, thus still providing some bending stiffness and resistance. This translates into the curve not dropping suddenly after the delamination occurs in the "down" reinforcement, but keeping the internal moment at a certain level. This fact is remarkably useful, since it means that although failure and delamination have occurred, the shape can still absorb a significant amount of energy as it continues to deform.

As for the UD50x2, a severe indentation occurred, as displayed in Fig. 5.15. It could be argued that the extra height provided by the reinforcements produced a ratio $l_s/b = 7.89$ (total height $b_{\text{total}} = 57$ mm); which according to Huang and Zhang (2018) would produce significant indentation. Unlike the UD25x1.5 and UD25x2, there is no observable mode II failure with UD50x2, the authors theorize that this fact is more related to the influence of the ratio t/b rather than the influence of the indentation. The UD reinforced shape with lowest t/b, namely UD50x2, does not show mode II failure. A slightly thicker shape UD25x1.5 shows mode II failure occurring at angles between 0.4 to 0.65 rad. An even thicker shape, shows mode II occurring at angles less than 0.3 rad.

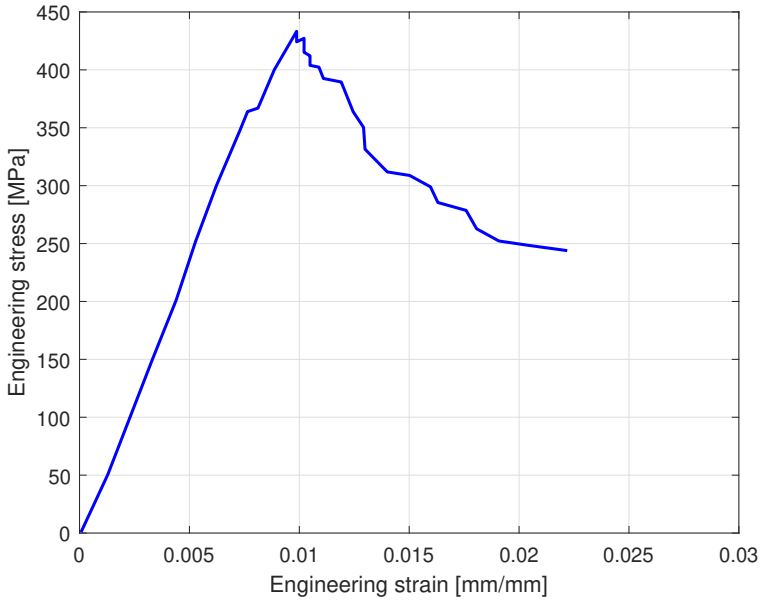

Figure 5.9: Stress and strain tests results for the CFRP in a bending test.

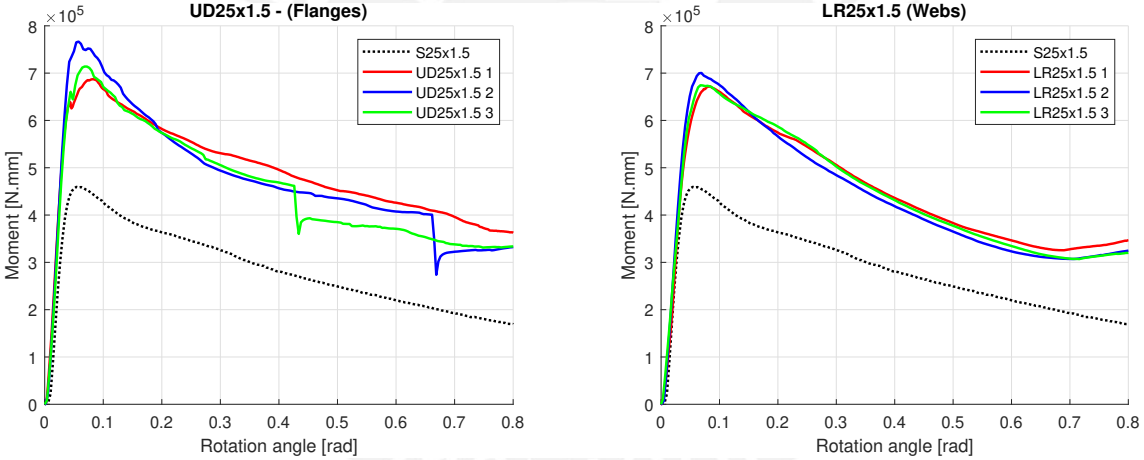

Figure 5.10: Comparison between S25x1.5, UD25x1.5 and LR25x1.5.

5.5.2 Left and Right (webs) reinforcements

The main failure mode found is bending fracture of the composite on the "bulges" that form in the plastic hinge in the middle of the test specimen. These areas suffer high bending deformations as seen in Figs. 5.16-5.18. Since the composite plates suffer larger bending deformations than the metal part, both the matrix and fibers of the outer layers fracture. However, testing showed that fracture does not occur immediately after the maximum moment is reached. Instead, these zones provide stiffness and resistance in the early stages of collapse. As the bending angle θ increases, the composite reinforcements begin to fracture in the outer layers of the upper portion, the strength decreases, and separation begins in between the plies of the CFRP reinforcement until it reaches the adhesive. A mixed (mode I and II) fracture occurs in the bulge area. All tested specimens showed delamination in this zone. In one case, the delamination extended to a considerable length (Fig. 5.17). Only in the larger LR50x2, the adhesive fractured significantly more than the CFRP (see Fig. 5.18), however, this is a localized phenomenon, and does not indicate that the whole length of adhesive fails. It should be noted that, unlike the other

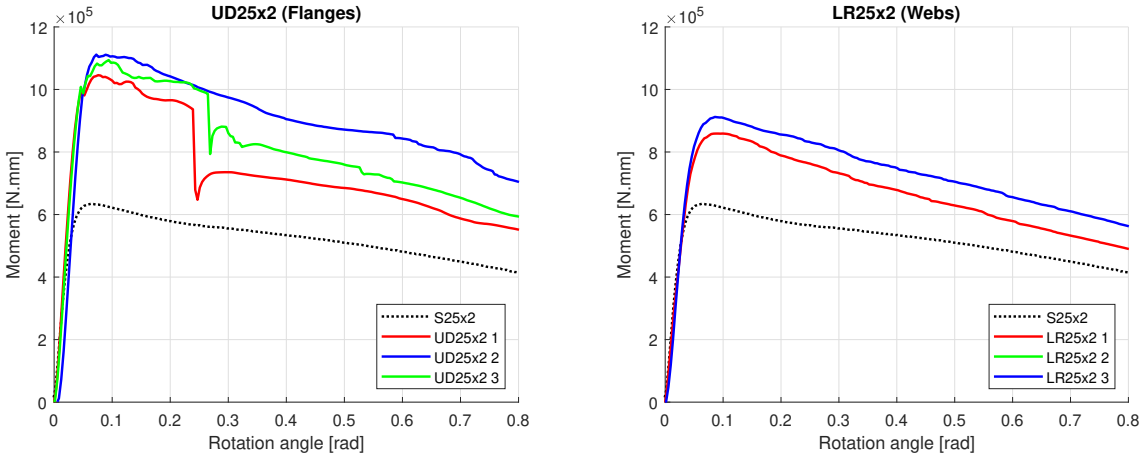

Figure 5.11: Comparison between S25x2, UD25x2 and LR25x2.

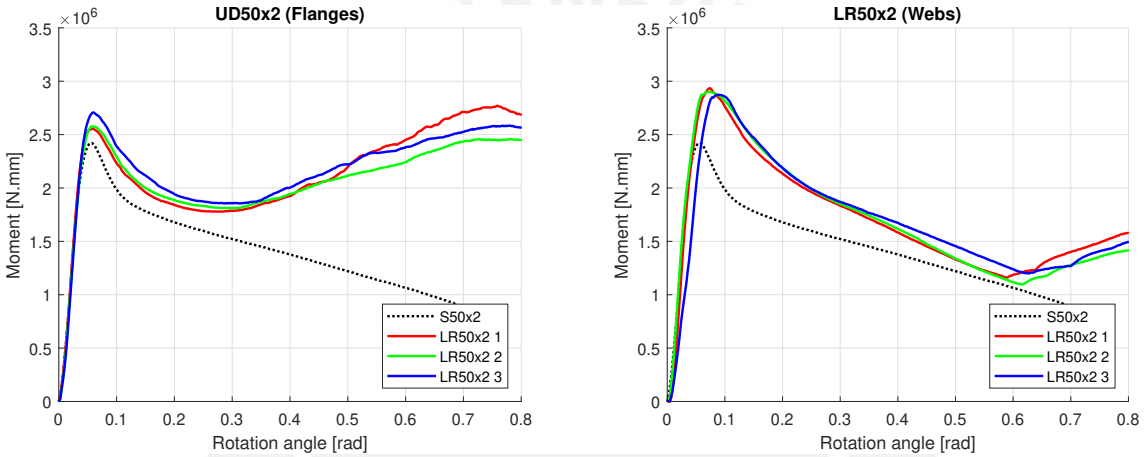

Figure 5.12: Comparison between S50x2, UD50x2 and LR50x2.

Figure 5.13: Mode II failure scenario found with top and bottom reinforcements of UD25x2. This is the most commonly found failure scenario.

Figure 5.14: Composite failure in UD25x2 due to normal bending stress in the lower portion of the collapsed zone in top and bottom reinforcements.

Figure 5.15: Indentation failure in UD50x2 shapes.

type of reinforcement, fracture does not reflect noticeably on the $M - \theta$ curves, as there is no noticeable drop in resistance, as seen in Figs. 5.10, 5.11 and 5.12.

The observation that fracture does not occur immediately after the maximum load is reached and instead occurs progressively, partially contradicts the supposition made by some previous authors (H. C. Kim et al., 2013; S. Y. Kim et al., 2017; Shin et al., 2002): if a composite plate (metal + composite) is under bending load and the composite is under traction, only the steel portion will hold the load, whereas if the plate is under compression, both materials hold the load. It is seen in the experiments, that not all layers of CFRP fracture (when under traction) at the same time. Instead, this fracture is progressive and starts with the upper portion on the outer layers. It is theorized that this apparent contradiction comes from the different mechanical properties of both materials.

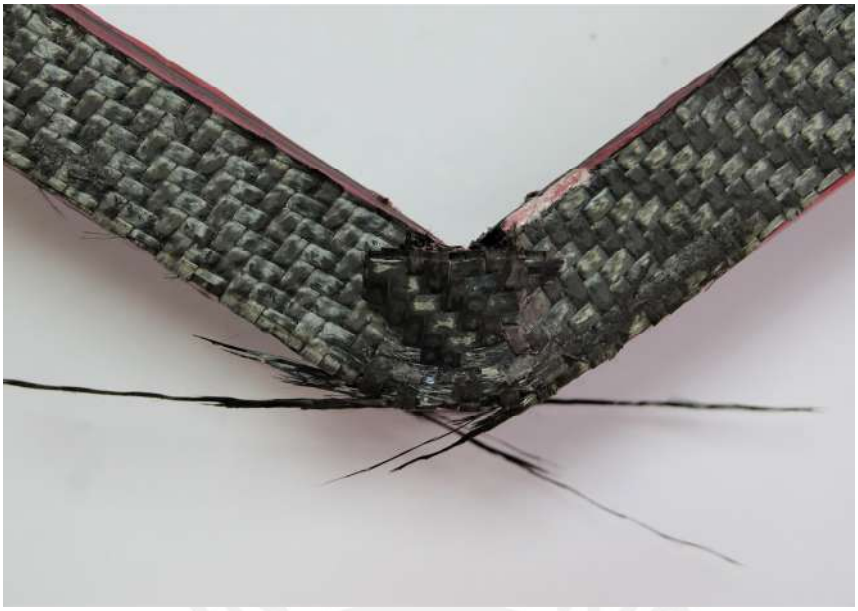

Figure 5.16: Composite failure in the exterior layers of the LR reinforcement.

Figure 5.17: Specimen with LR reinforcement, showing that the inner layers of CFRP are still attached to the steel tube.

Previous authors typically work with aluminum as the base material, which has greater compliance than steel. This leads to larger curvatures and thus, producing the fracture of the reinforcement earlier. Furthermore, in this study, commercial steel shapes are used, which are thicker than those typically used in research. Thicker shapes do not exhibit sharp hinge lines (Lavayen-Farfan et al., 2021; Rincón-Dávila et al., 2022), and the hinge lines show less curvature in the bulge zone; thus requiring larger deformations to fracture the reinforcement. If these hinge lines were to be sharper, then fracture would occur as soon as they appear. The combination of different materials and thicker shapes produces the apparent contradiction with the previously cited works. Another reason for the apparent contradiction comes from the use of different fiber fractions in the composite, fiber directions, and the adhesive used.

Figure 5.18: Collapse zone that forms in LR50x2, note that the fracture grows from the upper part to the bottom.

5.5.3 Comparison

A comparison between both types of reinforcements is an important remark for design choices. The comparison can be done in terms of the maximum moment M_m, the specific energy absorption (SEA), and their corresponding variation with respect to the unreinforced shape. The SEA can be calculated with the area under the $M-\theta$ curve and the total mass of the shape, as seen in Eq. 5.13. For uniformity, $\theta_{end} = 0.6$ rad is chosen for calculations.

$$\text{SEA} = \frac{1}{m_{\text{shape}}} \int_0^{\theta_{end}} M \mathrm{d}\theta \tag{5.13}$$

Special care is taken for the M_m and SEA results for UD50x2, since there are two "peaks" due to the indentation. Results of the "first" peak is considered as M_m, since it apparently occurs only due to bending and the second peak is the result of the indentation, an evidence supporting this supposition is provided in Fig. 5.15, as the indentation is the "last" phenomenon that occurs, leaving the shape of the force applicator on the test specimen.

As depicted in Table 5.3, the increase in maximum moment M_m is evident for all reinforcements. In the case of S25x1.5, both reinforcements produce similar increases in M_m. An ANOVA is performed on these results, and it is revealed that UD25x1.5 and LR25x1.5 produce statistically the same increase in M_m. For S25x2, the M_m increase for UD25x2 is far more denoting than LR25x2, whereas for S50x2, the opposite occurs. It is then theorized that the rise in M_m for each shape is deeply influenced by the ratio t_{st}/b. Smaller ratios of t_{st}/b seem to be better suited for web reinforcement (LR), whereas larger ratios t_{st}/b seem to favor flange reinforcement (UD).

A more objective comparison can be done using the SEA parameter (Eq. 5.13). It can be seen that the smallest shapes (S25x1.5 and S25x2) benefit the most from the reinforcements, as they increase the SEA by up to 45%. In terms of SEA increase, flange (UD) reinforcements seem to favor thicker shapes more. A comparison between the flange and web reinforcements of S50x2 is not possible, as the indentation mode is significant in UD50x2. It can also be seen in Table 5.3 that the largest shapes (S50x2) suffered the least increment in mass, at around 6%, whereas the smallest shape (S25x1.5) suffered the largest mass increment.

Table 5.3: Summary of the experimental results and comparison

ID	M_m 10^6 [N.mm]	Mass [kg]	SEA [J/kg]	M_m variation	Mass variation	SEA variation
S25x1.5	0.4595	0.485	471.16	ref.	ref.	ref.
UD25x1.5	0.7225	0.553	683.73	+57.24%	+13.99%	+45.12%
LR25x1.5	0.6821	0.555	631.35	+48.44%	+14.38%	+34.00%
S25x2	0.6344	0.707	591.37	ref.	ref.	ref.
UD25x2	1.0837	0.785	822.96	+70.83%	+11.09%	+39.16%
LR25x2	0.8856	0.784	702.84	+39.59%	+10.84%	+18.85%
S50x2	2.4220	1.477	619.46	ref.	ref.	ref.
UD50x2	2.6137*	1.563	768.09*	+7.91%*	+5.84%	+23.99%*
LR50x2	2.9038	1.570	694.27	+19.89%	+6.29%	+12.08%

* significant indentation, not to be directly compared.

Furthermore, the increase in both M_m and SEA due to reinforcements puts thinner shapes in the range of values of thicker shapes without reinforcement. For instance, by reinforcing the flanges or webs of S25x1.5, its M_m becomes larger than that of S25x2, which is an important increase in strength without a significant increase in weight. Moreover, the SEA value of the reinforced S25x1.5 and S25x2 becomes larger than that of the S50x2, meaning that they become more capable of absorbing energy than a larger shape.

5.5.4 Theoretical model results

Lastly, the theoretical model proposed in this work is compared to the experimental results, in order to assess its accuracy and with the modified Kecman model for the unreinforced shapes (according to Lavayen-Farfan et al. (2021)) to check the difference between the models. As depicted in Figs. 5.20-5.22, the theoretical model appears to be capable of predicting the experimental results; however, it also has a strong dependency on λ, in other words, the curvature at which the maximum moment M_m occurs. Theoretical results have been calculated with a λ that produces an adequate value of M_m. The only instance where the difference between the theoretical and experimental results is significant, corresponds to UD50x2. However, this significant difference is expected, since the theoretical formulation corresponds to pure bending, whereas the experiment showed significant indentation.

It is found that the most adequate values of λ are in fact in between 2 and 4 for LR reinforcements and between 1 and 2 for UD reinforcements. The specimens with LR reinforcements typically require larger λ values, which means that they endure larger curvatures during the collapse stage. This is most likely a consequence of their stress distribution (recall Fig. 5.5). The stress progressively grows along the reinforcements as the steel shape deforms plastically, thus increasing the curvature required to reach M_m. On the other hand, the specimens with UD reinforcements have the same stress value along its length.

Furthermore, in general, thicker shapes (larger values of t_{st}/b) require larger values of λ, as seen in Fig. 5.19. This means that M_m produce larger curvatures in thicker shapes. Previous research (Lavayen-Farfan et al., 2021) has also found a similar behavior. However, instead of analyzing the curvature at collapse, the angle θ_m was analyzed. It was found that for thin-walled shapes, θ_m is negligible, whereas for the so-called medium-thin-walled shapes θ_m (and the curvature), starts to grow. A similar behavior is shown in

for these reinforced shapes. The main reason for the growth of λ with the t_{st}/b ratio is due to the actual stress distribution that appears in the through-the-thickness direction of the shapes. Before the maximum moment is reached, not all points in the through-the-thickness direction reach the yield strength and tensile strength at the same time. Since M_m is defined by all points reaching these points, thicker shapes require larger curvatures to reach the actual maximum moment.

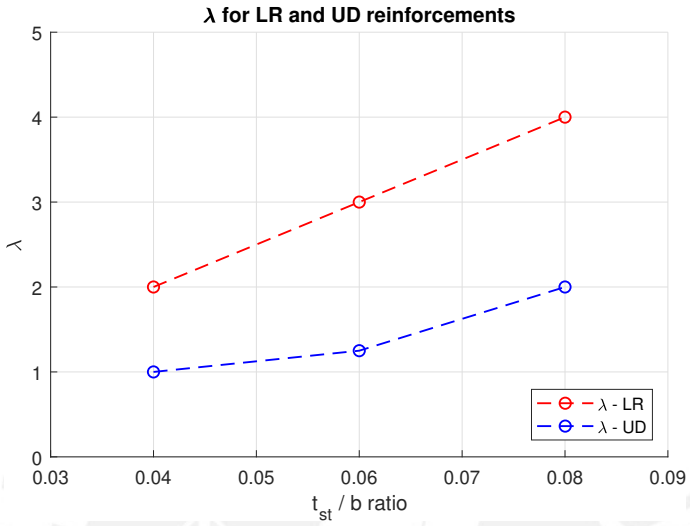

Figure 5.19: Critical curvature ratio λ for different values of t_{st}/b.

By comparing the proposed theoretical model curves (in black) with the theoretical curves for the unreinforced shapes (in magenta), an almost constant offset can be observed between the curves. This offset represents not only the increase in strength and absorbed energy, but it is also the additional stress distribution shown in red in Fig. 5.5 and the reinforcement term in Eq. 5.7.

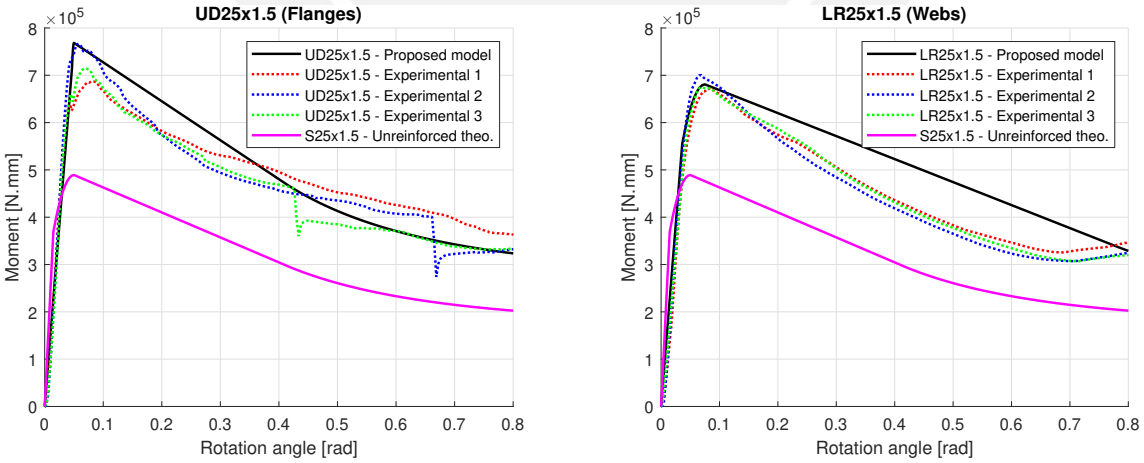

Figure 5.20: Comparison between the experimental and theoretical curves for UD25x1.5 and LR25x1.5. Theoretical results calculated with $\lambda = 1.25$ and $\lambda = 3$ for UD and LR reinforcements, respectively.

5.6 Conclusions

In this study, a theoretical approach is taken to determine the bending strength and bending collapse behavior of partially reinforced CFRP-Steel tubes. The bending strength

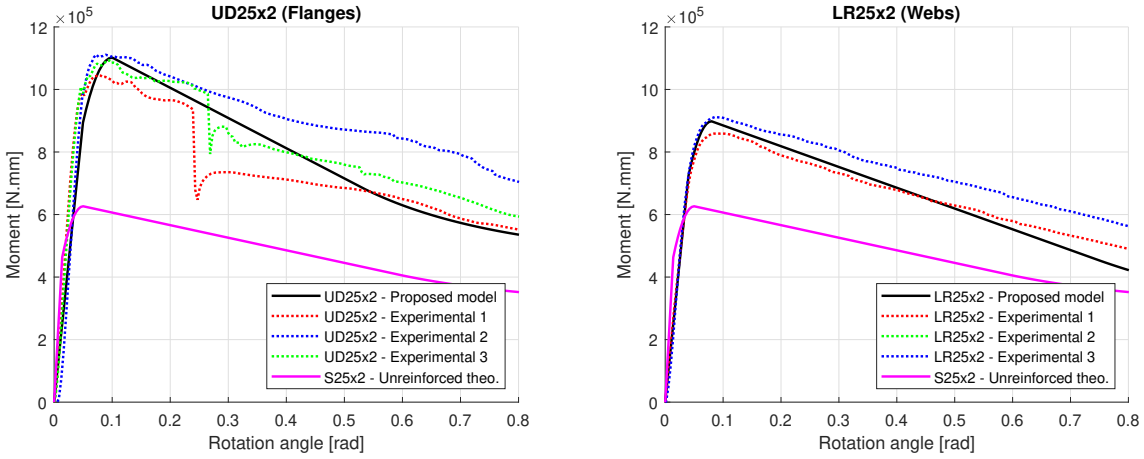

Figure 5.21: Comparison between the experimental and theoretical curves for UD25x2 and LR25x2. Theoretical results calculated with $\lambda = 2$ and $\lambda = 4$ for UD and LR reinforcements, respectively.

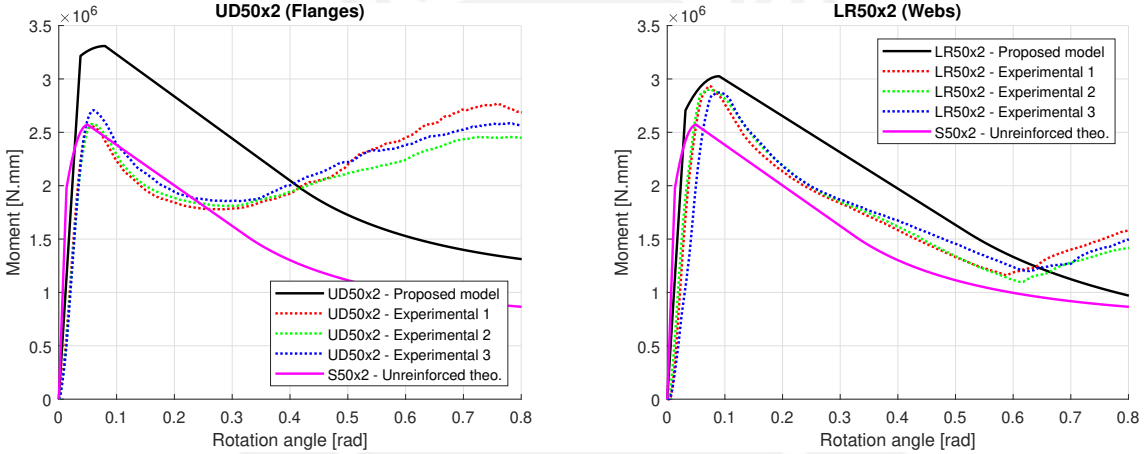

Figure 5.22: Comparison between the experimental and theoretical curves for UD50x2 and LR50x2. Theoretical results calculated with $\lambda = 1$ and $\lambda = 2$ for UD and LR reinforcements, respectively.

is characterized by the maximum moment M_m and the bending collapse behavior can be represented by the moment-angle $M - \theta$ curve, obtained by a modification of Kecman's collapse theoretical model. Two types of reinforcements are used: Reinforcements on the flanges (UD reinforcements) and reinforcements on the webs (LR reinforcements). The following conclusions have been drawn:

- The developed theoretical approach, based on Kecman's collapse model, is able to predict the maximum moment and the bending collapse behavior of partially reinforced CFRP-Steel square tubes. The theoretical results show an adequate agreement with the experimental collapse results obtained using three-point bending tests.
- Both types of proposed reinforcements can significantly increase the maximum moment and enhance the energy absorption capabilities of thin-walled and medium-thin-walled square shapes, without an important weight increment.
- Experiments showed that the failure mode of the LR reinforcements is kept in the vicinity of the plastic hinge (below the force applicator) or the critical zones of a structures, whereas the failure mode of the UD reinforcements is independent of the

span between supports. Thus, the whole length of a tube does not require to be reinforced and only a localized reinforcement is required.

- Since these reinforcements are localized, they do not increase the weight of the structure significantly but do increase the maximum load from 20% up to 70% (depending on the reinforcement) and, more importantly, the SEA by up to 45%. An important finding is that by adding a partial reinforcement, a thin shape can withstand larger loads than a thicker shape of the same dimensions, UD25x1.5 and LR25x1.5 when compared to S25x2. Although 0.5 mm could be seen as a minor increase in dimensions and weight, for a large structure, saving 0.5 mm in thickness can translate into an important weight reduction, since commercial shapes typically have the same thickness in the whole length.

Furthermore, future work and applications of the developed theoretical approach can be summarized as follows:

- The proposed theoretical approach can be used to implement simplified frame models to evaluate the crashworthiness of lightweight structures and require less computation and modeling time, without sacrificing the accuracy when compared to a fully detailed model. This development can significantly accelerate the structural optimization processes of design engineers.

- The present work shows that the use of localized partial reinforcements can enhance structures without a large increase in weight. Thus, these reinforcements can be retrofitted to existing vehicle structures, especially if they do not comply with new standards and regulations.

- It might be counter-intuitive to implement reinforcements on the webs (LR reinforcements), instead that on the flanges for a larger moment of inertia. However, webs are the zones where the most energy can be dissipated, which translates into a considerable increase in strength and absorbed energy when reinforced. This increase, although less than when reinforcing the flanges, is still significant and can be considered as viable alternative for designers of lightweight structures, especially with space constraints.

- Reinforcing existing vehicle structures, installing new and lighter rollover cages and bars in buses, pickup trucks and competition vehicles can be useful, especially now when there are initiatives, such as the goal zero for safe mobility in the European Union, which seek to enhance vehicle safety.

Chapter 6

Development of a conceptual bus model for rollover analysis

The bending collapse models proposed in Chapters 4 and 5,, now validated and implemented, can be used for the analysis of different frame structures. In this thesis, the focus lies on the rollover crashworthiness of a bus. Using a simplified concept model instead of a full detail FEM model offers several advantages: The first advantage is the significantly lesser modeling and simulation times, which open the door for further analyses and the study of new geometries, distributions, etc. Another advantage of low times is the possibility of optimization routines. Since optimization requires the evaluation of a large number of design points, and considering that each design point requires a non-linear analysis, the required optimization time of a full model can rapidly grow and make the optimization unfeasible; thus, a simplified model offers a great alternative for these type of studies (J. Fang et al., 2017).

In this chapter, a conceptual bus rollover model is used to address the crashworthiness of the structure, while keeping the problem size fairly low in terms of number of elements and simulation time. The simplified model consists of a concept model of beam elements, which represent the structural tubes of each component, and non-linear springs that represent the plastic collapse zones of the structure. The plastic collapse zones for a bus structure have been previously identified by various researchers and the UN/ECE 66 (2007). Moreover, authors such as Bai, Meng, Wu, et al. (2019), Bai, Meng, and Zuo (2019), Gui et al. (2018), Li et al. (2021), Park and Yoo (2008), and Weiß (2018) among others, have already demonstrated the effectiveness of using concept modeling to evaluate crashworthiness of several vehicle structures and the accuracy of the method when compared to detailed models made from SOLID or SHELL elements. Furthermore, the models used for the plastic zones have been already validated experimentally in the previous chapters. Thus, in this chapter, only the concept model is used.

Three groups of analyses are performed to compare the effectiveness of the proposed reinforcements (shown in Chapter 5). The first group consists of unreinforced structures with structural tubes of different sizes and thickness. On the other hand, the second group incorporates the proposed LR reinforcements, whereas the third group incorporates the UD reinforcements. Once the analyses are completed, an evaluation, following the specifications of R66 is performed. A scheme for the workflow followed in this chapter is presented in Fig. 6.1.

6.1 Model description

A scheme for the concept model is depicted in Fig. 6.2 and is built in Ansys Classic. The columns, floor, and roof are built using BEAM188 elements. The collapse zones are

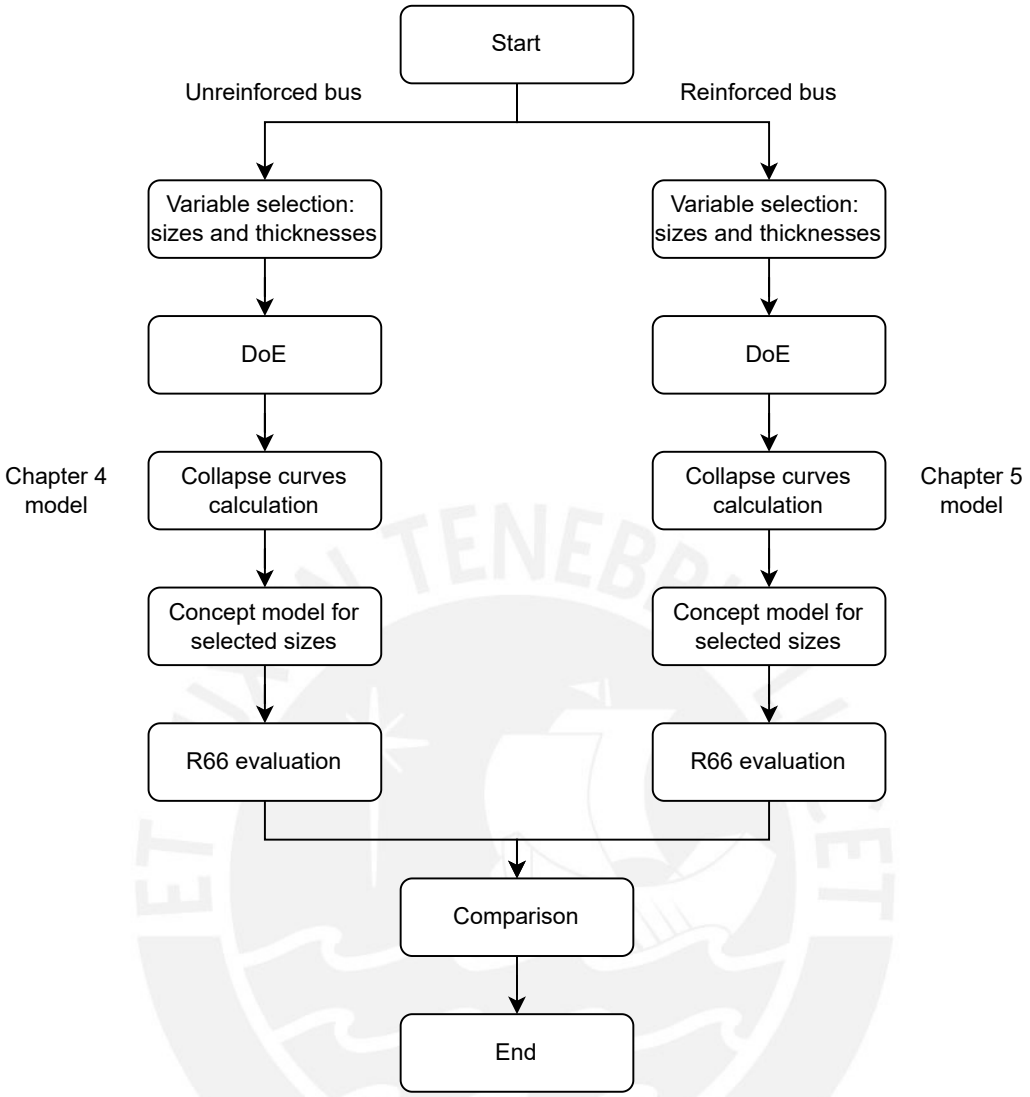

Figure 6.1: Workflow scheme for the current chapter.

modeled using two elements: First, a revolute joint is defined using the MPC164 element, which allows for free rotation in the zones of the plastic hinges. Then, a non-linear spring element COMBIN39 is defined parallel to the revolute joint. The non-linear spring element carries the information of the bending collapse $M - \theta$ curve, using the models developed in previous chapters. Furthermore, the static calculation method found in R66 is used for evaluation. This method has proven to be effective, as several entities use it for homologation of bus super-structures. For this procedure, the load is applied via a rigid surface until the structure invades the residual space. The load plane as well as the residual space are modeled using rigid target TARGET169 elements, and the structure is covered using deformable contact CONTA172 elements.

The resulting FEM model is shown in Fig. 6.3, along with its deformed shape and stress distribution. The stress distribution reveals that the zones near the column-floor and column-roof joints are those with the largest equivalent stresses. Since the point with the largest equivalent stress may not be the same for every case evaluated, all points near the joints are surveyed to obtain the maximum equivalent stress.

The analysis focuses on the crashworthiness of the structural loop. It should be noted that the lower bay of the bus does not contribute much in the crashworthiness, as shown in Chapters 2 and 3 and addressed by multiple researchers. Thus, in order to address

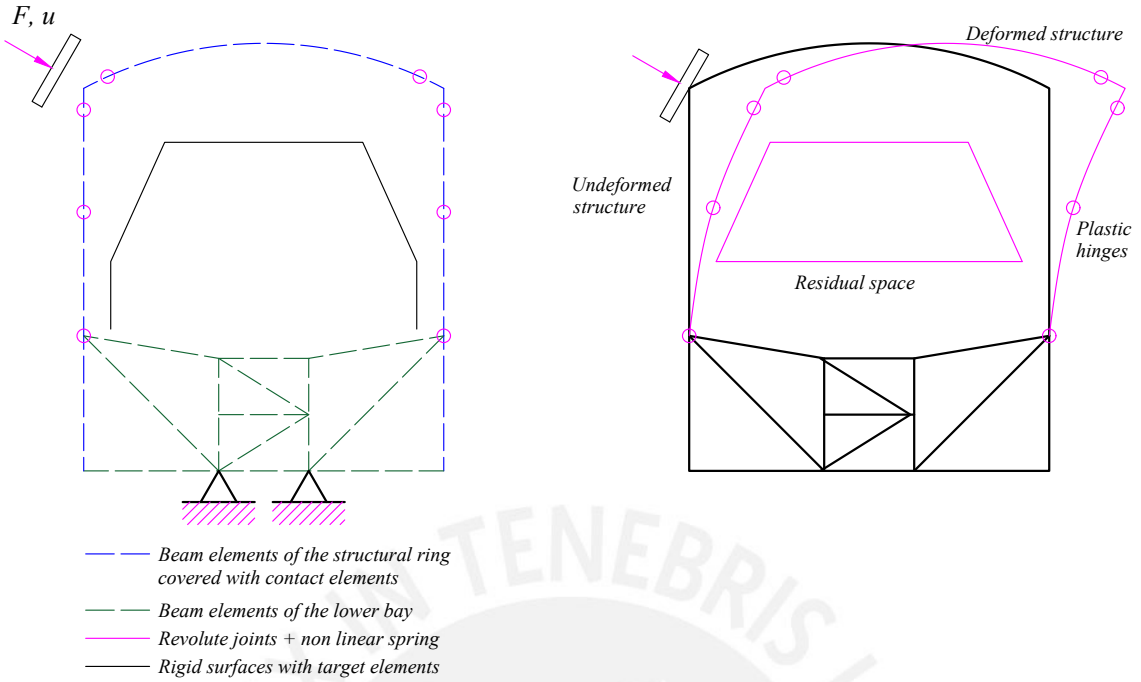

Figure 6.2: Scheme for concept modeling.

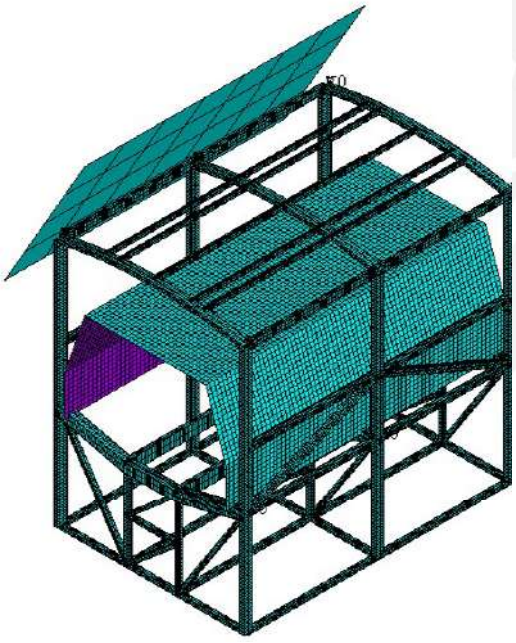

Figure 6.3: Resulting FEM model.

its energy absorption capabilities of the loop itself while reduce the influence of other variables, the loop is "isolated" and studied by itself, as seen in Fig. 6.4. Based on this scheme, a FEM model is also developed, as shown in Fig 6.5.

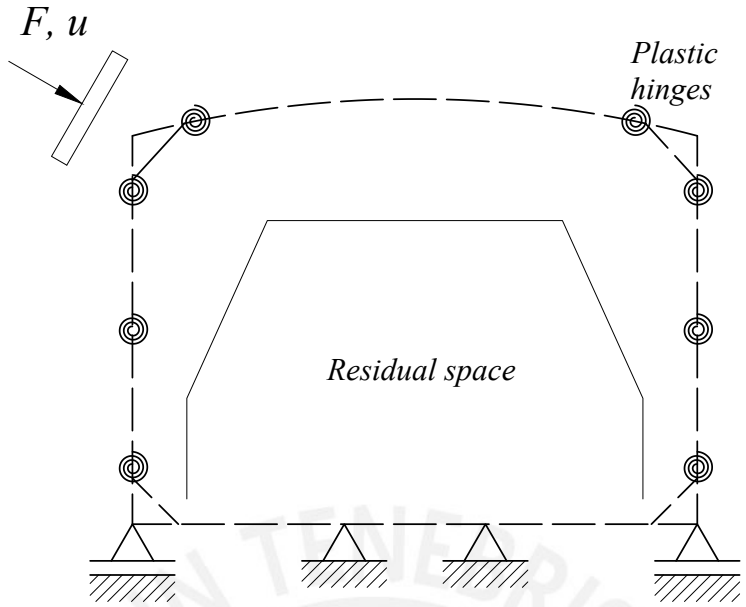

Figure 6.4: Concept model for a structural loop. Note that the non-linear springs are located in the plastic hinge zones.

6.2 R66 evaluation

6.2.1 Energy calculation

The UN/ECE 66 (2007) states that the absorbed energy during the rollover must be larger than a minimum energy value, based on the rollover test. This magnitude can be calculated using the applied force F and displacement of the rigid wall u, as seen in Eq. 6.1 as follows:

$$E_{abs} = \int_0^{u_{max}} \vec{F} \cdot d\vec{u} \tag{6.1}$$

Where u_{max} occurs when the structure touches the residual space. The initial position of the rigid wall (where the force is applied) is set to 100 mm away from the structure, and must travel an average of 400 mm before u_{max} is reached, thus, the total distance traveled by the rigid wall is always 500 mm.

6.2.2 Variable selection

Since most of the energy from an impact is dissipated in the plastic hinges, the dimensions of width, height and thickness of the structural shapes of the columns, roof and floor are used as design variables to explore different geometry variations. The design point x is thus defined:

$$x = (b_{col}, a_{col}, t_{col}, b_{roof}, a_{roof}, t_{roof}, b_{floor}, a_{floor}, t_{floor}) \tag{6.2}$$

It should be noted that not all combinations are commercially available, however, they are still included for the sake of mathematical continuity. The rest of the structure is kept with the same dimensions for all design points, since the influence of only the structural rings is evaluated. The reinforcements are considered to be either the UD or LR reinforcements from the previous chapters, with the same adhesive type and thickness. Furthermore, the values of λ taken from Fig. 5.19 are used.

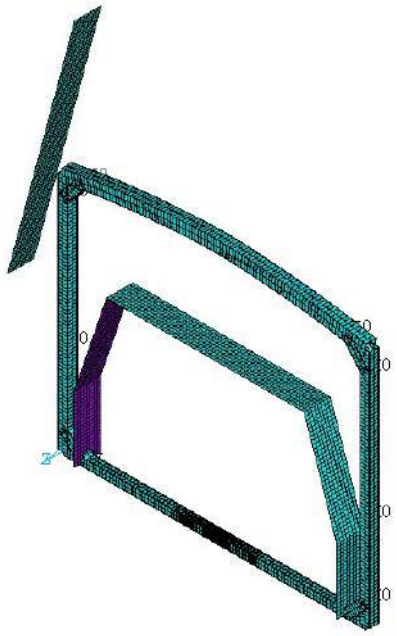

Figure 6.5: Concept model for a representative structural loop.

6.2.3 Design of experiments

Once the desired variables and their values are defined, a Latin Hypercube sampling (LHS) is performed. The LHS consists on the six aforementioned variables in 10 levels. The Matlab command `lhsdesign` is used to create the design of experiments and produces the design points shown in Table 6.1. Each design point consists of a different structural loop, with the identifying number shown in the first column of Table 6.1. The analysis also considers that both the column and roof have the same tube sizes. This is usually a design constraint. The tubes used for the floor are significantly larger, since the lower portion of the structure has a significantly higher stiffness than the structural loop, thus a rectangular tube of 80x40x3 mm is used for all cases. It should be noted, that as long as the floor tube is large enough, its influence on the crashworthiness of the loop is negligible.

Table 6.1: Design points used for DoE, sizes in mm.

ID	b_{col}	a_{col}	t_{col}	b_{roof}	a_{roof}	t_{roof}	b_{floor}	a_{floor}	t_{floor}
1	62.5	32.5	2.6	62.5	32.5	2.6	80	40	3
2	52.5	72.5	1.6	52.5	72.5	1.6	80	40	3
3	32.5	77.5	3.9	32.5	77.5	3.9	80	40	3
4	77.5	57.5	3.8	77.5	57.5	3.8	80	40	3
5	57.5	62.5	3.1	57.5	62.5	3.1	80	40	3
6	37.5	37.5	3.4	37.5	37.5	3.4	80	40	3
7	47.5	42.5	2.9	47.5	42.5	2.9	80	40	3
8	42.5	52.5	2.1	42.5	52.5	2.1	80	40	3
9	67.5	47.5	2.4	67.5	47.5	2.4	80	40	3
10	72.5	67.5	1.9	72.5	67.5	1.9	80	40	3

The structural loops in Table 6.1 are also reinforced with localized LR and UD reinforcements (see Fig. 3.14). Since the reinforcements are only applied in the vicinity of a

plastic zone, the only difference in the FEM model lies on the non-linear spring.

The following output variables are calculated for each design point previously defined:

- Energy absorbed E_{abs}: obtained as the area under the $F - u$ curve, obtained from the force and displacement of the rigid surface, as specified in Eq. 6.1.
- The maximum stress is surveyed from points in the vicinity of the collapse areas, a total of 8 points are considered and the bending stress calculated at these locations. The maximum stress of the structure is taken from these points. This value also serves to prevent collapse in other zones.

6.3 Results and discussion

The resulting deformed shape (Fig. 6.6) shows that most of the deformation occurs in the plastic hinges as predicted by various formerly mentioned authors and the Regulation 66 itself. Furthermore, the plastic hinge has the same deformed shape as the experimental test, which becomes evident by comparing Fig. 6.6 with the experiments shown in Chapter 3, more precisely in Figs. 3.6 - 3.9.

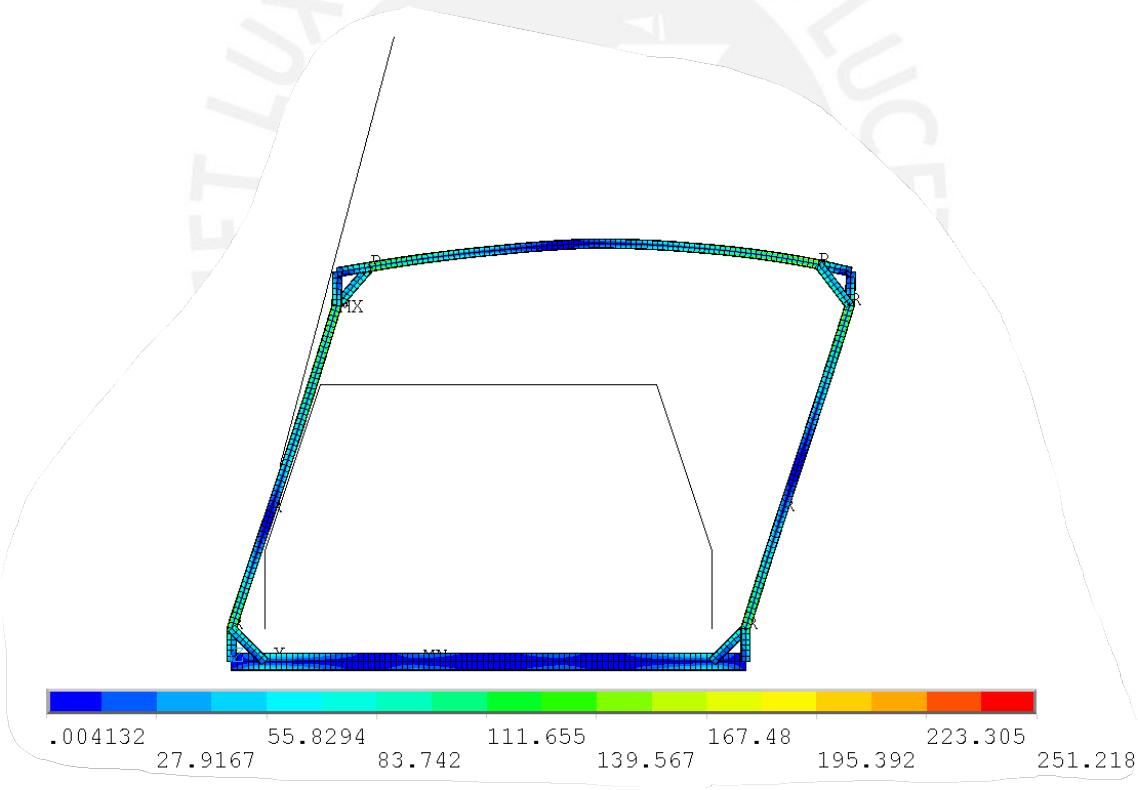

Figure 6.6: Stress field on the structural loop as it comes into contact with the residual space.

The resulting force-displacement curves, obtained in the rigid wall, are shown in Fig. 6.7, where the unreinforced loops (black) are compared with the loops with localized UD (blue) and LR (red) reinforcements. Each graph corresponds to the sizes in Table 6.1. It is readily apparent that the reinforcements provide an increase in the maximum load that the bus can endure. A comparison of the maximum loads and absorbed energy can be seen in Tables 6.2 and 6.3. When the unreinforced structural loop deforms, the force-displacement curve reaches a plateau with a fairly constant value (black curves in Fig. 6.7). In all cases,

both types of reinforcements improve this behavior, by increasing the slope of the force-displacement curve (red and blue curves) and thus increasing also the absorbed energy. There is however an unforeseen effect, which is an apparent loss in stiffness during the elastic portion of the test. It has been discussed in Chapter 4 that the calculation of θ_m relies heavily on the actual mechanical properties of the steel tubes used. If the theoretical values are used, a larger value of θ_m occurs, thus less stiffness is obtained. This means that more testing and/or numerical simulations are required to obtain a better relationship for θ_m. This unforeseen discrepancy also explains the apparent loss in absorbed energy seen in some cases in Table 6.3. It can also be argued that by increasing the u_{max}, the loss in absorbed energy may be avoided; however, larger u_{max} values would mean intrusion into the residual space and possible injury or fatalities for the passengers.

Moreover, the thinner shapes benefit the most from either type of reinforcements, as evidenced by loops ID 2, 8, 9 and 10. Whereas the increase in crashworthiness is not that significant for thicker shapes. This fact confirms the findings of Chapter 5 from another point of view. A structural loop with thin-walled shapes can benefit tremendously by adding the partial CFRP reinforcements. Additionally, if the tube has a larger thickness than the reinforcement, then the benefit is not as large, as evidenced by loops ID 3, 4 and 6.

Table 6.2: Summary of the results: absolute values.

ID	No reinf.		UD reinf.		LR reinf.	
	F_{max} kN	E_{abs} kJ	F_{max} kN	E_{abs} kJ	F_{max} kN	E_{abs} kJ
1	7.31	2.52	8.69	2.59	8.68	2.58
2	4.58	1.41	7.35	2.32	5.85	1.89
3	7.28	2.39	7.91	2.39	7.90	2.38
4	1.93	6.87	2.29	6.99	2.29	6.95
5	9.93	3.49	13.56	4.07	12.8	4.00
6	4.76	1.49	5.07	1.45	5.06	1.44
7	5.93	1.96	7.08	2.08	7.07	2.07
8	3.86	1.29	5.37	1.60	5.00	1.56
9	8.13	2.83	11.29	3.43	10.44	3.34
10	7.59	2.39	11.04	3.71	9.68	3.16

Furthermore, it should also be noted that in all simulations, the maximum equivalent stress did not surpass the critical stress for buckling. In most cases, the stress levels remained below 300 MPa, slightly above the nominal yield stress of steel S275 considered. In some cases, the equivalent stress levels reached values as high as 400 MPa, however this only occurred when the structure came into contact with the residual space. This data points were not considered during the analyses, since they occurred with wall displacements larger than 500 mm.

6.4 Conclusions

In this chapter, a concept model for the rollover analysis of a bus is developed, based on the bending collapse models proposed in Chapters 4 and 5. The concept model consist of a frame that represents one of the several structural loops of the super-structure of a bus, which is where most the energy dissipation occurs. Bending collapse has been previously identified as the energy absorption mechanism and is included in the concept model by non-linear springs with the corresponding constitutive law. Several variations of sizes and

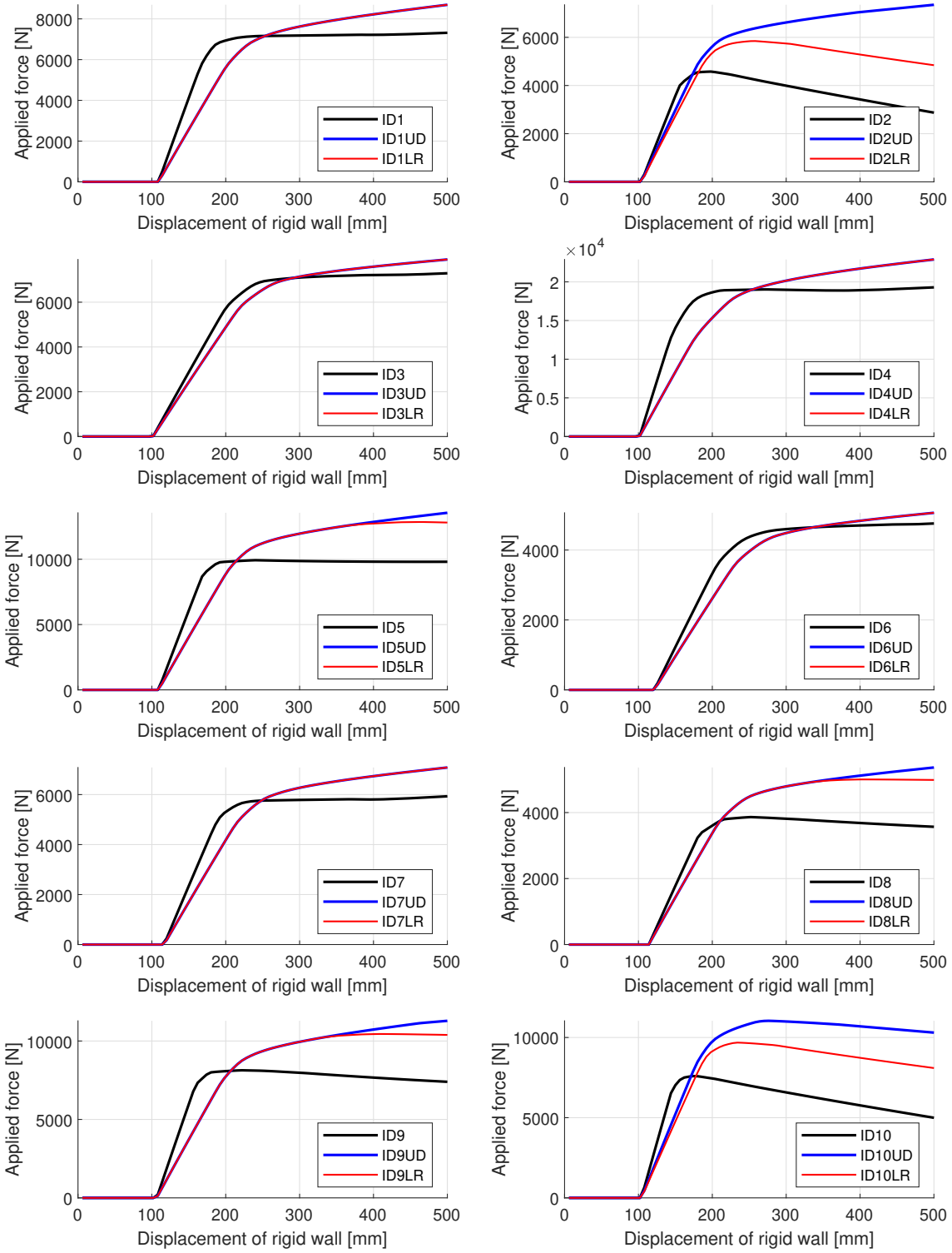

Figure 6.7: Applied force - displacement of the rigid wall for the R66 calculation of the structural loops. Each graph corresponds to the structural loops detailed in Table 6.1. Black lines: unreinforced structural loop, blue lines: structure with UD reinforcements, red lines: structure with LR reinforcements.

thickness have been evaluated: first with unreinforced shapes, and then with the two types of reinforcements (LR and UD) considering CFRP reinforcements of 2.5 mm of thickness.

Although this part of the thesis has not been directly validated by experiments. The similarity of the deformed shapes with those obtained during tests of structural nodes and

Table 6.3: Summary of the results: variations using the unreinforced loops as reference.

ID	UD reinf.		LR reinf.	
	F_{max} %	E_{abs} %	F_{max} %	E_{abs} %
1	+18.9	+2.8	+18.7	2.4
2	+60.5	+64.5	+27.7	34.0
3	+8.7	+0.0	+8.5	-0.4
4	+18.7	+1.7	+18.7	1.2
5	+36.6	+16.6	+28.9	14.6
6	+6.5	-2.7	+6.3	-3.4
7	+19.4	+6.1	+19.2	5.6
8	+39.1	+24.0	+29.5	20.9
9	+38.9	+21.2	+28.4	18.0
10	+45.5	+55.2	+27.5	32.2

previous simulations (in Chapter 3), as well as the experimentally-validated models, proves the validity of the obtained results This comparison can be seen in Fig. 6.8. It can be concluded that the concept model correctly identifies the location of the plastic zone, as it is the zone with the largest strain. The local effects and stress distributions of the collapse zone cannot be captured by the concept model, however, its influence is considered inside the non-linear spring. In future developments, the results could be validated with a real life rollover test.

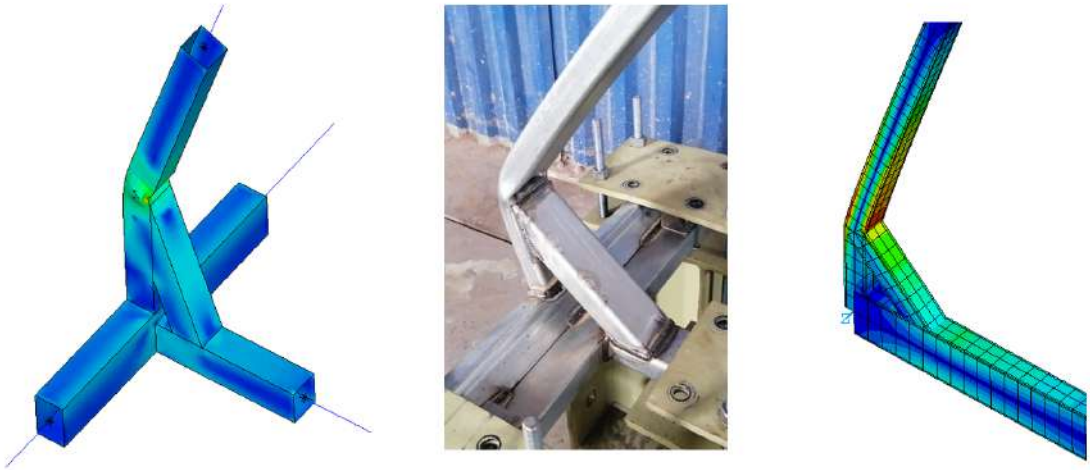

Figure 6.8: Comparison between a) detailed FEM results using SHELL elements, b) experimental bending collapse of a structural node, c) concept model using the proposed collapse models.

All of the structural loops benefited from the use of localized CFRP reinforcements. The UD reinforcements proved to have a larger influence on the structures, since they provide a larger moment of inertia. This result agrees with the findings of the previous chapter. However, the LR reinforcements still provide a non-negligible improvement. Both of these reinforcements can be used to reinforce existing structures and for new designs. When comparing structures with tubes of similar sizes, it can also be inferred that lower

dimensions with localized reinforcements can provide similar levels of crashworthiness than larger sizes without reinforcements.

Finally, further developments include metamodels and optimization based on the presented results. The developed concept model can also be used for other bus shapes and geometries in combination with the proposed bending collapse theoretical models. The resulting models can be used to accelerate the early design and decision making process in bus manufacturing companies, and can be translated with ease to other fields.

Chapter 7

Conclusions and future work

7.1 Conclusions

The research aimed to study and develop theoretical models to predict the effect of multimaterial steel-CFRP shapes on the strength and stiffness of a bus super-structure to enhance its rollover crashworthiness. The estimation of the rollover crashworthiness is performed following the specifications of the rollover test in UN/ECE 66 (2007). The research showed two important results: First, the proposed models can adequately and accurately predict the bending collapse behavior of steel and steel-CFRP shapes. Second, the introduction of localized reinforcements made from CFRP increased the maximum bending collapse load and the energy absorbed during the collapse process. In the automotive industry, a development as such is of great importance, since helps to improve the safety measures of a vehicle without a significant increase in weight.

During the rollover test, the column-floor and column-roof joints are susceptible to bending collapse failure. Two parameters are of great importance to characterize this phenomenon: the maximum bending collapse moment and the energy absorbed during the collapse process (extracted from a moment-angle curve). In steel-only structures, the existing theory (by Kecman) is not able to characterize the moment-angle curve for several commercially rectangular hollow shapes, which generally have a greater thickness than those used in past literature. Thus, a modification to the theory has been proposed to include shapes with larger thickness. The modification has been validated through experiments and numerical simulations, and overall has a better accuracy for the so-called medium-thin-walled shapes. As for the reinforced shapes, no method for calculating the maximum moment has been found. In chapter 5, a theoretical approach has been taken to determine this parameter, based on experimental data. The tests have also shown that by adding the CFRP reinforcements provide a significant increase in the maximum moment and the specific energy absorbed.

Finally, a concept model of the bus structure is built and tested. The concept model consists of beam elements for the structural elements and non-linear springs in the column-floor and column-roof joints. The non-linear springs have the characteristic moment-angle curve obtained using the aforementioned proposed theoretical models. The calculations follow the specifications found on UN/ECE 66 (2007) and show that the inclusion of the reinforcements provide a substantial increase in rollover crashworthiness without an significant weight increase, which translates into higher chances of survival for the occupants in case of an accident. The simplicity of the reinforcements means that they can be retrofitted in existing structures that may not initially pass the rollover test. Alternatively, new structure designs may use lower thickness in the structural shapes and compensate this reduction with localized reinforcements in critical areas. This change would in turn result in lighter structures and with acceptable level of crashworthiness and capable of

successfully passing the rollover test. Lighter and stronger structures provide not only reduced manufacturing costs but also reduced fuel consumption and carbon emissions which are mandatory in the current age. More importantly, this improvement can be translated into a larger survivability rate for passengers in case of a rollover accident.

7.2 Future work

The current trend in the lightweight design and the automotive industry is the use of multimaterial structures. Although the developments in this thesis are focused to bus super-structures, they could be extrapolated to many other structures prone to bending collapse and may benefit from composite reinforcements. The models and procedures obtained in this thesis can be applied to: rollover safety cages for heavy machinery and mining equipment, crashworthiness studies for competition vehicles, bending collapse of the structure of wind turbine blades, etc. It should be noted that these kind of studies always require the fulfillment of the corresponding regulations and standards.

Furthermore, the proposed models for bending collapse do not mark the end of the research in the bending collapse phenomenon for thin-walled structures. The development of this thesis allowed the exploration of localized bending collapse models that still require research. Even though most of the limitations of Kecman's theory have been overcome, the model itself is not perfect. The prediction of many parameters still relies heavily on empirical relationships and does not include the effect of the fillet radii, which requires attention in future research. Thus, another topic that follows is the study of the influence of variability of the nominal values for each dimension on the overall bending collapse behavior. Simultaneously, the yield and tensile strengths of the steel have a significant influence on the maximum moment and collapse behavior; however, their values can change even for two specimens of the same dimensions and base material most likely due to manufacturing process. The influence of such parameters can be studied, for example, using polynomial chaos expansion. Furthermore, due to the immense complexity for finding a closed-form solution to describe the collapse phenomenon including all geometry parameters and material models, it is worth looking at alternative approaches. One of the most promising alternatives is the development of an artificial neural network that predicts the parameters of a general collapse curve. In this manner, the calculation of the collapse curve and maximum moment can be performed with ease; however, this approach requires a large number of experimental data. Finally, during the development of this thesis relied upon the three-point bending test, as it produces results similar to those of by the cantilever test by Kecman. Current research, still in development by the author, aims to obtain the exact relationship between the two tests and determine under which conditions both tests are equivalent.

Bibliography

Abramowicz, W., & Jones, N. (1997). Transition from initial global bending to progressive buckling of tubes loaded statically and dynamically. *International Journal of Impact Engineering*, *19*(5-6), 415–437. https://doi.org/10.1016/s0734-743x(96)00052-8

Adams, R. D. (2017). 50 Years in Carbon Fibre, 60 Years in Composites. In P. W. R. Beaumont, C. Soutis, & A. Hodzic (Eds.), *The structural integrity of carbon fiber composites: Fifty years of progress and achievement of the science, development, and applications* (pp. 3–28). Springer International Publishing. https://doi.org/10.1007/978-3-319-46120-5

Allman, D. J. (1977). A theory for elastic stresses in adhesive bonded lap joints. *The Quarterly Journal of Mechanics and Applied Mathematics*, *30*(4), 415–436. https://doi.org/10.1093/qjmam/30.4.415

Amouzgar, K., & Strömberg, N. (2017). Radial basis functions as surrogate models with a priori bias in comparison with a posteriori bias. *Structural and Multidisciplinary Optimization*, *55*(4), 1453–1469. https://doi.org/10.1007/s00158-016-1569-0

ANSYS Inc. (2021a). ANSYS as a Server Example : MATLAB Setup.

ANSYS Inc. (2021b). Mechanical APDL as a Server User's Guide.

Araújo, H. A., Machado, J. J., Marques, E. A., & da Silva, L. F. (2017). Dynamic behaviour of composite adhesive joints for the automotive industry. *Composite Structures*, *171*, 549–561. https://doi.org/10.1016/j.compstruct.2017.03.071

ASTM A500. (2018). A500/A500M-18 Standard Specification for Cold-Formed Welded and Seamless Carbon Steel Structural Tubing in Rounds and Shapes. https://doi.org/10.1520/A0500_A0500M-18

Ataş, A., & Soutis, C. (2017). Damage and Failure Analysis of Bolted Joints in Composite Laminates. In P. W. R. Beaumont, C. Soutis, & A. Hodzic (Eds.), *The structural integrity of carbon fiber composites: Fifty years of progress and achievement of the science, development, and applications* (pp. 591–644). Springer. https://doi.org/10.1007/978-3-319-46120-5

Bai, J., Meng, G., Wu, H., & Zuo, W. (2019). Bending collapse of dual rectangle thin-walled tubes for conceptual design. *Thin-Walled Structures*, *135*(August 2018), 185–195. https://doi.org/10.1016/j.tws.2018.11.014

Bai, J., Meng, G., & Zuo, W. (2019). Rollover crashworthiness analysis and optimization of bus frame for conceptual design. *Journal of Mechanical Science and Technology*, *33*(7), 3363–3373. https://doi.org/10.1007/s12206-019-0631-4

Bambach, M. R. (2014). Thin-Walled Structures Fibre composite strengthening of thin steel passenger vehicle roof structures. *Thin Walled Structures*, *74*, 1–11. https://doi.org/10.1016/j.tws.2013.09.018

Barenblatt, G. I. (1959). The formation of equilibrium cracks during brittle fracture. General ideas and hypotheses. Axially-symmetric cracks. *Journal of Applied Mathematics and Mechanics*, *23*(5), 1273–1282. https://doi.org/10.1016/0021-8928(59)90130-3

Barenblatt, G. I. (1962). The Mathematical Theory of Equilibrium Cracks in Brittle Fracture. *Advances in Applied Mechanics*, *7*, 55–129. https://doi.org/10.1016/S0065-2156(08)70121-2

Brown, J. C., & Tidbury, G. H. (1983). An investigation of the collapse of thin walled rectangular beams in biaxial bending. *International Journal of Mechanical Sciences*, *25*(9), 733–746.

Budhe, S., Banea, M. D., de Barros, S., & Da Silva, L. F. (2017). An updated review of adhesively bonded joints in composite materials. *International Journal of Adhesion and Adhesives*, *72*(October 2016), 30–42. https://doi.org/10.1016/j.ijadhadh.2016.10.010

Castejon, L., Miravete, A., & Cuartero, J. (2006). Composite bus rollover simulation and testing. *International Journal of Heavy Vehicle Systems*, *13*(4), 281. https://doi.org/10.1504/IJHVS.2006.010584

Chen, S., Chng, E. S., & Alkadhimi, K. (1996). Regularized orthogonal least squares algorithm for constructing radial basis function networks. *International Journal of Control*, *64*(5), 829–837. https://doi.org/10.1080/00207179608921659

Chen, X. (2017). Experimental investigation on structural collapse of a large composite wind turbine blade under combined bending and torsion. *Composite Structures*, *160*, 435–445. https://doi.org/10.1016/j.compstruct.2016.10.086

Christensen, J., & Bastien, C. (2016a). Applications of Concept Nonlinear Optimization. In *Nonlinear optimization of vehicle safety structures* (pp. 383–414). https://doi.org/10.1016/b978-0-12-417297-5.00009-2

Christensen, J., & Bastien, C. (2016b). Introduction to Structural Optimization and Its Potential for Development of Vehicle Safety Structures. In *Nonlinear optimization of vehicle safety structures* (pp. 169–207). Elsevier. https://doi.org/10.1016/B978-0-12-417297-5.00004-3

Chu, D., Li, Z., Wang, J., Wu, C., & Hu, Z. (2018). Rollover speed prediction on curves for heavy vehicles using mobile smartphone. *Measurement: Journal of the International Measurement Confederation*, *130*, 404–411. https://doi.org/10.1016/j.measurement.2018.07.054

Chuang, C. H., Yang, R. J., Li, G., Mallela, K., & Pothuraju, P. (2008). Multidisciplinary design optimization on vehicle tailor rolled blank design. *Structural and Multidisciplinary Optimization*, *35*(6), 551–560. https://doi.org/10.1007/s00158-007-0152-0

Da Silva, L. F., & Campilho, R. D. S. G. (2012). *Advances in Numerical Modelling of Adhesive Joints* (1st ed.). Springer.

de Bruyne, N. (1944). The Strength of Glued Joints. *Aircraft Engineering and Aerospace Technology*, *16*(4), 115–118. https://doi.org/10.1108/eb031117

del Castillo, E. (2007). *Process Optimization - A Statistical approach* (1st ed.). Springer.

Dhaliwal, G. S., & Newaz, G. M. (2020). Experimental and numerical investigation of flexural behavior of hat sectioned aluminum/carbon fiber reinforced mixed material composite beam. *Composites Part B: Engineering*, *182*, 107642. https://doi.org/10.1016/j.compositesb.2019.107642

Doke, P., Fard, M., & Jazar, R. (2012). Advanced Concept Modelling Method for Automotive Structural Optimization. In *Sustainable automotive technologies 2012* (pp. 91–96). Springer Berlin Heidelberg. https://doi.org/10.1007/978-3-642-24145-1_13

Du, Z., Duan, L., Cheng, A., Xu, Z., & Zhang, G. (2019). Theoretical prediction and crashworthiness optimization of thin-walled structures with single-box multi-cell section under three-point bending loading. *International Journal of Mechanical Sciences*, *157-158*(May), 703–714. https://doi.org/10.1016/j.ijmecsci.2019.05.013

Dudgale, D. (1960). Yielding of steel sheets containing slits. *Journal of the Mechanics and Physics of Solids*, *8*(2), 100–104. https://doi.org/10.1016/0022-5096(60)90013-2

Eksi, S., & Genel, K. (2013). Bending response of hybrid composite tubular beams. *Thin-Walled Structures*, *73*, 329–336. https://doi.org/10.1016/j.tws.2013.09.001

Fang, H., Rais-Rohani, M., Liu, Z., & Horstemeyer, M. F. (2005). A comparative study of metamodeling methods for multiobjective crashworthiness optimization. *Computers and Structures*, *83*(25-26), 2121–2136. https://doi.org/10.1016/j.compstruc.2005.02.025

Fang, J., Sun, G., Qiu, N., Kim, N. H., & Li, Q. (2017). On design optimization for structural crashworthiness and its state of the art. *Structural and Multidisciplinary Optimization*, *55*(3), 1091–1119. https://doi.org/10.1007/s00158-016-1579-y

Fard, M., & Liu, Z. (2015). Automotive Body Concept Modeling Method for the NVH Performance Optimization. *SAE Technical Paper Series*, *1*(March), 1–5. https://doi.org/10.4271/2015-01-0012

Federation Internationale De l' Automobile. (2018). Reglement D ' Homologation 2018 Pour Armatures De Securite. https://www.rfeda.es/documents/20185/776060/RH+ES+FIA

Florian, A. (1992). An efficient sampling scheme: Updated Latin Hypercube Sampling. *Probabilistic Engineering Mechanics*, *7*(2), 123–130. https://doi.org/10.1016/0266-8920(92)90015-A

Fragassa, C., Pavlovic, A., & Minak, G. (2020). On the structural behaviour of a CFRP safety cage in a solar powered electric vehicle. *Composite Structures*, *252*(July), 112698. https://doi.org/10.1016/j.compstruct.2020.112698

Friedrich, H. E. (2017). *Leichtbau in der Fahrzeugtechnik* (2nd ed.). Springer. https://doi.org/10.1007/978-3-658-12295-9

Friedrich, K., & Almajid, A. A. (2013). Manufacturing aspects of advanced polymer composites for automotive applications. *Applied Composite Materials*, *20*(2), 107–128. https://doi.org/10.1007/s10443-012-9258-7

Galvez, P., Quesada, A., Martinez, M. A., Abenojar, J., Boada, M. J. L., & Diaz, V. (2017). Study of the behaviour of adhesive joints of steel with CFRP for its application in bus structures. *Composites Part B: Engineering*, *129*, 41–46. https://doi.org/10.1016/j.compositesb.2017.07.018

Gepner, B., Bojanowski, C., Kwasniewski, L., & Wekezer, J. (2014). Effectiveness of ECE R66 and FMVSS 220 standards in rollover crashworthiness assessment of para-transit buses. *International Journal of Automotive Technology*, *15*(4), 581–591. https://doi.org/10.1007/s12239-014-0061-3

Gillespie, T. D. (1992). *Fundamentals of vehicle dynamics*. SAE.

Gliszczyński, A., & Czechowski, L. (2017). Collapse of channel section composite profile subjected to bending. Part I: Numerical investigations. *Composite Structures*, *178*, 383–394. https://doi.org/10.1016/j.compstruct.2017.07.033

Goland, M., & Reissner, E. (1944). The stresses in cemented lap joints. *Journal of Applied Mechanics*, *11*, 17–27.

González, C., Vilatela, J. J., Molina-Aldareguía, J. M., Lopes, C. S., & LLorca, J. (2017). Structural composites for multifunctional applications: Current challenges and future trends. *Progress in Materials Science*, *89*, 194–251. https://doi.org/10.1016/j.pmatsci.2017.04.005

Gui, C., Bai, J., & Zuo, W. (2018). Simplified crashworthiness method of automotive frame for conceptual design. *Thin-Walled Structures*, *131*(July), 324–335. https://doi.org/10.1016/j.tws.2018.07.005

Guyan, R. J. (1965). Reduction of stiffness and mass matrices. *AIAA Journal*, *3*(2), 380–380. https://doi.org/10.2514/3.2874

Hamza, K., & Saitou, K. (2003). Design Optimization of Vehicle Structures for Crashworthiness via Equivalent Mechanism Approximations. *Journal of Mechanical Design*, *127*(3). https://doi.org/10.1299/jsmedsd.2003.13.309

Hardy, R. L. (1971). Multiquadric equations of topography and other irregular surfaces. *Journal of Geophysical Research*, *76*(8), 1905–1915. https://doi.org/10.1029/JB076i008p01905

Hashemi, S. M., Waltona, A. C., & Kayvantash, K. (2009). Strength of super-structure UN-ECE R66 rollover approval of coaches based on thin-walled framework structures. *International Journal of Vehicle Structures and Systems*, *1*(4), 78–84. https://doi.org/10.4273/ijvss.1.4.04

Henning, F., Kärger, L., Dörr, D., Schirmaier, F. J., Seuffert, J., & Bernath, A. (2019). Fast processing and continuous simulation of automotive structural composite components. *Composites Science and Technology*, *171*(September 2017), 261–279. https://doi.org/10.1016/j.compscitech.2018.12.007

Heshmati, M., Haghani, R., Al-Emrani, M., & André, A. (2018). On the strength prediction of adhesively bonded FRP-steel joints using cohesive zone modelling. *Theoretical and Applied Fracture Mechanics*, *93*, 64–78. https://doi.org/10.1016/j.tafmec.2017.06.022

Hong, H. C., & Huang, H. W. (2014). Effects of Cont Rail Joint Type on Bus Rollover Crashworthiness. *Advanced Materials Research*, *945-949*, 156–161. https://doi.org/10.4028/www.scientific.net/amr.945-949.156

Huang, Z., & Zhang, X. (2018). Three-point bending collapse of thin-walled rectangular beams. *International Journal of Mechanical Sciences*, *144*(April), 461–479. https://doi.org/10.1016/j.ijmecsci.2018.06.001

Huang, Z., & Zhang, X. (2020). Crashworthiness and optimization design of quadruple-cell Aluminum/CFRP hybrid tubes under transverse bending. *Composite Structures*, *235*, 111753. https://doi.org/10.1016/j.compstruct.2019.111753

Huang, Z., Zhang, X., & Fu, X. (2020). On the bending force response of thin-walled beams under transverse loading. *Thin-Walled Structures*, *154*(March), 106807. https://doi.org/10.1016/j.tws.2020.106807

Huang, Z., Zhang, X., & Yang, C. (2020). Experimental and numerical studies on the bending collapse of multi-cell Aluminum/CFRP hybrid tubes. *Composites Part B: Engineering*, *181*, 107527. https://doi.org/10.1016/j.compositesb.2019.107527

Jakubczak, P., Gliszczyński, A., Bieniaś, J., Majerski, K., & Kubiak, T. (2017). Collapse of channel section composite profile subjected to bending Part II: Failure analysis. *Composite Structures*, *179*, 1–20. https://doi.org/10.1016/j.compstruct.2017.07.052

Jung, D. W., Kim, H. J., & Choi, N. S. (2009). Aluminum-GFRP hybrid square tube beam reinforced by a thin composite skin layer. *Composites Part A: Applied Science and Manufacturing*, *40*(10), 1558–1565. https://doi.org/10.1016/j.compositesa.2009.06.015

Kadir, A. M., Priadi, D., Siradj, E. S., & Setiyono, H. (2013). Developing a strength analytical method of a thin-walled steel SHS beam by combine theory of plastic mechanisms and non-linear elastic. *Advanced Materials Research*, *746*, 428–433. https://doi.org/10.4028/www.scientific.net/AMR.746.428

Kah, P., Suoranta, R., Martikainen, J., & Magnus, C. (2014). Techniques for joining dissimilar materials: metals and polymers. *Rev. Adv. Mater. Sci.*, *36*, 152–164.

Kang, K. T., Chun, H. J., Park, J. C., Na, W. J., Hong, H. T., & Hwang, I. H. (2012). Design of a composite roll bar for the improvement of bus rollover crashworthiness. *Composites Part B: Engineering*, *43*(4), 1705–1713. https://doi.org/10.1016/j.compositesb.2012.01.072

Kecman, D. (1979). *Bending collapse of rectangular section tubes in relation to the bus roll over problem* (PhD Thesis). Cranfield Insititute of Technology.

Kecman, D. (1983). Bending collapse of rectangular and square section tubes. *International Journal of Mechanical Sciences*, *25*(9-10), 623–636. https://doi.org/10.1016/0020-7403(83)90072-3

Kelly, T., & Clyne, B. (1999). Composite Materials—Reflections on the First Half Century. *Physics Today*, *52*(11), 37–41. https://doi.org/10.1063/1.882882

Kim, H. C., Shin, D. K., & Lee, J. J. (2013). Characteristics of aluminum/CFRP short square hollow section beam under transverse quasi-static loading. *Composites Part B: Engineering*, *51*, 345–358. https://doi.org/10.1016/j.compositesb.2013.03.020

Kim, S. Y., Jeong, J. W., Kim, J. Y., Kim, H. C., Shin, D. K., Shin, K. C., & Lee, J. J. (2017). Energy absorption characteristics of aluminium/CFRP hybrid beam under impact loading. *International Journal of Crashworthiness*, *22*(2), 190–201. https://doi.org/10.1080/13588265.2016.1243637

Kim, T. H., & Reid, S. R. (2001). Bending collapse of thin-walled rectangular section columns. *Computers and Structures*, *79*(20-21), 1897–1911. https://doi.org/10.1016/S0045-7949(01)00089-X

Kim, Y. T., Lee, M. J., & Lee, B. C. (2011). Simulation of adhesive joints using the superimposed finite element method and a cohesive zone model. *International Journal of Adhesion and Adhesives*, *31*(5), 357–362. https://doi.org/10.1016/j.ijadhadh.2010.11.015

Klein, B. (2013). *Leichtbau-Konstruktion: Berechnungsgrundlagen und Gestaltung* (10th ed.). Springer.

Krolo, P., Grandić, D., & Smolčić, Ž. (2016). Experimental and Numerical Study of Mild Steel Behaviour under Cyclic Loading with Variable Strain Ranges. *Advances in Materials Science and Engineering*, *2016*. https://doi.org/10.1155/2016/7863010

Kuo, E. Y., Mehta, P. R., Prater, G., & Shahhosseini, A. M. (2006). Reliability and Quality of Body Concept CAE Models for Design Direction Studies. *SAE Technical Paper Series*, *1*(724). https://doi.org/10.4271/2006-01-1617

Lauter, C., Tröster, T., & Reuter, C. C. (2013). Hybrid Structures Consisting of Sheet Metal and Fibre Reinforced Applications. In *Advanced composite materials for automotive applications: Structural integrity and crashworthiness* (pp. 149–174). John Wiley & Sons Ltd. https://doi.org/doi:10.1002/9781118535288.ch7

Lavayen-Farfan, D., Boada, M. J. L., & Rodriguez-Hernandez, J. A. (2021). Bending collapse analysis for thin and medium-thin-walled square and rectangular hollow shapes. *Thin-Walled Structures*, *165*, 107934. https://doi.org/10.1016/j.tws.2021.107934

Lavayen-Farfan, D., Butenegro-Garcia, J. A., Boada, M. J. L., Martinez, M. A., & Rodriguez-Hernandez, J. A. (2022). Theoretical and experimental study of the bending collapse of partially reinforced CFRP-Steel square tubes. *Thin-Walled Structures*, *177*, 109457. https://doi.org/10.1016/j.tws.2022.109457

Lee, S. H., Kim, C. W., & Choi, N. S. (2006). Bending collapse behaviors and energy absorption characteristics of aluminum-GFRP hybrid tube beams. *Key Engineering Materials*, *326-328 II*, 1825–1828. https://doi.org/10.4028/www.scientific.net/kem.326-328.1825

Lee, S. H., Kim, H. J., & Choi, N. S. (2006). Bending performance analysis of aluminum-composite hybrid tube beams. *Key Engineering Materials*, *306-308 II*, 769–774. https://doi.org/10.4028/www.scientific.net/KEM.306-308.769

Li, Z., Tian, Y., Bai, J., & Zuo, W. (2021). Bending collapse of treble rectangular thin-walled tubes and its application in conceptual design for automobile crashworthiness. *Proceedings of the Institution of Mechanical Engineers, Part D: Jour-*

nal of Automobile Engineering, *235*(5), 1269–1284. https://doi.org/10.1177/0954407020967869

Liang, C. C., & Le, G. N. (2009). Bus rollover crashworthiness under European standard: An optimal analysis of superstructure strength using successive response surface method. *International Journal of Crashworthiness*, *14*(6), 623–639. https://doi.org/10.1080/13588260902920670

Liang, C. C., & Le, G. N. (2010a). Optimization of bus rollover strength by consideration of the energy absorption ability. *International Journal of Automotive Technology*, *11*(2), 173–185. https://doi.org/10.1007/s12239-010-0023-3

Liang, C. C., & Le, G. N. (2010b). Analysis of bus rollover protection under legislated standards using LS-DYNA software simulation techniques. *International Journal of Automotive Technology*, *11*(4), 495–506. https://doi.org/10.1007/s12239-010-0061-x

Litebus. (2009). Litebus - Modular lightweight snadwich bus concept. http://cordis.europa.eu/project/rcn/79972%7B%5C_%7Den.html.

Liu, Q., Lin, Y., Zong, Z., Sun, G., & Li, Q. (2013). Lightweight design of carbon twill weave fabric composite body structure for electric vehicle. *Composite Structures*, *97*, 231–238. https://doi.org/10.1016/j.compstruct.2012.09.052

Liu, Q., Xu, X., Ma, J., Wang, J., Shi, Y., & Hui, D. (2017). Lateral crushing and bending responses of CFRP square tube filled with aluminum honeycomb. *Composites Part B: Engineering*, *118*, 104–115. https://doi.org/10.1016/j.compositesb.2017.03.021

Liu, Y., & Day, M. L. (2008). Bending collapse of thin-walled circular tubes and computational application. *Thin-Walled Structures*, *46*(4), 442–450. https://doi.org/10.1016/j.tws.2007.07.014

Lotfollahi, M., Alinia, M. M., & Taciroglu, E. (2016). Validated finite element techniques for quasi-static cyclic response analyses of braced frames at sub-member scales. *Engineering Structures*, *106*, 222–242. https://doi.org/10.1016/j.engstruct.2015.07.049

Ma, Q., Sun, J., Gan, X., & Sun, Z. (2020). Experiment and modified model for CFRP/steel hybrid tubes under the quasi-static transverse loading. *International Journal of Crashworthiness*, *26*(3), 1–11. https://doi.org/10.1080/13588265.2020.1717918

Mamalis, A., Manolakos, D., Demosthenous, G., & Johnson, W. (1991). Axial plastic collapse of thin bi-material tubes as energy dissipating systems. *International Journal of Impact Engineering*, *11*(2), 185–196. https://doi.org/10.1016/0734-743X(91)90005-Z

Matthews, F., & Rawlings, R. (2008). *Composite materials: Engineering and science* (6th ed.). Woodhead Publishing.

Mckay, M. D., Beckman, R. J., & Conover, W. J. (1979). A Comparison of Three Methods for Selecting Values of Input Variables in the Analysis of Output From a Computer Code. *Technometrics*, *42*(1), 55–61. https://doi.org/10.1080/00401706.2000.10485979

Megson, T. (2019). *Structural and Stress Analysis* (4th ed.). Butterworth-Heinemann.

Montgomery, D. C. (2017). *Design and Analysis of Experiments* (9th ed.). Wiley.

Mundo, D., Donders, S., Hadjit, R., Stigliano, G., Mas, P., Van Der Auweraer, H., Hadjit, R., Stigliano, G., Mas, P., & Van Der Auweraer, H. (2010). Concept modelling of automotive beams, joints and panels. *Proceedings of the 3rd WSEAS Int. Conference on Finite Differences - Finite Elements - Finite Volumes - Boundary Elements*, *57*(1), 71–83.

Mundo, D., Donders, S., Stigliano, G., & Auweraer, H. V. D. (2011). Concept design of vehicle bodies using reduced models of beams, joints and panels. *International Journal of Vehicle Design*, *57*(1), 71. https://doi.org/10.1504/IJVD.2011.043593

Myers, R. H., Montgomery, D. C., & Anderson-Cook, C. M. (2016). *Response Surface Methodology - Process and product optimization using designed experiments* (1st ed.). Wiley.

Nargund, S., & Williams, D. K. (2016). Review and Comparison of Buckling Methodologies for ASME B&PV Code, Section III, Subsection NF Linear Piping Restraints. *Volume 11: Systems, Design, and Complexity*, (December 2018). https://doi.org/10.1115/IMECE2016-67207

Nasrolahzadeh, N., Fard, M., & Tatari, M. (2013). Automotive Concept Modelling: Optimization of the Vehicle NVH Performance. In *Proceedings of the fisita 2012 world automotive congress* (pp. 365–376). Springer. https://doi.org/10.1007/978-3-642-33738-3

Neto, J. A., Campilho, R. D., & Da Silva, L. F. (2012). Parametric study of adhesive joints with composites. *International Journal of Adhesion and Adhesives*, *37*, 96–101. https://doi.org/10.1016/j.ijadhadh.2012.01.019

Nigade, S. R., Dandge, S. S., Mahajan, R. S., & Vankudre, H. V. (2013). Rollover Analysis of Bus Using Body Section Method as per AIS-031 Standard. *SAE Technical Paper Series*, *1*, 1–5. https://doi.org/10.4271/2013-26-0038

Olsson, A., Sandberg, G., & Dahlblom, O. (2003). On Latin hypercube sampling for structural reliability analysis. *Structural Safety*, *25*(1), 47–68. https://doi.org/10.1016/S0167-4730(02)00039-5

Park, S. J., & Yoo, W. S. (2008). Rollover analysis for the body section structure of a large bus using beam and non-linear spring elements. *Proceedings of the Institution of Mechanical Engineers, Part D: Journal of Automobile Engineering*, *222*(6), 955–962. https://doi.org/10.1243/09544070JAUTO474

Phadatare, V. D., & Hujare, P. (2017). Performance Improvement of Bus Structure for Rollover Analysis Using FEA and Validation of Roll Bar. *IOSR Journal of Mechanical and Civil Engineering*, *17*(10), 16–19. https://doi.org/10.9790/1684-17010041619

Policia Nacional del Peru. (2017). *Anuario Estadistico 2017* (tech. rep.). http://www.gbv.de/dms/spk/iai/toc/865661790.pdf

Qu, Z.-Q. (2004). *Model Order Reduction Techniques*. Springer London. https://doi.org/10.1007/978-1-4471-3827-3

Rajamani, R. (2012). *Vehicle Dynamics and Control* (2nd ed.). Springer.

Rhodes, J., & Harvey, J. M. (1971). The Local Buckling and Post Local Buckling Behaviour of Thin-Walled Beams. *Aeronautical Quarterly*, *22*(4), 363–388. https://doi.org/10.1017/s0001925900005904

Rincón-Dávila, D., Alcalá, E., & Martín, Á. (2019). Theoretical-experimental study of the repair of steel bus structures after rollover. *Journal of Constructional Steel Research*, *162*, 105734. https://doi.org/10.1016/j.jcsr.2019.105734

Rincón-Dávila, D., Alcalá, E., & Martín, Á. (2022). Theoretical–experimental study of the bending behavior of thin-walled rectangular tubes. *Thin-Walled Structures*, *173*(January), 109009. https://doi.org/10.1016/j.tws.2022.109009

Roca, T., Arbiol, J., & Ruiz, S. (1997). Development of Rollover-Resistant Bus Structures. *SAE Technical Paper Series*.

Roux, W. J., Stander, N., & Haftka, R. T. (1998). Response surface approximations for structural optimization. *International Journal for Numerical Methods in Engineering*, *42*(3), 517–534. https://doi.org/10.1002/(SICI)1097-0207(19980615)42:3⟨517::AID-NME370⟩3.0.CO;2-L

Ruiz, S., Cruz, P., Sorita, B., & Vida, H. (2009). New Optimized Bus Structure to Improve the Roll-Over Test (ECE-R66) Using Structural Foam with High Strength Steel.

SAE Technical Papers, *2009-Janua*(January). https://doi.org/10.4271/2009-26-0003

Salvini, P., & Vivio, F. (2007). Dynamic reduction strategies to extend modal analysis approach at higher frequencies. *Finite Elements in Analysis and Design*, *43*(11-12), 931–940. https://doi.org/10.1016/j.finel.2007.06.001

Seiffert, U., & Gonter, M. (2013). *Integrated Automotive Safety Handbook*. SAE International. https://doi.org/10.4271/R-407

Senthil, K., Arockiarajan, A., & Palaninathan, R. (2018). Numerical study on the onset of initiation of debond growth in adhesively bonded composite joints. *International Journal of Adhesion and Adhesives*, *84*(March), 202–219. https://doi.org/10.1016/j.ijadhadh.2018.03.009

Shi, L., Yang, R. J., & Zhu, P. (2012). A method for selecting surrogate models in crashworthiness optimization. *Structural and Multidisciplinary Optimization*, *46*(2), 159–170. https://doi.org/10.1007/s00158-012-0760-1

Shields, M. D., & Zhang, J. (2016). The generalization of Latin hypercube sampling. *Reliability Engineering and System Safety*, *148*, 96–108. https://doi.org/10.1016/j.ress.2015.12.002

Shin, K. C., Lee, J. J., Kim, K. H., Song, M. C., & Huh, J. S. (2002). Axial crush and bending collapse of an aluminum/GFRP hybrid square tube and its energy absorption capability. *Composite Structures*, *57*(1-4), 279–287. https://doi.org/10.1016/S0263-8223(02)00094-6

Shishesaz, M., & Hosseini, M. (2018). Effects of joint geometry and material on stress distribution, strength and failure of bonded composite joints: an overview. *The Journal of Adhesion*, *00*(00), 1–69. https://doi.org/10.1080/00218464.2018.1554483

Song, X., Sun, G., Li, G., Gao, W., & Li, Q. (2013). Crashworthiness optimization of foam-filled tapered thin-walled structure using multiple surrogate models. *Structural and Multidisciplinary Optimization*, *47*(2), 221–231. https://doi.org/10.1007/s00158-012-0820-6

Stein, M. (1987). Large sample properties of simulations using latin hypercube sampling. *Technometrics*, *29*(2), 143–151. https://doi.org/10.1080/00401706.1987.10488205

Stigliano, G., Mundo, D., Donders, S., & Tamarozzi, T. (2010). Advanced Vehicle Body Concept Modeling Approach Using Reduced Models of Beams and Joints. *SMA 2010 - International Conference on Modal Analysis Noise and Vibration Engineering, 20-22 September 2010, Leuven, Belgium*, 4179–4190.

Su, R., Gui, L., & Fan, Z. (2011). Multi-objective optimization for bus body with strength and rollover safety constraints based on surrogate models. *Structural and Multidisciplinary Optimization*, *44*(3), 431–441. https://doi.org/10.1007/s00158-011-0627-x

Sun, G., Li, G., Stone, M., & Li, Q. (2010). A two-stage multi-fidelity optimization procedure for honeycomb-type cellular materials. *Computational Materials Science*, *49*(3), 500–511. https://doi.org/10.1016/j.commatsci.2010.05.041

Takewaki, I. (1998). Inverse component-mode synthesis method for redesign of large structural systems. *Computer Methods in Applied Mechanics and Engineering*, *166*(3-4), 201–209. https://doi.org/10.1016/S0045-7825(98)00070-X

Tang, B. (1993). Orthogonal array-based latin hypercubes. *Journal of the American Statistical Association*, *88*(424), 1392–1397. https://doi.org/10.1080/01621459.1993.10476423

Tang, J., & Chen, X. (2018). Experimental investigation on ultimate strength and failure response of composite box beams used in wind turbine blades. *Composite Structures*, *198*(May), 19–34. https://doi.org/10.1016/j.compstruct.2018.05.042

Tsai, M., Oplinger, D., & Morton, J. (1998). Improved theoretical solutions for adhesive lap joints. *International Journal of Solids and Structures*, *35*(12), 1163–1185. https://doi.org/10.1016/S0020-7683(97)00097-8

UN/ECE 66. (2007). Regulation No 66 of the Economic Commission for Europe of the United Nations (EN/ECE) - Uniform technical prescriptions concerning the approval of large passenger vehicles with regard to the strength of their superstructure.

US DoT. (1976). Federal Motor Vehicle Safety Standard 220: School bus rollover protection.

Vignjevic, R., Liang, C., Hughes, K., Brown, J. C., De Vuyst, T., Djordjevic, N., & Campbell, J. (2019). A numerical study on the influence of internal corrugated reinforcements on the biaxial bending collapse of thin-walled beams. *Thin-Walled Structures*, *144*(June), 106277. https://doi.org/10.1016/j.tws.2019.106277

Volkersen, O. (1938). Die Niekraftverteilung in Zugbeanspruchten mit Konstanten Laschenquerschritten. *Luftfahrtforschung*, *15*, 41–47.

Weiß, L. (2018). A simplified model for structural stiffness and crashworthiness optimisation of composite fuselages. *Structural and Multidisciplinary Optimization*, (2002). https://doi.org/10.1007/s00158-018-2166-1

Wierzbicki, T., & Abramowicz, W. (1983). On the Crushing Mechanics of Thin-Walled Structures. *Journal of Applied Mechanics*, *50*(4a), 727–734. https://doi.org/10.1115/1.3167137

Wierzbicki, T., Recke, L., Abramowicz, W., Gholami, T., & Huang, J. (1994a). Stress profiles in thin-walled prismatic columns subjected to crush loading-I. Compression. *Computers and Structures*, *51*(6), 625–641. https://doi.org/10.1016/S0045-7949(05)80002-1

Wierzbicki, T., Recke, L., Abramowicz, W., Gholami, T., & Huang, J. (1994b). Stress profiles in thin-walled prismatic columns subjected to crush loading-II. Bending. *Computers and Structures*, *51*(6), 625–641. https://doi.org/10.1016/S0045-7949(05)80002-1

Wilson, A. (2017). Vehicle weight is the key driver for automotive composites. *Reinforced Plastics*, *61*(2), 100–102. https://doi.org/10.1016/j.repl.2015.10.002

Xie, S., Li, H., Yang, C., & Yao, S. (2018). Crashworthiness optimisation of a composite energy-absorbing structure for subway vehicles based on hybrid particle swarm optimisation. *Structural and Multidisciplinary Optimization*, *58*(5), 2291–2308. https://doi.org/10.1007/s00158-018-2022-3

Xiong, F., Wang, D., Chen, S., Gao, Q., & Tian, S. (2018). Multi-objective lightweight and crashworthiness optimization for the side structure of an automobile body. *Structural and Multidisciplinary Optimization*, *58*(4), 1823–1843. https://doi.org/10.1007/s00158-018-1986-3

Xu, F., Sun, G., Li, G., & Li, Q. (2013). Crashworthiness design of multi-component tailor-welded blank (TWB) structures. *Structural and Multidisciplinary Optimization*, *48*(3), 653–667. https://doi.org/10.1007/s00158-013-0916-7

Xu, K., Xu, P., Yang, C., Wang, T., Li, B., Che, Q., Yao, S., & Huang, Q. (2020). Crashworthiness optimisation for the rectangular tubes with axisymmetric and uniform thicknesses under offset loading. *Structural and Multidisciplinary Optimization*, (2001). https://doi.org/10.1007/s00158-020-02535-1

Xu, R. Z., & Zhou, W. (2011). The finite element analysis of the coach body frontal crash and structure improvement. *Proceedings of 2011 International Conference on Electronic and Mechanical Engineering and Information Technology, EMEIT 2011*, *1*, 77–82. https://doi.org/10.1109/EMEIT.2011.6022843

you Xie, Z. (2020). The reinforcement optimization of thin-walled square tubes for bending crashworthiness. *International Journal of Crashworthiness*, *0*(0), 1–7. https://doi.org/10.1080/13588265.2020.1766186

Yu, Y., Ying, L., Hu, P., Yu, Y., Li, X., & Fan, R. (2015). Optimization Design Method of School Bus Structure Lightweight on the Rollover Safety. In *Lecture notes in electrical engineering* (pp. 261–268). Springer. https://doi.org/10.1007/978-3-662-45043-7_28

Zhang, G., Zhang, X., & Liu, B. (2011). The study of bus superstructure strength based on rollover test using body sections. *Advances in Intelligent and Soft Computing*, *129*, 315–322. https://doi.org/10.1007/978-3-642-25986-9_49

Zhang, X., Zhang, H., & Ren, W. (2016). Bending collapse of folded tubes. *International Journal of Mechanical Sciences*, *117*, 67–78. https://doi.org/10.1016/j.ijmecsci.2016.07.016

Zhang, X., Zhang, H., & Wang, Z. (2016). Bending collapse of square tubes with variable thickness. *International Journal of Mechanical Sciences*, *106*, 107–116. https://doi.org/10.1016/j.ijmecsci.2015.12.006

Zhao, D., & Xue, D. (2010). A comparative study of metamodeling methods considering sample quality merits. *Structural and Multidisciplinary Optimization*, *42*(6), 923–938. https://doi.org/10.1007/s00158-010-0529-3

Zhou, W., Kuznectov, A., Wu, C. Q., & Telichev, I. (2019). A comparative numerical study of motorcoach rollover resistance under ECE R66 and proposed NHTSA regulation conditions. *International Journal of Crashworthiness*, *0*(0), 1–16. https://doi.org/10.1080/13588265.2018.1544476

Appendix A

Matlab - Ansys connection

In this Ph.D. work, a large number of FEM simulations were required, different parameters in each simulation had to be changed for optimization and exploration of various design points. Thus, an automated method to change the parameter values and extract results had to be implemented. For instance, the Latin Hypercube experimental designed used, required the definition of multiple design points and the calculation of certain parameters afterwards, which might be cumbersome in Ansys, thus Matlab is chosen as an alternative for post-processing. It should be noted, that other alternatives for post-processing, such as Python are also possible. The choice of using Matlab is merely due to the author's familiarity with its programming language. The connection between both programs requires Matlab toolbox, as detailed below. Not much information has been found to setup this kind of connections, for further information and diffusion of the proposed method, the following procedure has been also detailed in the author's personal blog:
http://blog.pucp.edu.pe/blog/daniellavayen/2020/10/09/conectar-matlab-y-ansys/.

A.1 Requirements

The followings versions of each program are required to make the connection work:

- ANSYS 15 or above.
- Matlab 2014b-2020b (newer versions still not supported).
- Matlab toolbox: Ansys as Server - ver 1.1.10 (beta). Available on the Ansys Customer Portal.

The file `ansys_aas 1.1.10.mltbx` must be opened and installed in a Matlab session in order to invoke it when needed.

A.2 Algorithm

Preparations

Once the toolbox is installed, the "Mechanical APDL Product Launcher" must be started, which allows to launch as many Ansys APDL instances as required with a default configuration. The working directory has to be specified, as well as the option "-aas" as an "Additional Parameter", in the "Customization / preferences" tab. The "-aas" parameter launches APDL in batch mode and creates two files required for the connection. Note that, unlike a normal session, only the APDL output window will open and no GUI will be available. The created files are:

- `aaS_MapdlId.txt`: includes the key for the aaS session.
- `aaS_MapdlExceptionHolderServer.txt`: includes details for connecting to the aaS session.

Once an Ansys ADPL session is started in "Ansys as Server" mode, it begins to wait for instructions from any CORBA [1] supported source and a CORBA compiler. Certain programming languages such as C++, Python and Java offer native support for CORBA (ANSYS Inc., 2021b). The toolbox `ansys aas 1.1.10.mltbx` provides this support for certain versions of Matlab.

Main steps

In Matlab, the communication with APDL starts with the command `initialize_orb()`, and then the command `load_ansys_aas`. The working directory must contain the created files mentioned above. The commands are specified below:

```
orb = initialize_orb();
load_ansys_aas;
iCoMapdlUnit = actmapdlserver(orb,'<folder>/aaS_MapdlId.txt');
```

These commands set the communications between the current Matlab session and the Ansys batch session. Once the communication is established, the following command can be used to send instructions to Ansys, using the APDL language:

```
char(iCoMapdl(executeCommandToString('APDL command here')));
```

Now that APDL commands can be sent from Matlab (even from a different computer). This method is useful when single commands are required or sent one by one. However, if a Matlab .m file, containing several Ansys APDL commands is executed, a synchronization problem occurs between both programs. It may occur that Ansys is executing the solution process, while Matlab attempts to access the result files. This would end up in execution errors in Matlab or in crashes in Ansys. To avoid these kind of problems, it is recommended to prepare a .txt file with the APDL commands in it, and sending the `/input,...` command to Ansys via Matlab, as follows:

```
char(iCoMapdl(executeCommandToString(...
        "/input,commandstosend,txt,'<folder>'")));
```

The `commandstosend.txt` file is then read by Ansys and executed normally. This file may have the following general structure:

```
/filname, File_Name
/title, Proyect_Title
! Parameters
...
! Pre-processor
/prep7
...
! Solver configuration
/solu
...
! Graphical post processor (not available in batch mode)
/post1
```

[1] Common Object Request Broker Architecture

```
...
! Time-history post processor.
/post26
...
/save
/fini
```

Once the .txt file with the commands is sent to Ansys for execution, Matlab does not wait for a response from Ansys to finish execution. At this point, both programs are out of sync. The solution is to introduce a pause to Matlab until certain Ansys output files are created. Each ten seconds, Matlab checks if the output files containing the desired results are present. If they are found, the wait is stopped and post-processing in Matlab can continue. The workflow of the Ansys-Matlab connection is depicted in Fig. A.1.

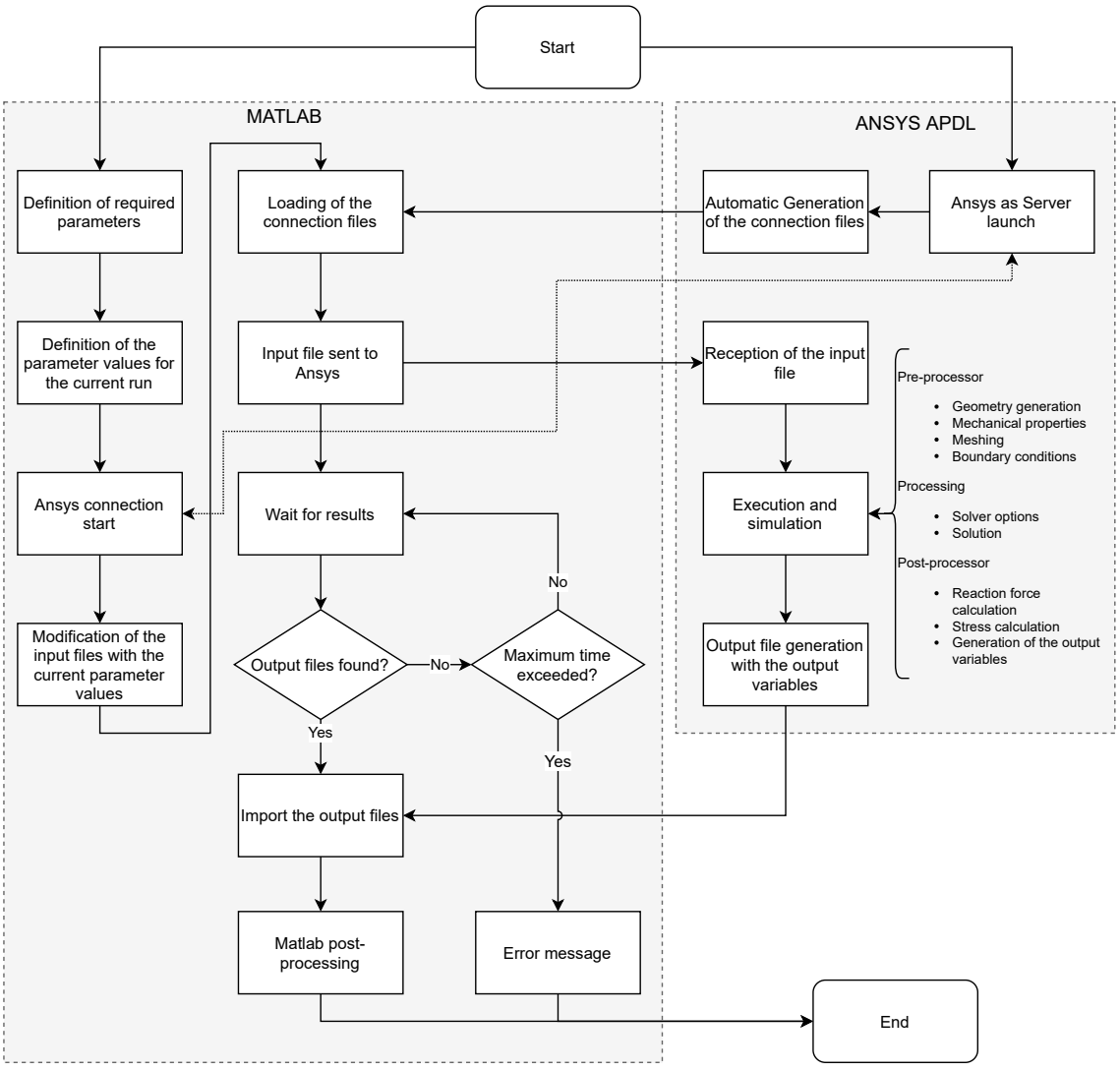

Figure A.1: Flowchart of the connection.

A.3 Final comments

In this appendix, the general procedure for the Ansys-Matlab connection is detailed, using the `Ansys_aas 1.1.10.mltbx` toolbox. This procedure has been used in different chapters of the thesis where several simulations with different dimensions and parameters are required. In certain scenarios, it has been found that the geometry may not be generated adequately (Ansys bug for certain commands related to node numbering) and the simulation may take longer than expected, mainly due to numerical issues. In order to overcome these kind of difficulties, it is recommended to manually execute a couple of runs to check if the program is executed adequately. Additionally, when variations in size are required, meshing should be based on number of divisions and not element size, to ensure similar simulation times. Furthermore, to ensure that the output files are created and filled, an extra 5 seconds pause should be added to the Matlab script.